



NUMERICAL SIMULATION OF SUPERSONIC
TURBULENT BOUNDARY LAYER FLOW
UNDER THE INFLUENCE OF MILD
PRESSURE GRADIENTS

THESIS
Eric Thomas Fick
Captain, USAF

AFIT/GAE/ENY/95D-10

DISTRIBUTION STATEMENT A

Approved for public release;
Distribution Unlimited

19970606 100

DEPARTMENT OF THE AIR FORCE
AIR UNIVERSITY
AIR FORCE INSTITUTE OF TECHNOLOGY

Wright-Patterson Air Force Base, Ohio

AFIT/GAE/ENY/95D-10

**NUMERICAL SIMULATION OF SUPERSONIC
TURBULENT BOUNDARY LAYER FLOW
UNDER THE INFLUENCE OF MILD
PRESSURE GRADIENTS**

**THESIS
Eric Thomas Fick
Captain, USAF**

AFIT/GAE/ENY/95D-10

Approved for public release; distribution unlimited

**The views expressed in this thesis are those of the author and do not reflect the official
policy or position of the Department of Defense or the U. S. Government.**

AFIT/GAE/ENY/95D-10

**NUMERICAL SIMULATION OF SUPERSONIC
TURBULENT BOUNDARY LAYER FLOW
UNDER THE INFLUENCE OF MILD
PRESSURE GRADIENTS**

THESIS

**Presented to the Faculty of the Graduate School of Engineering
of the Air Force Institute of Technology
Air University
In Partial Fulfillment of the
Requirements for the Degree of
Master of Science**

Eric Thomas Fick, B.S.

Captain, USAF

December, 1995

Approved for public release; distribution unlimited

Preface

Although the title page of this document reflects me as the author and I alone am responsible for its content, I cannot take full credit for the research performed herein. I owe a great debt of gratitude to Dr. Datta Gaitonde for his insight, help, patience, and suggestions. Without it, this thesis would not exist. The wealth of knowledge possessed and freely shared by Dr. Rodney Bowersox and my advisor, Major Thomas Buter, proved to be invaluable as well. I would like to thank my wife, Christine for her help and encouragement through the dark days and my sons, John and Kevin, for reminding me that turbulence modeling is not the end of the world. Without the three of you, this research would be meaningless.

Eric Thomas Fick

Table of Contents

	Page
Preface	ii
List of Figures	iv
List of Tables	ix
List of Symbols	x
List of Abbreviations	xiii
Abstract	xiv
I. Introduction	1-1
1.1 Problem Motivation	1-1
1.2 The Closure Problem	1-2
1.3 “Excuse me, your Boussinesq is showing”	1-4
1.4 Flowfield Configuration	1-6
1.5 Summary	1-6
II. Problem Descriptions	2-1
2.1 AFIT Mach 3 Blowdown Wind Tunnel	2-1
2.2 Nozzle	2-1
2.3 Zero Pressure Gradient (ZPG) Test Sections	2-1
2.4 Favorable Pressure Gradient (FPG) Test Section	2-2
2.5 Adverse Pressure Gradient (APG) Test Section	2-3
III. Numerical Formulation	3-1
3.1 Governing Equations	3-1
3.2 Algorithm Development	3-3

	Page
3.2.1 Boundary Conditions	3-5
3.2.2 Implementation	3-7
3.3 Turbulence Modeling	3-9
3.3.1 Baldwin - Lomax Turbulence Model	3-10
3.3.2 $k - \omega$ Turbulence Model	3-13
IV. Grid Refinement and Flat-Plate Validation	4-1
4.1 Variation in Normal Node Count	4-1
4.2 Variation in Streamwise Node Count	4-3
4.3 Variation in Wall Spacing	4-4
4.4 Final Grid Generation	4-4
4.5 Flat Plate Validation	4-5
4.6 Upstream Boundary Conditions	4-7
4.6.1 Freestream Inflow	4-8
4.6.2 Experimental Profile Inflow	4-8
V. Results and Discussion	5-1
5.1 Validation	5-1
5.1.1 ZPG Test Section	5-1
5.1.2 FPG Test Section	5-4
5.1.3 APG Test Section	5-7
5.2 Comparison to Baldwin-Lomax Results	5-11
5.2.1 Zero Pressure Gradient (ZPG) Test Section	5-13
5.2.2 Favorable Pressure Gradient (FPG) Test Section . .	5-15
5.2.3 Adverse Pressure Gradient (APG) Test Section . .	5-16
5.2.4 Surface Effects	5-19
5.2.5 Computational Expense and Convergence Characteristics	5-20
5.3 Evaluation of Inflow Boundary Condition Effects	5-22

	Page
5.3.1 Zero Pressure Gradient (ZPG) Test Section	5-23
5.3.2 Favorable Pressure Gradient (FPG) Test Section . .	5-24
5.3.3 Adverse Pressure Gradient (APG) Test Section . . .	5-24
5.3.4 Surface Effects	5-26
5.3.5 Summary	5-31
5.4 Flowfield Analysis	5-33
5.4.1 Favorable Pressure Gradient (FPG) Test Section . .	5-33
5.4.2 Adverse Pressure Gradient (APG) Test Section . . .	5-38
VI. Conclusions and Recommendations for Further Investigation	6-1
6.1 Conclusions	6-1
6.2 Recommendations for Further Investigation	6-2
Appendix A. Strong Conservation Law form of Governing Differential Equations	A-1
Appendix B. Finite Volume Method Overview	B-1
Appendix C. Extrapolation and Limiting	C-1
C.1 Left State	C-1
C.2 Right State	C-3
Appendix D. Coordinate Transformation	D-1
Appendix E. Time-Averaged Navier-Stokes Equations	E-1
E.1 Reynolds Averaging	E-1
E.2 Favré Averaging	E-2
Appendix F. AFIT Supersonic Pressure-Vacuum Wind Tunnel	F-1
Appendix G. Additional Figures	G-1

	Page
Bibliography	BIB-1
Vita	VITA-1

List of Figures

Figure	Page
2.1. Nozzle Cross Section	2-2
2.2. Favorable Pressure Gradient Test Section Cross Section	2-2
2.3. Surface Pressure in Test Sections	2-3
2.4. Adverse Pressure Gradient Test Section Cross Section	2-4
 3.1. Cell Configuration Along a Solid Wall Boundary	3-5
4.1. $y^+ \text{ vs } u^+$ (van Driest)	4-6
4.2. $C_f \text{ vs } Re_\theta$	4-7
4.3. k and ω Experimental Inflow Profiles	4-9
 5.1. Mach Number vs y/δ_M , ZPG, FS 60.0/44.0	5-2
5.2. Nondimensional Turbulent Shear Stress vs y/δ_M , ZPG, FS 60.0/44.0 .	5-3
5.3. u/u_e vs y/δ_u , ZPG, FS 60.0/71.5	5-4
5.4. Nondimensional Turbulent Shear Stress vs y/δ_u , ZPG, FS 60.0/71.5 ..	5-5
5.5. k vs y/δ_u , ZPG, FS 60.0/71.5	5-5
5.6. Mach Number vs y/δ_M , FPG, FS 71.5	5-6
5.7. Nondimensional Turbulent Shear Stress vs y/δ_M , FPG, FS 71.5 . . .	5-6
5.8. u/u_e vs y/δ_u , FPG, FS 71.5	5-8
5.9. Nondimensional Turbulent Shear Stress vs y/δ_u , FPG, FS 71.5 . . .	5-8
5.10. k vs y/δ_u , FPG, FS 71.5	5-9
5.11. Mach Number vs y/δ_M , APG, FS 71.0	5-10
5.12. Nondimensional Turbulent Shear Stress vs y/δ_M , APG, FS 71.0 . . .	5-10
5.13. u/u_e vs y/δ_u , APG, FS 68.0	5-11
5.14. Nondimensional Turbulent Shear Stress vs y/δ_u , APG, FS 68.0 . . .	5-12
5.15. k vs y/δ_u , APG, FS 68.0	5-12

Figure	Page
5.16. u/u_e vs y/δ_u , ZPG, FS 60.0/71.5	5-13
5.17. Nondimensional Turbulent Shear Stress vs y/δ_u , ZPG, FS 60.0/71.5 . .	5-14
5.18. μ_T/μ vs y/δ_u , ZPG, FS 60.0/71.5	5-15
5.19. u/u_e vs y/δ_u , FPG, FS 71.5	5-16
5.20. Nondimensional Turbulent Shear Stress vs y/δ_u , FPG, FS 71.5	5-17
5.21. μ_T/μ vs y , FPG, FS 71.5	5-17
5.22. u/u_e vs y/δ_u , APG, FS 68.0	5-18
5.23. Nondimensional Turbulent Shear Stress vs y/δ_u , APG, FS 68.0	5-18
5.24. μ_T/μ vs y , APG, FS 68.0	5-19
5.25. τ_{wall} vs x	5-20
5.26. p_{wall} vs x	5-21
5.27. Convergence History, $k - \omega$ vs Baldwin-Lomax	5-23
5.28. u/u_e vs y/δ_u , ZPG, FS 60.0/71.5	5-24
5.29. Nondimensional Turbulent Shear Stress vs y/δ_u , ZPG, FS 60.0/71.5 . .	5-25
5.30. u/u_e vs y/δ_u , FPG, FS 71.5	5-25
5.31. Nondimensional Turbulent Shear Stress vs y/δ_u , FPG, FS 71.5	5-26
5.32. u/u_e vs y/δ_u , APG, FS 68.0	5-27
5.33. Nondimensional Turbulent Shear Stress vs y/δ_u , APG, FS 68.0	5-27
5.34. τ_{wall} vs x	5-28
5.35. p_{wall} vs x	5-29
5.36. p_{wall} vs x and Pressure Contour Plot, FPG, Freestream Inflow	5-30
5.37. p_{wall} vs x and Pressure Contour Plot, APG, Freestream Inflow	5-30
5.38. p_{wall} vs x and Pressure Contour Plot, FPG, Experimental Profile Inflow	5-32
5.39. p_{wall} vs x and Pressure Contour Plot, APG, Experimental Profile Inflow	5-32
5.40. Schlieren Imagery of FPG Test Section	5-34
5.41. Location of Measurement Stations, FPG Test Section	5-35
5.42. Velocity vs y , FPG Test Section	5-36

Figure	Page
5.43. Nondimensional Turbulent Shear Stress vs y/δ_u , FPG Test Section	5-36
5.44. Turbulent Kinetic Energy vs y , FPG Test Section	5-37
5.45. μ_T/μ vs y/δ_u , $k - \omega$ Modeling, FPG Test Section	5-38
5.46. Schlieren Imagery of APG Test Section	5-39
5.47. Location of Measurement Stations, APG Test Section	5-40
5.48. Velocity vs y , APG Test Section	5-41
5.49. Nondimensional Turbulent Shear Stress vs y , APG Test Section	5-42
5.50. Turbulent Kinetic Energy vs y , APG Test Section	5-42
5.51. μ_T/μ vs y , $k - \omega$ Modeling	5-43
B.1. Finite Volume Cell in Computational Domain	B-2
C.1. First and Second Order Extrapolation, Left State	C-1
C.2. Sign Convention for Extrapolation and Limiting, Left State	C-2
C.3. $A > B > 0$, Left State	C-3
C.4. $B > A > 0$, Left State	C-3
C.5. $A, B < 0$, $ A > B $, Left State	C-3
C.6. $A, B < 0$, $ B > A $, Left State	C-4
C.7. Local Maximum, Left State	C-4
C.8. Local Minimum, Left State	C-4
C.9. Sign Convention for Extrapolation and Limiting, Right State	C-4
C.10. $A > B > 0$, Right State	C-5
C.11. $B > A > 0$, Right State	C-5
C.12. $A, B < 0$, $ A > B $, Right State	C-6
C.13. $A, B < 0$, $ B > A $, Right State	C-6
C.14. Local Maximum, Right State	C-6
C.15. Local Minimum, Right State	C-6
G.1. $u+$ (van Driest) vs $y+$, Upstream Flat Plate Test Section, FS 44.0, Normal Node Count Variation	G-1

Figure	Page
G.2. u^+ (van Driest) vs y^+ , Favorable Pressure Gradient Section, FS 71.5, Normal Node Count Variation	G-1
G.3. Nondimensional Velocity Profile, Upstream Flat Plate Test Section, FS 44.0, Normal Node Count Variation	G-2
G.4. Nondimensional Velocity Profile, Favorable Pressure Gradient Section, FS 71.5, Normal Node Count Variation	G-2
G.5. Nondimensional Turbulent Shear Stress Profile, Upstream Flat Plate Test Section, FS 44.0, Normal Node Count Variation	G-3
G.6. Nondimensional Turbulent Shear Stress Profile, Favorable Pressure Gradient Section, FS 71.5, Normal Node Count Variation	G-3
G.7. u^+ (van Driest) vs y^+ , Upstream Flat Plate Test Section, FS 44.0, Streamwise Node Count Variation	G-4
G.8. u^+ (van Driest) vs y^+ , Favorable Pressure Gradient Section, FS 71.5, Streamwise Node Count Variation	G-4
G.9. Nondimensional Velocity Profile, Upstream Flat Plate Test Section, FS 44.0, Streamwise Node Count Variation	G-5
G.10. Nondimensional Velocity Profile, Favorable Pressure Gradient Section, FS 71.5, Streamwise Node Count Variation	G-5
G.11. Nondimensional Turbulent Shear Stress Profile, Upstream Flat Plate Test Section, FS 44.0, Streamwise Node Count Variation	G-6
G.12. Nondimensional Turbulent Shear Stress Profile, Favorable Pressure Gradient Section, FS 71.5, Streamwise Node Count Variation	G-6
G.13. u^+ (van Driest) vs y^+ , Upstream Flat Plate Test Section, FS 44.0, Wall Spacing Variation	G-7
G.14. u^+ (van Driest) vs y^+ , Favorable Pressure Gradient Section, FS 71.5, Wall Spacing Variation	G-7
G.15. Nondimensional Velocity Profile, Upstream Flat Plate Test Section, FS 44.0, Wall Spacing Variation	G-8
G.16. Nondimensional Velocity Profile, Favorable Pressure Gradient Section, FS 71.5, Wall Spacing Variation	G-8

Figure	Page
G.17. Nondimensional Turbulent Shear Stress Profile, Upstream Flat Plate Test Section, FS 44.0, Wall Spacing Variation	G-9
G.18. Nondimensional Turbulent Shear Stress Profile, Favorable Pressure Gra- dient Section, FS 71.5, Wall Spacing Variation	G-9
G.19. Test Section Grid - FPG1	G-10
G.20. Test Section Grid - FPG2	G-10
G.21. Test Section Grid - APG1	G-11
G.22. Test Section Grid - APG2	G-11

List of Tables

Table	Page
4.1. Dimensions - Grid Study Meshes	4-2
4.2. Grid Dimensions - Test Case Grids	4-5

List of Symbols

Symbol	Description	Units
c_p	= specific heat coefficient at constant pressure	$\frac{J}{kgK}$
c_v	= specific heat coefficient at constant volume	$\frac{J}{kgK}$
C_f	= skin friction coefficient	non-dimensional
e	= internal energy per unit mass	$\frac{m^2}{s^2}$
E_t	= total internal energy	$\frac{N}{m^2}$
F, G	= flux vectors in Cartesian coordinates	N/A
\bar{F}, \bar{G}	= flux vectors in Strong Conservation Form	N/A
$\overline{\bar{F}}, \overline{\bar{G}}$	= turbulent flux vectors in Strong Conservation Form	N/A
h	= enthalpy per unit volume	$\frac{J}{kg}$
J	= Jacobian of the coordinate transformation	non-dimensional
\tilde{J}	= Jacobian of the inverse transformation	non-dimensional
k	= turbulent kinetic energy	$\frac{m^2}{s^2}$
l_{mix}	= mixing length	m
M	= Mach number	non-dimensional
\hat{n}	= surface normal	non-dimensional
p	= pressure	$\frac{N}{m^2}$
P	= vector of $k - \omega$ turbulence model source terms	N/A
Pr	= Prandtl number	non-dimensional
Pr_T	= turbulent Prandtl number	non-dimensional
q_i	= heat flux components	$\frac{W}{m^2}$
q_i^T	= turbulent heat flux components	$\frac{W}{m^2}$
R	= gas constant	$\frac{J}{kgK}$
R_e/m	= Reynolds number per meter ($\rho_\infty u_\infty / \mu_\infty$)	$\frac{1}{m}$
$R_{e\delta}$	= Reynolds number based on delta ($\rho_\infty u_\infty \delta / \mu_\infty$)	non-dimensional
t	= time	s
T	= static temperature	K
T_0	= total temperature	K

u, v	=	velocity components in Cartesian frame	$\frac{m}{s}$
u_1, u_2	=	u, v	$\frac{m}{s}$
u^+	=	inner turbulent velocity (u/u^*)	non-dimensional
u^*	=	friction velocity $\left(\sqrt{\frac{f_m}{\rho_w}}\right)$	$\frac{m}{s}$
U	=	state vector	N/A
U_{KE}	=	turbulent state vector	N/A
U_∞	=	freestream velocity	$\frac{m}{s}$
y^+	=	inner turbulent coordinate (yu^*/ν)	non-dimensional
x, y	=	Cartesian coordinates	m
x_1, x_2	=	x, y	m
$\sigma_k, \sigma_\omega, \alpha_k, \alpha_\omega$	=	closure coefficients, $k - \omega$ turbulence model	non-dimensional
$C_{k1}, C_{k2}, C_{\omega 1}, C_{\omega 2}$			
f_k, f_ω, f, C_μ			
κ_{BL}, A^+, α	=	closure coefficients, Baldwin-Lomax turbulence model	non-dimensional
C_{kleb}, C_{cp}, C_{wk}			
δ	=	boundary layer thickness, temporal finite difference	m, N/A
Δ	=	spatial finite difference	N/A
ϵ	=	dissipation rate of turbulent kinetic energy	$\frac{m^2}{s^3}$
γ	=	ratio of specific heats	non-dimensional
η_k	=	Kolmogorov length scale	m
κ	=	heat transfer coefficient	$\frac{W}{mK}$
μ	=	molecular viscosity	$\frac{N \cdot s}{m^2}$
ν	=	molecular kinematic viscosity (μ/ρ)	$\frac{m^2}{s}$
θ	=	momentum thickness	m
ρ	=	density	$\frac{kg}{m^3}$
τ_{ij}	=	shear stress tensor components	$\frac{N}{m^2}$
τ_{ij}^T	=	turbulent shear stress tensor components	$\frac{N}{m^2}$
ω	=	specific dissipation rate of turbulent kinetic energy	$\frac{1}{s}$
ω_{BL}	=	vorticity $\left(\frac{\partial v}{\partial x} - \frac{\partial u}{\partial y}\right)$	$\frac{1}{s}$
ξ, η	=	transformed computational coordinates	m

$\xi_x, \xi_y, \eta_x, \eta_y$ = metric coefficients of the coordinate transformation non-dimensional

Subscripts

<i>BL</i>	= pertaining to the Baldwin-Lomax turbulence model	N/A
<i>e</i>	= edge	N/A
<i>i,j</i>	= cell coordinates	N/A
<i>inv</i>	= inviscid	N/A
<i>M</i>	= Mach number	N/A
<i>n</i>	= current time level	N/A
<i>o</i>	= stagnation, total	N/A
<i>t</i>	= partial differentiation with respect to time	N/A
<i>T</i>	= turbulent	N/A
<i>u</i>	= velocity	N/A
<i>v</i>	= viscous	N/A
<i>wall</i>	= wall values	N/A
<i>x, y</i>	= partial differentiation in <i>x, y</i> directions	N/A
<i>ξ, η</i>	= partial differentiation in ξ, η directions	N/A
∞	= freestream	N/A

Superscripts

<i>T</i>	= turbulent	N/A
(<i>)'</i>	= Reynolds fluctuating component	N/A
(<i>)''</i>	= Favré fluctuating component	N/A
(<i>—</i>)	= Reynolds-averaged component	N/A
(<i>~</i>)	= Favré-averaged component	N/A

List of Abbreviations

Abbreviation	Meaning
APG	Adverse Pressure Gradient
FPG	Favorable Pressure Gradient
FS	Flow Station
LDV	Laser Doppler Velocimetry
TKE	Turbulent Kinetic Energy
ZPG	Zero Pressure Gradient

Abstract

Mach 2.9 boundary layer flow ($R_e/m \approx 1.75 \times 10^7$) under the influence of mild pressure gradients is studied numerically. Baldwin-Lomax and $k - \omega$ turbulence models are incorporated into a cell-centered finite volume flow solver and the results are compared with hot wire anemometry and Laser Doppler Velocimetry (LDV) measurements obtained for the same geometries in the AFIT Mach 2.9 wind tunnel. Agreement between the present simulations obtained with the $k - \omega$ turbulence model and experimental velocity profiles is excellent in all test sections. Nondimensional turbulent shear stress predictions closely match experimental data in the flat plate and adverse pressure gradient sections while slightly over-predicting this quantity in the favorable pressure gradient region. Favorable pressure gradients are found to stabilize the flowfield, resulting in increased boundary layer thickness and reduced turbulent and wall shear stress distributions. Additionally, the presence of a favorable pressure gradient is found to diminish the effects of variations in upstream boundary condition specification. Adverse pressure gradients are found to destabilize the flowfield, resulting in increases in the turbulent shear stress, turbulent kinetic energy, and wall shear stress. Upstream effects are found to play a major role in adverse pressure gradient flowfield development. Flowfield features are predicted more accurately with the $k - \omega$ model than with the Baldwin-Lomax model.

NUMERICAL SIMULATION OF SUPERSONIC
TURBULENT BOUNDARY LAYER FLOW
UNDER THE INFLUENCE OF MILD
PRESSURE GRADIENTS

I. Introduction

1.1 Problem Motivation

The vast majority of flowfields of current engineering interest are turbulent in nature. High speed turbulent flows are of particular interest to the Air Force as many of the weapon systems currently under development operate in the supersonic and hypersonic regimes. As the atmospheric conditions in which these aerospace vehicles operate become more and more hostile, experimental determination of the character of these flowfields becomes prohibitively difficult and expensive. In the current atmosphere of reduced defense spending, the emphasis must be placed on working smarter, not harder. Numerical simulation of these flowfields must be an option by which design issues may be resolved without the need to resort to expensive wind tunnel testing. It is therefore imperative that the Computational Fluid Dynamics (CFD) researcher provide the means to obtain accurate, timely solutions to these types of flow fields if the development of the next generation of aerospace vehicles is to take place. To ensure their long-term utility, the methodologies thus developed must be flexible enough to accurately resolve the flowfields over a large variety of geometries and under varying atmospheric conditions.

To increase the confidence level in computational output for arbitrary geometries under varying atmospheric conditions, steps must be taken to validate the driver code's output with existing experimental data on similar geometries subjected to similar conditions. Thus, valid data sets from supersonic turbulent flow surveys play a vital role in the development of turbulence models for CFD. Recent experimental investigations by Miller (16), Dotter (5), Luker (15), Hale (9) and Huffman (12) at the Air Force Institute of Tech-

nology (AFIT) provide excellent test cases for the development of turbulence models for CFD. The aforementioned tests were designed to meet the rigorous requirements of Settles and Dodson (20) for viable high-speed turbulence model validation cases, and as such should prove to be invaluable in the development of turbulence closure models. Since the stated goal of this data collection is to serve as a validation database for computational turbulence research, generating a code with which to perform this research is a logical companion effort.

The focus of this effort is threefold: first, add a two-equation turbulence model to an existing, validated, laminar CFD code; second, validate the code thus modified for use in turbulence research by comparing its output with the experimental data mentioned above; and third, utilize this code to evaluate the effects of pressure gradient on compressible, turbulent, boundary layer flowfields.

1.2 The Closure Problem

Turbulence is a three-dimensional time-dependent phenomenon, manifesting itself in fluid flows in which the ratio of inertial forces to viscous forces is sufficiently large. In 1937, Taylor and von Kármán (see Wilcox (27)) proposed that “turbulence is an irregular motion which in general makes its appearance in fluids, gaseous or liquid, when they flow past solid surfaces or even when neighboring streams of the same fluid flow past or over one another.” In turbulent flow, the viscous forces are insufficient to damp out small disturbances in the mean flow, which instead are amplified, leading to irregular, turbulent motion. The structure of this turbulent motion may be thought of as a cascade of eddies, in which large eddies swirling through the flow entrain smaller eddies, who in turn entrain yet smaller eddies. The energy associated with these eddies, the turbulent kinetic energy, is dissipated away in the smallest eddies. This cascade of eddies leads to greater diffusivity in turbulent flow, resulting in increased skin friction and heat transfer rates. The largest of these eddies are typically of the same order of magnitude as the length scale of the mean fluid flow; the smallest are microscopic in size. Thus, the range of applicable length scales in turbulent flow is extremely large. Fortunately, as noted in Wilcox (27), “the time-dependent, three-dimensional Navier Stokes equation contains all of the physics of a given

turbulent flow." Notice that turbulent fluid motion is not excluded; it too must obey the Navier-Stokes equations. That said, modeling a turbulent flow should be fundamentally no different than modeling a laminar flow; in fact turbulence will develop naturally, provided that all the pertinent length scales are captured.

But just how widely do these length scales vary? As previously noted, the largest is on the order of the characteristic length of the flowfield being modeled. The length scale associated with the smallest eddies is on the order of the Kolmogorov length scale, η_k . For wall bounded flows, the characteristic length of the flow may be taken to be the boundary layer thickness, δ . The ratio of these length scales has been found to be inversely proportional to the Reynolds number based on δ raised to the three-fourths power, or

$$\eta_k \approx \frac{\delta}{R_{\epsilon_\delta}^{\frac{3}{4}}} \quad (1.1)$$

Using this approximation, η_k for the flowfields to be studied in this investigation is estimated to be roughly 1.22×10^{-6} . Assuming that flowfield features of this length scale may be accurately resolved if the grid spacing is equal to η_k , computing the solution over 1 cubic centimeter of the flowfield would require a grid with 5.49×10^{11} nodes. With this kind of required node density, problems of a realistic size quickly become unmanageable with present day computational resources. This is the core problem in turbulence. The inability to resolve all of the pertinent length scales, all the effects of the turbulent eddies, requires that the effect of these eddies be modeled.

In present-day turbulence modeling, a statistical approach is used to solve the governing equations. In both Reynolds and Favre averaging, each flow variable is replaced by the sum of a time-averaged and a fluctuating term. Expanding and then contracting these terms (See Appendix E) produces similar sets of differential equations. These forms of the governing equations, the Reynolds- and Favre-averaged Navier-Stokes equations, contain additional fluctuation terms required to model the actions of the turbulent eddies and are the forms most frequently used in turbulent flow modeling.

1.3 "Excuse me, your Boussinesq is showing"

At the core of eddy viscosity turbulence models is the Boussinesq eddy viscosity approximation, which (27) "assumes that the principal axes of the Reynolds stress tensor, τ_{ij} are coincident with those of the mean strain-rate tensor, S_{ij} , at all points in a turbulent flow ... [where] ... the constant of proportionality between τ_{ij} and S_{ij} is the eddy viscosity, μ_T ." The ultimate goal of an eddy viscosity turbulence closure model is then to compute μ_T in such a manner as to replicate accurately the effects of the turbulent eddies on the flowfield. Dimensional arguments have been used to show that appropriate length (or time) and velocity scales are needed to specify μ_T . Two-equation turbulence models propose differential equations that govern these length scales and as such are complete models; both required scales are specified. The solution of these differential equations in terms of the scales modeled is then used to specify μ_T .

The wide range of velocity and length scales present in a turbulent flowfield necessitates the consideration of non-local flowfield influences on the local turbulent quantities. Turbulent kinetic energy models have been found to be successful at incorporating these effects. Prandtl chose the kinetic energy per unit mass of the turbulent fluctuations, k , as the basis for his velocity scale:

$$k = \frac{1}{2} \overline{u'_i u'_i} = \frac{1}{2} (\overline{u'^2} + \overline{v'^2} + \overline{w'^2}) \quad (1.2)$$

As described in Appendix E, the primed velocities in Equation 1.2 represent the Reynolds fluctuating portion of the instantaneous velocities and overbars represent time averaging. The link between k and μ_T lies in the trace of the Reynolds stress tensor (see Appendix E), which may be expressed in terms of Favre fluctuating components as

$$\tau_{ii}^T = -\rho \overline{u''_i u''_i} = -2\rho k \quad (1.3)$$

The full form of the Reynolds stress tensor is then given by

$$\tau_{ij}^T = 2\mu_T \left(S_{ij} - \frac{1}{3} \frac{\partial u_k}{\partial x_k} \delta_{ij} \right) - \frac{2}{3} \rho k \delta_{ij} \quad (1.4)$$

where the second term ensures that the trace of the Reynolds stress tensor is correct for incompressible flows, where $S_{ii} = 0$. In a similar fashion, the differential equation for k may be obtained by taking the trace of the Reynolds stress equation (27). With the velocity scale thus specified, a length scale is needed.

In 1942, Kolmogorov (see Wilcox (27)) proposed a two-equation turbulence model that used the specific dissipation of turbulent kinetic energy, ω , as its second scale. Although current trends lean towards viewing ω as the dissipation of k per unit k , ω itself is a non-physical quantity and as such, its exact definition is open for discussion. In justifying the selection of ω as the second scale, Wilcox (27), a strong proponent of the $k - \omega$ turbulence model, argues that "While the actual process of dissipation takes place in the smallest eddies, the rate of dissipation is the rate of transfer of turbulence kinetic energy to the smallest eddies. Hence, this rate is set by the properties of the large eddies, and thus scales with k and l . . ." Thus, the two scales modeled in the $k - \omega$ turbulence model are consistent; both concern themselves with the actions of the large eddies (not to be confused with Large Eddy Simulation, another turbulence modeling method, which will not be discussed here). Physical arguments have been utilized to determine the form of the governing equation for ω , which closely resembles the governing equation for k in that convection, diffusion, production, and dissipation terms are all present. Though the arguments used to determine the governing equation for ω are certainly not rigorous mathematically, in turbulence modeling the most successful models are frequently developed with more emphasis on dimensional analysis and physical reasoning than mathematical rigor.

The more popular $k - \epsilon$ turbulence model attempts to directly model the dissipation, ϵ , occurring in the smallest eddies. The governing equation for ϵ is obtained by taking a moment of the Navier-Stokes equations and involves several additional double and triple correlations. Since this equation is obtained with substantially more rigor than the equation for ω , the bulk of two-equation turbulent flow modeling has been done with this model. The model is not without flaws, however. Closing the equation for ϵ requires estimations of the aforementioned correlations, which traditionally have been very difficult to measure experimentally. Additionally, this difficulty aside, there is concern that even if it is modeled exactly, ϵ might not be the appropriate length scale, since it is the scale associated with

the dissipating eddies and not that of the Reynolds-stress bearing larger eddies. Recall that k is the velocity scale corresponding to the large-scale turbulent fluctuations.

1.4 *Flowfield Configuration*

The computations performed in this investigation simulate the flow in the AFIT supersonic pressure-vacuum wind tunnel, which operates at a nominal freestream Mach number of 2.9. In this facility, favorable and adverse pressure gradients are imposed on supersonic flow through the introduction of expansion and compression ramps, respectively, into the tunnel ceiling. In four related studies at AFIT, experimental data have been collected in these pressure gradient regions. The present numerical effort simulates these flowfields and compares the data thus generated to that obtained through the aforementioned experimental investigations.

1.5 *Summary*

The generality, completeness, and overall accuracy of two-equation turbulence models makes them attractive. The Boussinesq approximation makes their implementation into existing laminar codes easy. Due to questions regarding the basic formulation of the $k - \epsilon$ model and reports of exceptional accuracy obtained with the $k - \omega$ model (see Wilcox (26) (27), Liu and Zheng (14), Coakley and Huang (4), and Morrison (18)), the focus of this computational effort is on the $k - \omega$ model. Several different versions of the $k - \omega$ model exist; certainly Wilcox's (27) has been tested more than any other. For this investigation, however, the model presented by Coakley and Huang (4) is used. The reason behind this selection is that the model itself is fundamentally the same as Wilcox's, but the algorithm development presented in (4) is such that only minor changes are required to move from the $k - \omega$ model to a $k - \epsilon$ model or almost any other two-equation turbulence model. Thus, the final source code will serve as a valuable research tool for turbulence model development, facilitating direct comparison between results obtained with different turbulence models using the same basic flow solver.

The remainder of this thesis is structured as follows: A description of the problem geometries is presented in Chapter 2. Details of the governing equations and development

of the numeric scheme used in the mean flow and turbulence modeling portions of the source code are provided in Chapter 3. Chapter four presents results of a grid refinement study conducted to ensure grid independence in the solutions. Results of the present study are compared and contrasted with experimental data collected by Miller (16), Dotter (5) Luker (15), and Hale (9) in Chapter 5. Conclusions and recommendations, including proposed coding changes are given in Chapter 6.

II. Problem Descriptions

2.1 AFIT Mach 3 Blowdown Wind Tunnel

The computations presented in this effort simulate the flowfield within the AFIT Supersonic Pressure-Vacuum Wind Tunnel. This wind tunnel was used in previous investigations by Dotter (5) and Miller (16), who experimentally examined Mach 2.9 boundary layer flows using hot-film anemometry. Luker (15) and Hale (9) considered the same flowfields in their investigation, employing Laser Doppler Velocimetry for flowfield characterization. In the latter set of experiments, the settling chamber pressure and temperature were 2.1263×10^5 Pa and 294 K, respectively, producing a freestream Mach number at the nozzle exit of nominally 2.85 and a freestream Reynolds number $R_e/m = 1.75 \times 10^7$. All flow stations referenced in this investigation are specified in centimeters using a Cartesian coordinate system with the origin set at the nozzle throat. As such, Flow Station (FS) 71.5 corresponds to a location 71.5 cm aft of the nozzle throat. For convenience, computational meshes used in this investigation are inverted; the wind tunnel ceiling, which contains the compression (Adverse Pressure Gradient) and expansion (Favorable Pressure Gradient) ramps in the physical domain, is the floor of the computational domain.

2.2 Nozzle

Figure 2.1 is a cross section of the nozzle section used in the AFIT Supersonic Pressure-Vacuum Wind Tunnel. This contour was designed by Dr Rodney Bowersox using the method of characteristics with a boundary condition correction. The coordinates of the contour of this nozzle may be found in Appendix F.

2.3 Zero Pressure Gradient (ZPG) Test Sections

Experimental data has been collected in this test section, effectively a zero-pressure gradient (ZPG) channel flow, at FS 44.0 by Miller (16) and Luker (15). Additional ZPG data was collected by Luker (15) in a similar channel flow configuration at FS 71.5 with the pressure gradient test sections removed.

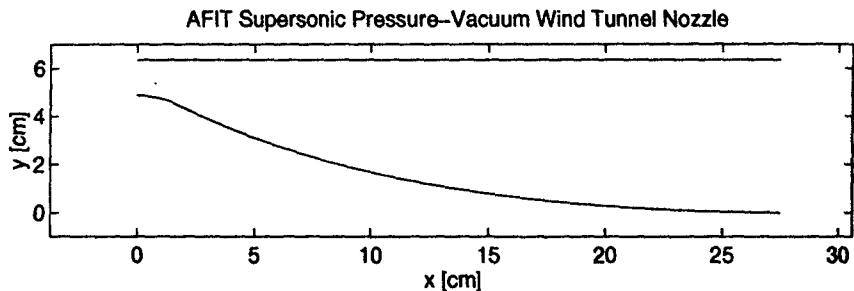


Figure 2.1 Nozzle Cross Section

2.4 Favorable Pressure Gradient (FPG) Test Section

The tunnel contour in this test section is presented in Figure 2.2 and is given by the third-order polynomial

$$Y = -0.2078 + 0.0897x - 0.009476x^2 + 0.00003598x^3 \quad (2.1)$$

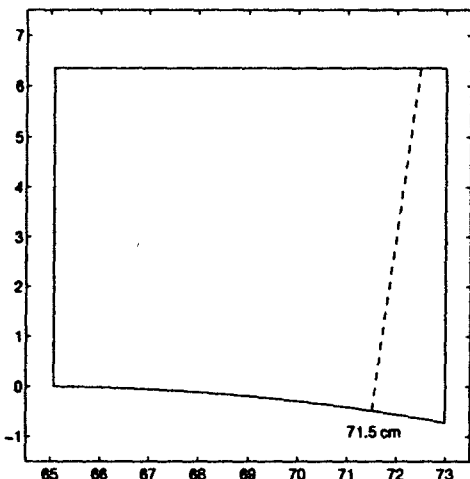


Figure 2.2 Favorable Pressure Gradient Test Section Cross Section

where x is measured in cm from the beginning of the test section (60.0 cm). Experimental data has been acquired by Miller (16) and Luker (15) at FS 71.5 in a region characterized by a mild favorable pressure gradient. This data plane is presented as the dashed line in Figure 2.2 and is locally normal to the lower surface. All flowfield quantities at this plane are represented in terms of a body normal coordinate system, defined by the dashed line and the tangent line at FS 71.5.

2.5 Adverse Pressure Gradient (APG) Test Section

Figure 2.4 presents the tunnel contour in this test section, which is given by the third-order polynomial

$$Y = 1.186 - 0.5410x + 0.07478x^2 - 0.0028x^3 \quad (2.2)$$

where x is once again measured in cm from the beginning of the test section (60.0 cm). Experimental data has been collected in this test section at FS 71.0 by both Dotter (5) and Hale (9). During the course of this investigation, however, it became obvious that FS 71.0 lies in a region whose pressure gradient is even more favorable than that referred to in Section 2.4, as may be seen in Figure 2.3. This figure shows the computed static pressure along the surface of the contours of both test sections; indicating that the pressure gradient at FS 71.0 of the APG test section is indeed favorable. Using this figure to guide further experiments, Hale (9) obtained additional data at FS 68.0, well within the APG region.

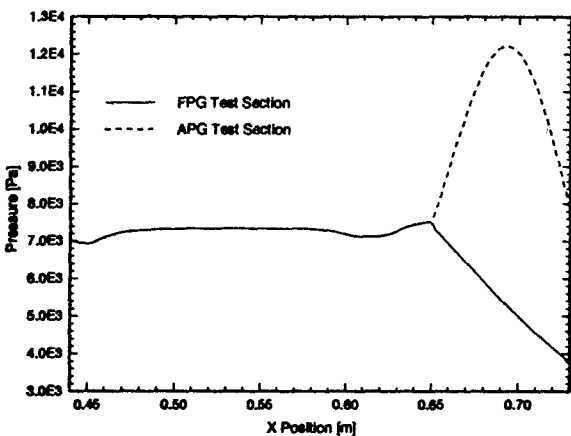


Figure 2.3 Surface Pressure in Test Sections

The planes of data examined experimentally are shown by the dotted and dashed lines in Figure 2.4. Once again, a body normal coordinate system is used for data output.

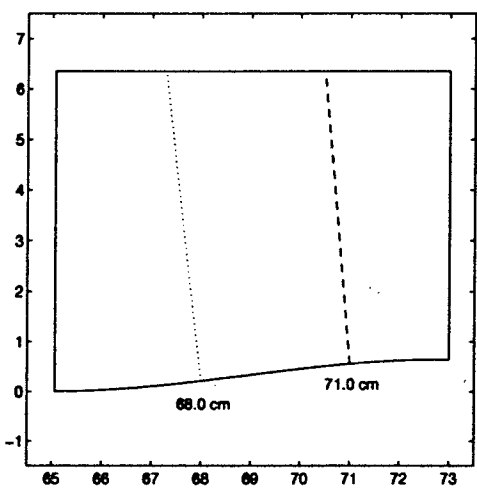


Figure 2.4 Adverse Pressure Gradient Test Section Cross Section

III. Numerical Formulation

3.1 Governing Equations

Within the field of fluid mechanics, conservation of mass, momentum, and energy may be expressed through the Navier-Stokes equations, which may be written (in Cartesian coordinates for two-dimensional flow) as:

$$U_t + F_x + G_y = 0 \quad (3.1)$$

The solution vector is given by

$$U = \begin{pmatrix} \rho \\ \rho u \\ \rho v \\ E_t \end{pmatrix} \quad (3.2)$$

and the flux vectors in the x and y coordinate directions are

$$F = \begin{pmatrix} \rho u \\ \rho u^2 + p - \tau_{xx} \\ \rho uv - \tau_{xy} \\ (E_t + p)u - u\tau_{xx} - v\tau_{xy} + q_x \end{pmatrix} \quad (3.3)$$

$$G = \begin{pmatrix} \rho v \\ \rho uv - \tau_{xy} \\ \rho v^2 + p - \tau_{yy} \\ (E_t + p)v - u\tau_{xy} - v\tau_{yy} + q_y \end{pmatrix} \quad (3.4)$$

In the above formulation, E_t is the total energy per unit volume and is given by

$$E_t = \rho \left(e + \frac{u^2 + v^2}{2} \right) \quad (3.5)$$

where e is the internal energy per unit mass. The viscous stresses and heat fluxes are given by

$$\tau_{ij} = \mu \left[\left(\frac{\partial u_i}{\partial x_j} + \frac{\partial u_j}{\partial x_i} \right) - \frac{2}{3} \delta_{ij} \frac{\partial u_k}{\partial x_k} \right] \quad i, j, k = 1, 2 \quad (3.6)$$

and

$$q_x = (-\kappa T)_x \quad q_y = (-\kappa T)_y \quad (3.7)$$

Equation 3.1 is a system of four equations in eight unknowns, those being ρ , u , v , p , e , μ , T , and κ . Thus, four additional relations are required to close the system. Three of these come from Sutherland's law and the assumptions of thermally and calorically perfect gases:

$$p = \rho RT \quad (3.8)$$

$$e = c_v T \quad (3.9)$$

$$\mu = C_1 \frac{T^{3/2}}{T + C_2} \quad (3.10)$$

where R is the gas constant, c_v is the specific heat at constant volume, and C_1 and C_2 are constant for a given gas. Assuming that the specific heat at constant pressure, c_p , and the Prandtl number, Pr , are constant for the flows being considered, the final relation comes from the definition of the Prandtl number:

$$Pr = \frac{c_p \mu}{\kappa} \quad (3.11)$$

3.2 Algorithm Development

This section describes the algorithm used within Flat Plate Finite Volume (FPFV), the driver code utilized and modified in this investigation. FPFV operates on the two-dimensional Navier-Stokes equations in general curvilinear coordinates using a cell-centered, finite volume approach. This code was originally developed and validated for high-speed viscous flows by Dr. Datta Gaitonde (8) (6).

The form of the governing equations given in the preceding section is not amenable to solution on uneven computational meshes. Transforming the uneven physical domain $((x, y)$ space) into an even computational domain $((\xi, \eta)$ space) allows the equations to be more readily solved. As the physical space is transformed into computational space, so must the governing equations be transformed. The set of equations thus obtained is referred to as the strong conservation form of the governing equations, the derivation of which may be found in Appendix A.

Beginning with the strong conservation form of the governing equations

$$\frac{U_t}{J} + \bar{F}_\xi + \bar{G}_\eta = 0 \quad (3.12)$$

the dissipative viscous terms are separated from the convective terms to yield the form

$$\frac{1}{J} \frac{\partial U}{\partial t} + \frac{\partial \bar{F}_{inv}}{\partial \xi} + \frac{\partial \bar{G}_{inv}}{\partial \eta} + \frac{\partial \bar{F}_v}{\partial \xi} + \frac{\partial \bar{G}_v}{\partial \eta} = 0 \quad (3.13)$$

where

$$\bar{F}_{inv} = \frac{1}{J} \begin{bmatrix} \rho u \xi_x + \rho v \xi_y \\ (\rho u^2 + p) \xi_x + \rho u v \xi_y \\ \rho u v \xi_x + (\rho v^2 + p) \xi_y \\ (E_i + p) u \xi_x + (E_i + p) v \xi_y \end{bmatrix} \quad (3.14)$$

$$\bar{F}_v = \frac{1}{J} \begin{bmatrix} 0 \\ -\tau_{xx}\xi_x - \tau_{xy}\xi_y \\ -\tau_{xy}\xi_x - \tau_{yy}\xi_y \\ (-u\tau_{xx} - v\tau_{xy} + q_x)\xi_x + (-u\tau_{xy} - v\tau_{yy} + q_y)\xi_y \end{bmatrix} \quad (3.15)$$

$$\bar{G}_{inv} = \frac{1}{J} \begin{bmatrix} \rho u \eta_x + \rho v \eta_y \\ (\rho u^2 + p) \eta_x + \rho u v \eta_y \\ \rho u v \eta_x + (\rho v^2 + p) \eta_y \\ (E_t + p) u \eta_x + (E_t + p) v \eta_y \end{bmatrix} \quad (3.16)$$

$$\bar{G}_v = \frac{1}{J} \begin{bmatrix} 0 \\ -\tau_{xx} \eta_x - \tau_{xy} \eta_y \\ -\tau_{xy} \eta_x - \tau_{yy} \eta_y \\ (-u\tau_{xx} - v\tau_{xy} + q_x)\eta_x + (-u\tau_{xy} - v\tau_{yy} + q_y)\eta_y \end{bmatrix} \quad (3.17)$$

Using Δ to represent spatial finite differences, Equation 3.13 may be further re-written as

$$\frac{\delta U}{J\delta t} + \frac{\Delta \bar{F}_{inv}}{\Delta \xi} + \frac{\Delta \bar{G}_{inv}}{\Delta \eta} + \frac{\Delta \bar{F}_v}{\Delta \xi} + \frac{\Delta \bar{G}_v}{\Delta \eta} = 0 \quad (3.18)$$

where

$$\delta U = U^{n+1} - U^n \quad (3.19)$$

where U^n represents the solution at the current time step and U^{n+1} represents the solution at the next time step. Since the computational domain is uniform with $\Delta\xi = \Delta\eta = 1.0$, Equation 3.18 may be re-written yet again as

$$\frac{U_{i,j}^{n+1} - U_{i,j}^n}{J_{i,j} \delta t_{i,j}} + \Delta \bar{F}_{inv,i,j} + \Delta \bar{G}_{inv,i,j} + \Delta \bar{F}_{v,i,j} + \Delta \bar{G}_{v,i,j} = 0 \quad (3.20)$$

Solving for the update to the solution δU based on the current state of the flux vectors yields

$$\delta U_{i,j} = U_{i,j}^{n+1} - U_{i,j}^n = -J_{i,j} \delta t_{i,j} \left[\Delta \bar{F}_{inv,i,j}^n + \Delta \bar{G}_{inv,i,j}^n + \Delta \bar{F}_{v,i,j}^n + \Delta \bar{G}_{v,i,j}^n \right] \quad (3.21)$$

In the present computational effort, this equation is solved using a cell-centered, finite-volume approach in which the conserved quantities ($\rho, \rho u, \rho v, E_t$) are stored at cell centers. Note that the formulation in Equation 3.21 may be obtained through the use of a classical finite-volume approach (10) on a uniform computational mesh, as can be found in Appendix B.

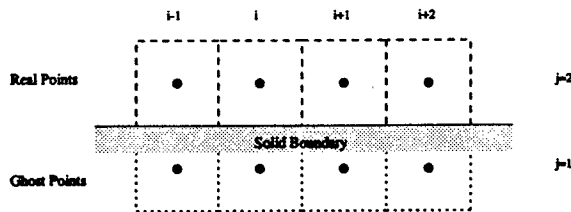


Figure 3.1 Cell Configuration Along a Solid Wall Boundary

3.2.1 Boundary Conditions. As the name suggests, cell-centered, finite-volume codes store no flowfield information at the cell interfaces. Specification of boundary conditions poses special difficulties for these codes since cell interfaces, not cell centers, lie on the boundaries of the physical and computational domains. To address this difficulty, “ghost points” (see Figure 3.1) may be created outside the physical domain and their values set to enforce the condition at the interface (surface). In this effort, the physical domain is broken into a mesh consisting of $(il - 2) \times (jl - 2)$ cells with nodes 2 through $(il - 1)$ in the ξ direction (2 through $(jl - 1)$ in the η direction) treated as interior nodes. The ghost points are assigned indices of 1 and il in the ξ direction and 1 and jl in the η direction.

The boundary conditions imposed at a non-moving impermeable wall may be expressed in the following manner: No slip and no penetration are specified by setting u and v at the wall equal to zero. This is accomplished by specifying that the ghost point velocities are equal in magnitude and opposite in direction to the corresponding velocities inside the physical domain:

$$u|_{wall} = 0 : u_{i,1} = -u_{i,2}$$

$$v|_{wall} = 0 : v_{i,1} = -v_{i,2}$$

In specifying an isothermal wall boundary condition, the internal energy at the ghost point is extrapolated using the specified wall temperature and the internal energy at the first node inside the physical domain. The isobaric wall boundary condition, $\frac{\partial p}{\partial n} = 0$, requires that the static pressure at the ghost point be equal to the static pressure just inside the physical domain:

$$T|_{wall} = T_{wall} : e_{i,1} = 2c_v T_{wall} - e_{i,2}$$

$$\frac{\partial p}{\partial n}|_{wall} = 0 : p_{i,1} = p_{i,2}$$

Other pertinent flowfield properties ($\rho, \rho u, \rho v, E_t, \mu$) are obtained from these specified values. Inflow boundary conditions are specified by explicitly setting flowfield properties at the upstream ghost points:

$$\rho_{1,j} = \rho_\infty$$

$$u_{1,j} = u_\infty$$

$$v_{1,j} = v_\infty$$

$$e_{1,j} = c_v T_\infty$$

$$p_{1,j} = p_\infty$$

where once again, ρu , ρv , E_t , and μ are specified through the use of these values with the governing equations listed in Section 3.1. Details concerning the specific implementation of the upstream boundary conditions are presented in Section 4.6. Downstream ghost point values are extrapolated using the values at the last two interior nodes to define a rate of change of each flow property, which is then used to set flowfield quantities at the ghost points:

$$\begin{aligned}
\rho_{il,j} &= 2u_{il-1,j} - u_{il-2,j} \\
\rho u_{il,j} &= 2\rho u_{il-1,j} - \rho u_{il-2,j} \\
\rho v_{il,j} &= 2\rho v_{il-1,j} - \rho v_{il-2,j} \\
p_{il,j} &= 2p_{il-1,j} - p_{il-2,j} \\
u_{il,j} &= \frac{\rho u_{il,j}}{\rho_{il,j}} \\
v_{il,j} &= \frac{\rho v_{il,j}}{\rho_{il,j}} \\
e_{il,j} &= \frac{c_v p_{il,j}}{\rho_{il,j} R} \\
E_{t,il,j} &= \rho \left(e_{il,j} + \frac{u_{il,j}^2 + v_{il,j}^2}{2} \right)
\end{aligned}$$

3.2.2 Implementation. The flowfield is initialized using either a uniform or one-dimensional approximation of initial flowfield properties. The next step, the first in an iterative series of steps, is to scan the flowfield to establish either a local or global δt based on a specified maximum CFL number, the magnitude of the mean flow eigenvalues, and the cell size. After δt (potentially $\delta t_{i,j}$) has been determined, computational sweeps on the interior nodes begin by fixing j and sweeping $2 \leq i \leq (il - 1)$. In this sweep, denoted the ξ sweep, the left and right states at the cell's Eastern interface are extrapolated using both upstream and downstream flow information. MINMOD limiting (28) is used in conjunction with flowfield information from the i , $(i + 1)$, and $(i - 1)$ cells to establish the left state; the right state uses the same limiting logic with flowfield information from the i , $(i + 1)$ and $(i + 2)$ cells. In this application, ρ , ρu , ρv and p are extrapolated; other flowfield properties are obtained from these extrapolated quantities. The choice of the extrapolated variables has a large impact on the behavior of the algorithm; extrapolating these variables provides the best overall flowfield behavior. See Appendix C for an explanation of the extrapolation and limiting procedure. The left and right states are combined using Roe's flux-difference splitting (18) to obtain the inviscid flux at the East interface of each cell. Central differences about the cell interface are used to obtain the viscous fluxes (including the turbulent contributions from μ_T and κ_T) at the East interface, which are added to the previously calculated inviscid fluxes. At this point the contribution of the East and West fluxes to δU is calculated as shown below.

$$\delta \widetilde{U}_{i,j} = J_{i,j} \delta t_{i,j} \left[\overline{F}_{inv,i-1,j}^n - \overline{F}_{inv,i,j}^n + \overline{F}_{v,i-1,j}^n - \overline{F}_{v,i,j}^n \right] \quad (3.22)$$

The η sweep begins by fixing i and sweeping $2 \leq j \leq (jl - 1)$. The manipulations performed in the η sweep are effectively identical to those performed in the ξ sweep except that the states are established at the North interface of each cell, and flux boundary conditions are enforced at solid wall boundaries. These conditions supplement the boundary conditions enforced explicitly at the end of each step. The flux boundary conditions enforced at these solid wall boundaries are

$$\overline{G} = \begin{bmatrix} 0 \\ -py_\xi \\ px_\xi \\ 0 \end{bmatrix} \quad (3.23)$$

reflecting $u = v = 0$ at the stationary, impermeable walls. At the conclusion of these sweeps, the contribution of the North and South fluxes to δU is calculated and added to that previously established:

$$\delta U_{i,j} = \delta \widetilde{U}_{i,j} + J_{i,j} \delta t_{i,j} \left[\overline{G}_{inv,i,j}^n - \overline{G}_{inv,i,j+1}^n + \overline{G}_{v,i,j}^n - \overline{G}_{v,i,j+1}^n \right] \quad (3.24)$$

Using the δU vector calculated above, the flowfield is updated by setting

$$\hat{U}_{i,j} = U_{i,j} + \delta U_{i,j}^{(1)} \quad (3.25)$$

At this point, the residual is evaluated to determine the extent to which the flow has converged. The flowfield residual is defined as

$$RESID \equiv \frac{\sqrt{\sum_{\text{interior nodes}} \frac{\left(\frac{\Delta \rho}{\rho}\right)_{i,j}^2 + \left(\frac{\Delta \rho u}{\rho u}\right)_{i,j}^2 + \left(\frac{\Delta \rho v}{\rho v}\right)_{i,j}^2 + \left(\frac{\Delta E_t}{E_t}\right)_{i,j}^2}{\left(\frac{\Delta f}{f}\right)_{i,j}^2}}}{(il - 2)(jl - 2)} \quad (3.26)$$

Following this calculation, the mean flow boundary conditions are updated explicitly as described in Section 3.2.1.

If desired, the above procedure may be executed twice at each time step, allowing the code to operate in a predictor-corrector mode. After the second set of sweeps, the solution is updated by setting

$$U_{i,j} = \frac{\hat{U}_{i,j} + U_{i,j} + \delta U_{i,j}^{(2)}}{2} \quad (3.27)$$

with the residual evaluated in exactly the same manner as before. If only one sweep through the computational domain is desired, then

$$U_{i,j} = \hat{U}_{i,j} \quad (3.28)$$

If the flowfield under consideration is turbulent, μ_T and κ_T are updated at this point using either the Baldwin-Lomax or $k - \omega$ turbulence model. Descriptions of these turbulence models are found in Sections 3.3.1 and 3.3.2, respectively. When the ratio of the residual calculated in Equation 3.26 to the first residual is below a specified threshold, calculations are halted and the flowfield is deemed converged.

3.3 Turbulence Modeling

Turbulence modeling in FPFV is accomplished through the use of either the Baldwin-Lomax algebraic turbulence model or the $k - \omega$ two equation turbulence model. Both are eddy viscosity models, making their incorporation into existing laminar codes a relatively straightforward exercise. In eddy viscosity turbulence models, the governing equations are modified through the addition of eddy viscosity and eddy thermal conductivity coefficients to the already existing thermophysical viscosity and thermal conductivity coefficients, as seen below

$$\bar{\mu} \equiv \mu + \mu_T \quad \bar{\kappa} \equiv \kappa + \kappa_T \quad (3.29)$$

where

$$\kappa_T \equiv \frac{c_p \mu_T}{Pr_T} \quad (3.30)$$

and Pr_T is the turbulent Prandtl number, considered to be a constant for a given fluid. As is common practice for air at the temperatures considered in this study (see Coakley (4), Wilcox (27), and White (25)), a value of 0.90 has been assumed.

3.3.1 Baldwin - Lomax Turbulence Model. The choice of an algebraic turbulence model as the “other” model to be implemented in this effort is based on the well documented features of this flowfield. The work of Miller (16) and Dotter (5) established that the test sections are separation-free, meaning that simpler algebraic turbulence models should do a fair job at computing the flowfield. The results from computations performed with this model may serve then as an additional reference point for the validation of the more complex $k - \omega$ model. The Baldwin-Lomax turbulence model is a two-layer eddy viscosity model, incorporating different formulations for the eddy viscosity for the inner and outer regions of the boundary layer. To that end, the eddy viscosity is defined as

$$\mu_T = \begin{cases} \mu_{T_i} & y \leq y_m \\ \mu_{T_o} & y > y_m \end{cases} \quad (3.31)$$

where y_m is the first point away from the wall at which $\mu_{T_i} = \mu_{T_o}$. This model was incorporated in accordance with the formulation described in Wilcox (27). The sections below describe the formulations in each of these regions

3.3.1.1 Inner Region. The inner region uses a basic mixing length model

$$\mu_{T_i} = \rho l_{mix}^2 |\omega_{BL}| \quad (3.32)$$

where ω is the magnitude of the vorticity vector and is defined for two-dimensional flow as

$$\omega_{BL} \equiv \left[\left(\frac{\partial v}{\partial x} - \frac{\partial u}{\partial y} \right)^2 \right]^{1/2} \quad (3.33)$$

and the mixing length is defined as

$$l_{mix} = \kappa_{BL} y \left(1 - e^{\frac{-y^+}{A^+}} \right) \quad (3.34)$$

with

$$A^+ = 26.0$$

$$y^+ \equiv \frac{\rho u^* y}{\mu} \quad (3.35)$$

$$u^* \equiv \sqrt{\frac{\tau_{wall}}{\rho_{wall}}} \quad (3.36)$$

$$\tau_{wall} = \mu \left(\frac{\partial u}{\partial y} + \frac{\partial v}{\partial x} \right) \Big|_{wall} \quad (3.37)$$

3.3.1.2 Outer Region. In the outer region, the Baldwin-Lomax model uses the vorticity in the boundary layer to determine the length scale, giving

$$\mu_{T_0} = \rho \alpha C_{cp} F_{wake} F_{Kleb} \left(y; \frac{y_{max}}{C_{Kleb}} \right) \quad (3.38)$$

where

$$F_{Kleb}(y; \delta) = \left[1 + 5.5 \left(\frac{y}{\delta} \right)^6 \right]^{-1} \quad (3.39)$$

$$F_{wake} = \min \left[y_{max} F_{max}; C_{wk} y_{max} \frac{U_{diff}^2}{F_{max}} \right] \quad (3.40)$$

$$F_{max} = \frac{1}{\kappa_{BL}} \left[\max_{\forall y} (l_{mix} |\omega_{BL}|) \right] \quad (3.41)$$

and y_{max} is the y location at which F_{max} is evaluated. Traditionally, U_{dif} is the maximum value of U for boundary layer flows. In this application, U_{dif} is chosen to be the centerline velocity. Additional closure coefficients, taken from Wilcox (27), are as follows

$$C_{kleb} = 0.3$$

$$C_{cp} = 1.6$$

$$C_{wk} = 1.0$$

$$\alpha = 0.0168$$

$$\kappa_{BL} = 0.41$$

Note that $A^+ = 26$ is "rigorously" valid only for zero pressure gradient flows; modifications may be made to enhance the performance of this method in the presence of strong pressure gradients (25). In this investigation, the pressure gradients are mild and the aforementioned modification has not been made.

3.3.1.3 Implementation. The flowfields under consideration are treated as horizontally opposed flat plate flows. Therefore, at each i -plane in the computational domain two sweeps are used to calculate μ_T . The first sweep begins at the top wall, calculating μ_{T_i} from the wall to the centerline from above. Following this calculation, μ_{T_0} is calculated over the same range of nodes and compared to μ_{T_i} at each node. The stored values for μ_T in the upper half of the computational domain are then determined through the rule given in Equation 3.31. The above procedure is repeated on the bottom half of the computational domain, with the sweeps moving from the lower wall to the centerline from below. In this application, y is taken to be the normal distance from the node in question to the node on the wall at that i -plane. Calculation of μ_T progresses in this manner through the computational domain one i -plane at a time after each mean flow update.

3.3.2 $k - \omega$ Turbulence Model. As described in Coakley and Huang (4) the governing differential equation for the $k - \omega$ turbulence model may be written as

$$\frac{\partial U_{KE}}{\partial t} + \frac{\partial F_{KE,inv}}{\partial x} + \frac{\partial G_{KE,inv}}{\partial y} + \frac{\partial F_{KE,v}}{\partial x} + \frac{\partial G_{KE,v}}{\partial y} = P \quad (3.42)$$

with

$$U_{KE} = \begin{bmatrix} \rho k \\ \rho \omega \end{bmatrix} \quad (3.43)$$

$$F_{KE,inv} = \begin{bmatrix} \rho u k \\ \rho u \omega \end{bmatrix} \quad (3.44)$$

$$G_{KE,inv} = \begin{bmatrix} \rho v k \\ \rho v \omega \end{bmatrix} \quad (3.45)$$

$$F_{KE,v} = \begin{bmatrix} -\left(\mu + \frac{\mu_T}{\sigma_k}\right) \frac{\partial k}{\partial x} \\ -\left(\mu + \frac{\mu_T}{\sigma_\omega}\right) \frac{\partial \omega}{\partial x} \end{bmatrix} \quad (3.46)$$

$$G_{KE,v} = \begin{bmatrix} -\left(\mu + \frac{\mu_T}{\sigma_k}\right) \frac{\partial k}{\partial y} \\ -\left(\mu + \frac{\mu_T}{\sigma_\omega}\right) \frac{\partial \omega}{\partial y} \end{bmatrix} \quad (3.47)$$

$$P = \begin{bmatrix} \left[C_{k1} C_\mu f_k \left(\frac{S}{\omega} \right)^2 - \frac{\alpha_k D}{\omega} - C_{k2} \right] \rho \omega k \\ \left[C_{\omega 1} C_\mu f_\omega \left(\frac{S}{\omega} \right)^2 - \frac{\alpha_\omega D}{\omega} - C_{\omega 2} \right] \rho \omega^2 \end{bmatrix} \quad (3.48)$$

$$S^2 = \left(\frac{\partial u}{\partial y} \right)^2 + 2 \left(\frac{\partial u}{\partial y} \right) \left(\frac{\partial v}{\partial x} \right) + \left(\frac{\partial v}{\partial x} \right)^2 + \frac{4}{3} \left[\left(\frac{\partial u}{\partial x} \right)^2 - \left(\frac{\partial u}{\partial x} \right) \left(\frac{\partial v}{\partial y} \right) + \left(\frac{\partial v}{\partial y} \right)^2 \right] \quad (3.49)$$

$$D = \frac{\partial u}{\partial x} + \frac{\partial v}{\partial y} \quad (3.50)$$

with closure coefficients given by

$$\sigma_k = \sigma_\omega = 2.0$$

$$f_k = f_\omega = f = 1.0$$

$$\alpha_k = \frac{2}{3} C_{k1}$$

$$\alpha_\omega = \frac{2}{3} C_{\omega 1}$$

$$C_{k1} = C_{k2} = 1.0$$

$$C_{\omega 1} = 0.555$$

$$C_{\omega 2} = 0.833$$

Following the solution of these differential equations, the eddy viscosity may be obtained through the following relation

$$\mu_T = C_\mu f \rho \frac{k}{\omega} \quad (3.51)$$

with $C_\mu = 0.09$

3.3.2.1 Algorithm Development. The transformation of the governing equations for the $k - \omega$ turbulence model into strong conservation form is analogous to the transformation of the governing mean flow equations. The resulting form of the equations is

$$\frac{1}{J} \frac{\partial U_{KE}}{\partial t} + \frac{\partial \bar{\bar{F}}_{inv}}{\partial \xi} + \frac{\partial \bar{\bar{G}}_{inv}}{\partial \eta} + \frac{\partial \bar{\bar{F}}_v}{\partial \xi} + \frac{\partial \bar{\bar{G}}_v}{\partial \eta} = \frac{P}{J} \quad (3.52)$$

where

$$\begin{aligned} \bar{\bar{F}}_{inv} &= \frac{\xi_x F_{KE,inv} + \xi_y G_{KE,inv}}{J} & \bar{\bar{G}}_{inv} &= \frac{\eta_x F_{KE,inv} + \eta_y G_{KE,inv}}{J} \\ \bar{\bar{F}}_v &= \frac{\xi_x F_{KE,visc} + \xi_y G_{KE,visc}}{J} & \bar{\bar{G}}_v &= \frac{\eta_x F_{KE,visc} + \eta_y G_{KE,visc}}{J} \end{aligned} \quad (3.53)$$

As in Equation 3.18, Δ is used to represent spatial differentiation, allowing Equation 3.52 to be written in finite-difference form as

$$\frac{\delta U_{KE}}{J\delta t} + \frac{\Delta \bar{F}_{inv}}{\Delta \xi} + \frac{\Delta \bar{G}_{inv}}{\Delta \eta} + \frac{\Delta \bar{F}_v}{\Delta \xi} + \frac{\Delta \bar{G}_v}{\Delta \eta} = \frac{P}{J} \quad (3.54)$$

Defining δU_{KE} as had been done previously with δU in Equation 3.19, multiplying through by $J\delta t$, taking advantage of the uniform and unitary the computational domain, and evaluating the flux vectors and source term, P , at the current time step, Equation 3.54 may be re-written as

$$\delta U_{KE,i,j} = P^n \delta t_{i,j} - J_{i,j} \delta t_{i,j} [\Delta \bar{F}_{inv,i,j}^n + \Delta \bar{G}_{inv,i,j}^n + \Delta \bar{F}_{v,i,j}^n + \Delta \bar{G}_{v,i,j}^n] \quad (3.55)$$

With all flow and turbulence properties known at time level n , updating the solution involves evaluation of the above equation at each cell.

3.3.2.2 Boundary Conditions. Boundary conditions in this application are implemented in accordance with the algorithm description given in Coakley and Huang (4). At an impermeable wall, the governing equations for k and ω must satisfy

$$k = 0 \quad (3.56)$$

$$\omega_1 = 7.2 \frac{\nu_1}{y_1^2} \quad (3.57)$$

In Equation 3.57, the subscript 1 refers to the first calculated data point above the wall and y is the normal distance from the wall to that data point. Inflow or freestream conditions must satisfy the somewhat more ambiguous conditions

$$\left(\frac{\mu_T}{\mu} \right)_\infty = \left(\frac{C_\mu k}{\nu \omega} \right)_\infty \leq 1.0 \quad (3.58)$$

$$\omega_\infty \geq 10 \frac{u_\infty}{L} \quad (3.59)$$

where L is a characteristic length of the flow field, taken to be 1 m in the present investigation. For the present calculations, discussions with Dr Gaitonde (7) lead these boundary conditions to the form

$$k_\infty = 0.001 \frac{(\nu\omega)_\infty}{C_\mu} \quad (3.60)$$

$$\omega_\infty = 10 \frac{u_\infty}{L} \quad (3.61)$$

3.3.2.3 Implementation. The procedure by which the governing equations for the $k - \omega$ turbulence model are marched to convergence is essentially identical to that used for the mean flow. As in the mean flow equations, the conserved variables (ρk and $\rho\omega$) are extrapolated to the cell faces using MINMOD limiting and the resulting fluxes established through the use of Roe flux-difference splitting (18). The viscous terms are once again treated with central differences and, as stated previously, the source terms are evaluated at the present time level.

The boundary conditions are treated in a similar manner. At the solid wall boundaries, Equation 3.56 is enforced by setting

$$k_{i,1} = -k_{i,2} \quad (3.62)$$

Since the ω solid wall boundary condition is not actually enforced at the wall, but at the point immediately above the wall, Equation 3.57 is implemented by setting

$$\omega_{i,2} = 7.2 \frac{\nu_{i,2}}{y_1^2} \quad (3.63)$$

where y_1 is the normal distance from the wall to the cell center of node $(i, 2)$. Inflow boundary conditions are set using the methodology outlined in Section 4.6. Downstream or outflow boundary conditions are set by extrapolating k and ω using the previous two upstream points in a manner reminiscent of the mean flow calculations. Subsequent to the

evaluation of the boundary conditions on k and ω , μ_T is evaluated through the functional form given in equation 3.51.

IV. Grid Refinement and Flat-Plate Validation

A grid study was conducted to ensure that the computed results are not grid dependent. For this study, a series of 9 grids were examined to determine the effects of grid properties on the computed solutions. The properties of the grids studied may be found in Table 4.1. The grids itemized in this table begin at Flow Station (FS) 27.457, corresponding to the nozzle exit plane, and extend to FS 73.0, aft of the favorable pressure gradient test (FPG) section. Flowfield properties are examined both upstream at FS 44.0 and in the FPG test section at FS 71.5. For the purposes of this grid study, the upstream boundary conditions reflect a $M = 2.9$, $R_e/m = 1.5 \times 10^7$ uniform flow with zero boundary layer thickness and $T_{wall} = T_0 = 294K$ impinging on the leading edge of the grid. These conditions reflect the freestream conditions reported by Miller (16) and Dotter (5).

GRIDGEN2D revision 8.4.7.1 was utilized for the grid generation task in this effort. Node stretching normal to the wall was accomplished within GRIDGEN2D using Vinokur's weighting factor. Initial wall spacings are the same at the North and South grid boundaries and are as given in Table 4.1. Spacing in the streamwise direction is uniform. Grids were generated algebraically using the arclength-based Trans-Finite Interpolation (TFI) option and smoothed elliptically using the Thomas and Middlecoff background control function. Transverse node spacing was held constant through the smoothing process, which enforced orthogonality at domain boundaries and utilized exponential blending between boundary and interior points. Grids were smoothed elliptically until the residual dropped below 1.0×10^{-9} .

The effects of variations in streamwise and normal node count on non-dimensional velocity and turbulent shear stress profiles and law of the wall plots are discussed in this chapter. An assessment of the sensitivity of the computed solution to the initial wall spacing is also included.

4.1 Variation in Normal Node Count

The effect of normal node count variation is studied by doubling the normal node count, utilizing grids GS1, GS2, and GS3. Streamwise spacing in all three grids is uniform,

Table 4.1 Dimensions - Grid Study Meshes

Reference	Size $\xi \times \eta$	Δy_{wall} [m]	$\Delta y_{mid,L}$ [m]	$\Delta y_{mid,R}$ [m]	Δx [m]
GS1	101 x 101	1.5×10^{-5}	0.2047×10^{-2}	0.2325×10^{-2}	0.4605×10^{-2}
GS2	101 x 151	1.5×10^{-5}	0.1253×10^{-2}	0.1425×10^{-2}	0.4605×10^{-2}
GS3	101 x 201	1.5×10^{-5}	0.8814×10^{-3}	0.1004×10^{-2}	0.4605×10^{-2}
GS4	75 x 151	1.5×10^{-5}	0.1253×10^{-2}	0.1425×10^{-2}	0.6244×10^{-2}
GS5	151 x 151	1.5×10^{-5}	0.1253×10^{-2}	0.1425×10^{-2}	0.3059×10^{-2}
GS6	201 x 151	1.5×10^{-5}	0.1253×10^{-2}	0.1425×10^{-2}	0.2291×10^{-2}
GS7	101 x 151	0.5×10^{-5}	0.1527×10^{-2}	0.1730×10^{-2}	0.4605×10^{-2}
GS8	101 x 151	1.0×10^{-5}	0.1354×10^{-2}	0.1538×10^{-2}	0.4605×10^{-2}
GS9	101 x 151	2.0×10^{-5}	0.1180×10^{-2}	0.1344×10^{-2}	0.4605×10^{-2}

and the initial wall spacing is 1.5×10^{-5} m, calculated to provide y^+ values near 1.0 in the test sections. All figures referred to in this section may be found in Appendix G.

Figures G.1 and G.2 show the influence of normal node count on the wall law plot, which plots u^+ as a function of y^+ , where u^+ is based on the effective velocity as defined by van Driest (25)

$$\bar{u}_{eff} = \int_0^{\bar{u}} \left(\frac{\bar{\rho}}{\rho_{wall}} \right)^{\frac{1}{2}} d\bar{u} \quad (4.1)$$

Differences between the three grids are very slight in the inner region, which may be attributed to the fact that initial node spacing is held constant for all three. Grid GS1 separates itself from the others in the logarithmic and wake regions, where GS2 and GS3 continue to agree very closely. Nondimensional velocity profiles in these two regions exhibit the same basic trends. Figure G.3 and Figure G.4 are plots of the nondimensional velocity through the boundary layer. The boundary layer thickness, δ_u , is the location at which $u = 0.995U_e$, where U_e is the edge velocity at the flow station of interest. Agreement between the three solutions is good near the wall; once again the coarser grid does not do well away from the wall, where the disparity between that solution and the others reaches 0.5%. Comparisons of the nondimensional turbulent shear stress profiles

$$\tau_{xy,ND}^T = \frac{\mu_T \left(\frac{\partial u}{\partial y} + \frac{\partial v}{\partial x} \right)}{\rho u^2} \quad (4.2)$$

where μ_T is the eddy viscosity, as defined in Chapter III, are shown in Figures G.5 and G.6. Once again, differences between grids GS2 and GS3 are negligible. The figures discussed above indicate that while 101 normal nodes is insufficient for accurate flowfield computation, increasing the normal node count beyond 151 nodes has a negligible effect on computational accuracy. For this reason, the bulk of the computations performed hereafter utilize 151 nodes in the normal direction.

4.2 Variation in Streamwise Node Count

In this section the effects of variations in streamwise node count are studied by examining computational output generated on grids GS2, GS4, GS5, and GS6. Uniform streamwise spacing is once again used for the four grids considered, which range in size from 75x151 ($\Delta x = .6244\text{cm}$), to 201x151 ($\Delta x = .2291\text{cm}$). Initial wall spacing for all grids is once again $1.5 \times 10^{-5} \text{ m}$.

Figures G.7 and G.8 are wall law plots for the upstream flat plate and favorable pressure gradient test sections, respectively. With the exception of the extremely coarse 75x151 grid, axial node distribution seems to have no effect on the flowfield properties in the flat-plate region. Figure G.8, however, shows that at FS 71.5 in the FPG test section, axial node count has a more noticeable effect on the solution in the inner and overlap regions. The difference disappears away from the wall and thus seems to be linked to poor resolution of the curvature of the wall. The nondimensional velocity profiles in Figure G.7 and Figure G.8 show little sensitivity to the streamwise node count, as do the nondimensional turbulent shear stress profiles shown in Figures G.11 and Figure G.12.

In order to improve resolution in the curved wall region without wasting grid points upstream, a non-uniform node spacing scheme is adopted in the final grid generation task.

4.3 Variation in Wall Spacing

In this section, computations performed on grids GS2, GS7, GS8, and GS9 are used to determine the flowfield effects of initial wall spacing variations. Uniform streamwise spacing is used, and the initial wall spacing is varied from 0.5×10^{-5} m to 2.0×10^{-5} m. The effect of wall spacing on the wall law plots may be seen in Figures G.13 and G.14 for flow stations 44.0 and 71.5, respectively. These figures clearly show that the initial wall spacing has an effect on the computed solution. At FS 44.0, the profiles generated using grid GS9 are appreciably different from the remainder of the grids. Moving to FS 71.5, this difference diminishes, but does not disappear. Figure G.15 and Figure G.16 show the effect of wall spacing variation on the nondimensional velocity profiles. Once again, differences at FS 44.0 are greater than those at FS 71.5, and both curves show close agreement between all solutions near the wall. Figures G.17 and G.18 serve only to reinforce the previous trends.

In considering initial wall spacing variation only, differences in the computed solutions are greatest in the logarithmic and outer regions. This can be attributed to the fact that when the total node count is held constant, decreasing the initial node spacing serves also to decrease the number of nodes that are available for freestream resolution. A compromise must be made between resolution of mean flow and near wall effects. Grids utilized in the remainder of the calculations contained herein use an initial wall spacing of 1.0×10^{-5} m, providing for both accurate near-wall modeling and mean flow resolution.

4.4 Final Grid Generation

The preceding grid study was used to guide the final grid generation task for this project. All of the grids begin with a channel flow section, basically two parallel flat plates, beginning at either FS 0.0 (FPG1, APG1) or FS 44.0 (FPG2, APG2). The streamwise node spacing in these sections is uniform and given by Δx_1 in Table 4.2. Aft of this section is a 4.0 cm region where the streamwise spacing is compressed from Δx_1 to Δx_3 using Vinokur's weighting factor. Δx_3 is the uniform streamwise node spacing used in the test sections, which begin at FS 64.0 and extend to FS 73.0. As was mentioned in Section 4.2, node spacing in the curved wall test sections is significantly tighter than that used in the upstream region. For grids FPG1 and APG1, the streamwise spacing in the

Table 4.2 Grid Dimensions - Test Case Grids

Reference	Size $\xi \times \eta$	Δy_{wall} [m]	Δx_1 [m]	Δx_3 [m]
FPG1	219 x 151	1.5×10^{-5}	0.4068×10^{-2}	0.1644×10^{-2}
FPG2	151 x 151	1.5×10^{-5}	0.2963×10^{-2}	0.1239×10^{-2}
APG1	219 x 151	1.5×10^{-5}	0.4068×10^{-2}	0.1642×10^{-2}
APG2	151 x 151	1.5×10^{-5}	0.2963×10^{-2}	0.1237×10^{-2}
FLAT1	151 x 101	0.4×10^{-5}	0.99×10^{-2}	N/A

test sections is equivalent to utilizing approximately 278 evenly spaced nodes on the GS series of grids. For the FPG2 and APG2 grids, this number climbs to approximately 370 evenly spaced nodes. This node distribution scheme enables increased resolution of the curved wall sections without adversely impacting computational expense. The compressed region, including the test sections, of Grids FPG1, FPG2, APG1, and APG2 are depicted in Figures G.19, G.20, G.21, and G.22, respectively.

4.5 Flat Plate Validation

Prior to comparisons with the experimental data taken at AFIT, validation runs using the Baldwin-Lomax and $k - \omega$ turbulence models were performed against Morrison's (18) flat-plate test case using the following conditions

$$M_\infty : 2.0$$

$$T_\infty : 222K$$

$$T_{wall} : 222K$$

$$R_e/m : 1.0 \times 10^7$$

These computations were performed on grid FLAT1, which utilized node clustering at the North and South domain boundaries and even spacing in the streamwise direction. This nodal distribution was chosen to correspond approximately to that used in the test section calculations. Results of these runs may be seen in Figures 4.1 and 4.2. Figure 4.1 is a

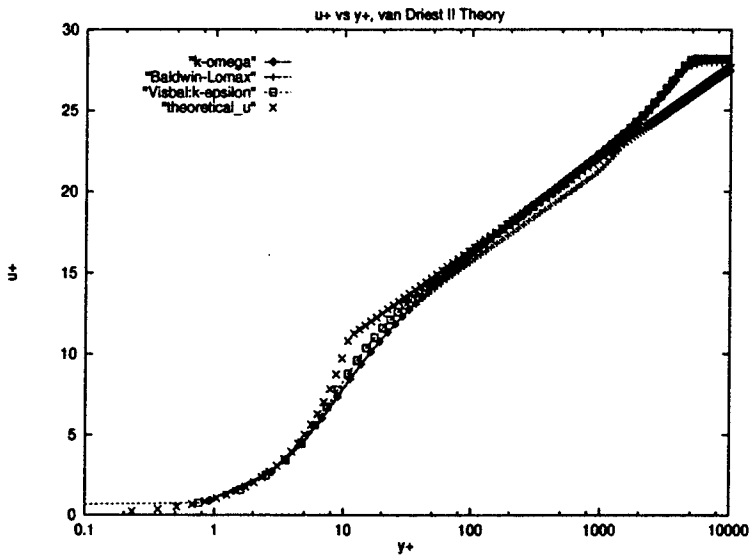


Figure 4.1 y^+ vs u^+ (van Driest)

plot of u^+ vs y^+ , where u^+ is once again based on the effective velocity as defined by van Driest (25). The correlated curve shown follows the rule

$$u^+ = \begin{cases} y^+ & : 0 \leq y^+ \leq y_{\text{match}}^+ \\ \frac{\ln y^+}{.41} + 4.9 & : y^+ > y_{\text{match}}^+ \end{cases} \quad (4.3)$$

as given in Morrison (18). Also shown in this plot is the output from a previously validated finite-difference code (19) which utilizes Roe flux difference splitting and a $k - \epsilon$ two equation turbulence model. Agreement between the present calculations, the $k - \epsilon$ code, and the correlated curve is very close through the inner region. In the overlap region, both the $k - \omega$ and Baldwin-Lomax models predict slightly lower velocities than the $k - \epsilon$ calculation. Note that the correlated curve has not been modified to account for the overlap region between the inner and logarithmic regions. Both of the two equation models do exceptionally well in the logarithmic layer, where both the magnitude and slope of the correlated curve is replicated computationally. In this region, the Baldwin-Lomax model accurately predicts the slope of the correlated data, but the magnitude is slightly lower than expected. Finally, agreement between all three models is excellent in the wake region.

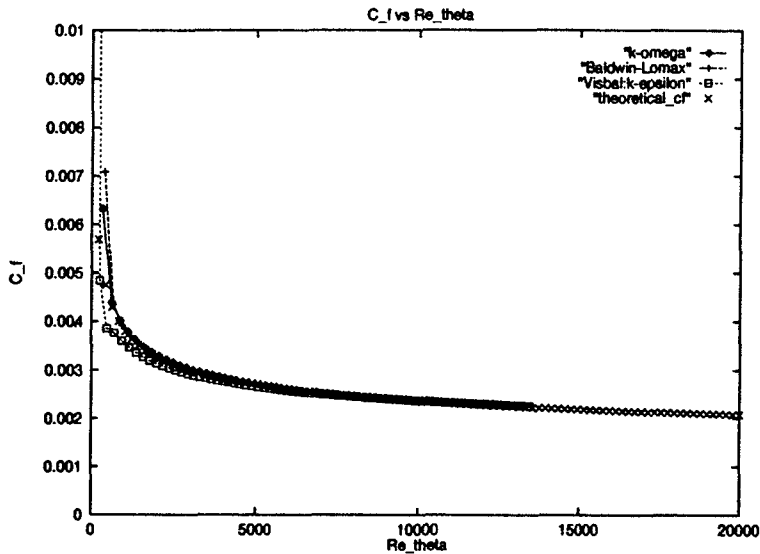


Figure 4.2 C_f vs Re_θ

Figure 4.2 is a plot of C_f vs Re_θ , where θ is the momentum thickness and is defined (25) as

$$\theta = \int_0^\infty \frac{\bar{\rho}}{\rho} \frac{\bar{u}}{U_e} \left(1 - \frac{\bar{u}}{U_e} \right) dy \quad (4.4)$$

A correlated curve from Hopkins and Inouye (11) is presented along with the computational results to serve as a basis for comparison. All three models accurately predict the skin friction for $Re_\theta \geq 7500$. At lower values of Re_θ , the $k - \epsilon$ model slightly under-predicts the skin friction whereas the $k - \omega$ and Baldwin-Lomax results continue to agree exceptionally well with the correlated values.

4.6 Upstream Boundary Conditions

In accordance with the recommendations of Settles and Dodson (20), upstream boundary conditions are set using experimentally determined values. Calculations performed in this investigation utilize two sets of boundary conditions, both based on the FS 44.0 data of Luker (15). The method by which these conditions were set is presented in this section.

4.6.1 Freestream Inflow. This boundary condition is used exclusively with grids FPG1 and APG1. It assumes that an undisturbed freestream ($\delta \equiv 0$) flow impinges on the leading edge of these grids at FS 0.0. The freestream value of u is set to the edge velocity measured by Luker (15) at Flow Station (FS) 44.0 and v is assumed to be everywhere zero. The total temperature ($T_0 = 294$ K) and pressure ($p_0 = 2.12634 \times 10^5$ Pa) are assumed constant, allowing direct computation of the static temperature and pressure at this flow station. The second of these assumptions ($p_0 = \text{constant}$) is used with the realization that it is technically inaccurate due to the presence of weak shocks in the wind tunnel caused by test section misalignment.

$$u_e = u_\infty = 605.1 \text{ m/s} \quad (4.5)$$

$$T = T_0 - \frac{u^2}{2c_p} = 111.8 \text{ K} \quad (4.6)$$

$$p = p_0 \left(\frac{T}{T_0} \right)^{\frac{\gamma}{\gamma-1}} = 7210 \text{ Pa} \quad (4.7)$$

The viscosity and density are calculated using Sutherland's Law 3.10 and the Equation of State 3.8, respectively. The constants utilized in the above formulations are

$$\begin{aligned} R &= 287.0 & \frac{\text{J}}{\text{kgK}} \\ c_p &= 1005.0 & \frac{\text{J}}{\text{kgK}} \\ \gamma &= 1.40 \\ C_1 &= 1.458 \times 10^{-5} & \frac{\text{N.s}}{\text{m}^2} \\ C_2 &= 110.4 & \text{K} \end{aligned}$$

Boundary conditions on k and ω are specified using Equations 3.60 and 3.61, respectively, using the thermophysical conditions calculated above.

4.6.2 Experimental Profile Inflow. This boundary condition set is used exclusively with grids FPG2 and APG2, approximating the flowfield conditions measured by Luker (15) at FS 44.0. The experimental velocity profile (with the additional specification

that $v = 0$) is used with the assumption of constant T_0 to approximate the temperature distribution through the boundary layer. The static pressure is assumed to be constant and equal to the value calculated at the mid-plane using the methodology introduced above. From these values, the density distribution through the boundary layer is established.

Boundary conditions on k are specified from fluctuating velocity information provided in the experimental data set, where the contribution of w' is assumed to be equal to v' , reducing Equation 1.2 to

$$k = \frac{1}{2} (u'^2 + 2v'^2) \quad (4.8)$$

The velocity profile is differentiated to obtain $\frac{\partial u}{\partial y}$, which is combined with the experimentally determined turbulent shear stress profile to specify an effective μ_T distribution. Rearranging Equation 3.51, k and μ_T are used to generate the ω profile at this station. The k and ω profiles thus generated may be found in Figures 4.3(a) and 4.3(b), respectively.

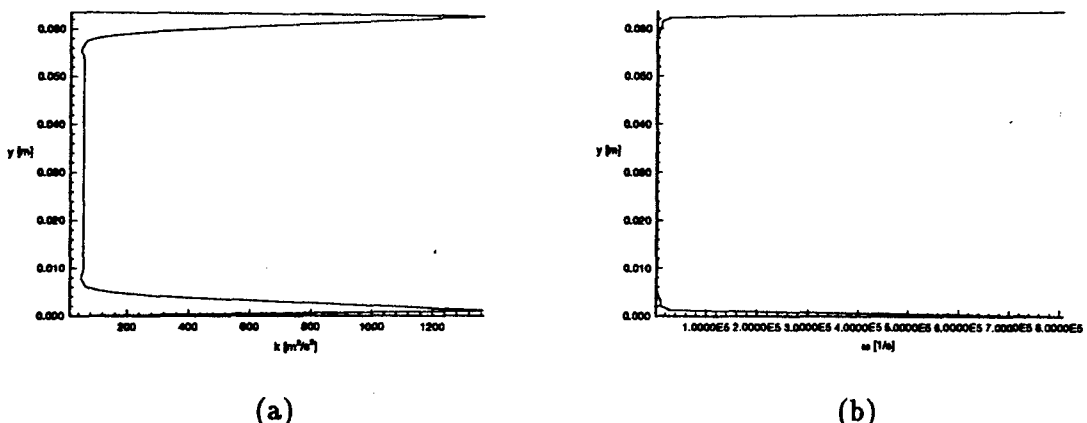


Figure 4.3 k and ω Experimental Inflow Profiles

V. Results and Discussion

This chapter presents the results of the present computational effort, beginning with a validation of the computed results through a comparison with the experimental data of Miller (16), Dotter (5), Luker (15) and Hale (9). Comparisons are made in the Zero Pressure Gradient (ZPG), Favorable Pressure Gradient (FPG), and Adverse Pressure Gradient (APG) test sections. Through this analysis, the effects of pressure gradient are addressed. Also discussed are differences between the Baldwin-Lomax and $k - \omega$ solutions, relative computational expense for both models, and the effect of upstream boundary condition specification on the downstream solutions.

5.1 Validation

This section presents the results of computations performed using the $k - \omega$ turbulence model. Computations utilize grids FPG2 and APG2, and in accordance with the recommendations of Settles and Dodson (20), the experimental profile inflow conditions are used unless otherwise specified. Overall agreement with experimental data is found to be excellent.

5.1.1 ZPG Test Section. The inflow plane for grids FPG2 and APG2 is at Flow Station (FS) 44.0; as such, direct comparison to the experimental data collected at FS 44.0 is meaningless. In the figures that follow, computed results at FS 60.0, upstream of the APG/FPG test sections, is compared to experimental data collected at FS 44.0 (Miller (16) and Dotter (5)) and FS 71.5 (ZPG data from Luker (15) and Hale (9)). This comparison assumes that the boundary layer at all three stations is fully developed and therefore velocity and shear stress profiles at these stations should be similar when plotted against y/δ .

Figure 5.1 is a comparison between the present computed Mach number profile at FS 60.0 and Miller's (16) experimental data, collected at FS 44.0. The Mach number is based on the magnitude of the velocity vector and the local static temperature

$$M \equiv \frac{\sqrt{u^2 + v^2}}{\sqrt{\gamma RT}} \quad (5.1)$$

Agreement between the computational and experimental profiles is very good, with a slight (magnitude is less than 1.1%) mismatch in the freestream that may potentially be related to either a mismatch in experimental testing conditions or the physical separation between the experimental and computational flow stations used to generate the plot. With regard to the former, recall that the upstream boundary conditions for this calculation are set using Luker's (15) FS 44.0 data. Using this inflow information, the freestream Reynolds number per meter is approximately 1.75×10^7 , whereas Miller (16) reported a freestream Reynolds number per meter of 1.50×10^7 for his measurements.

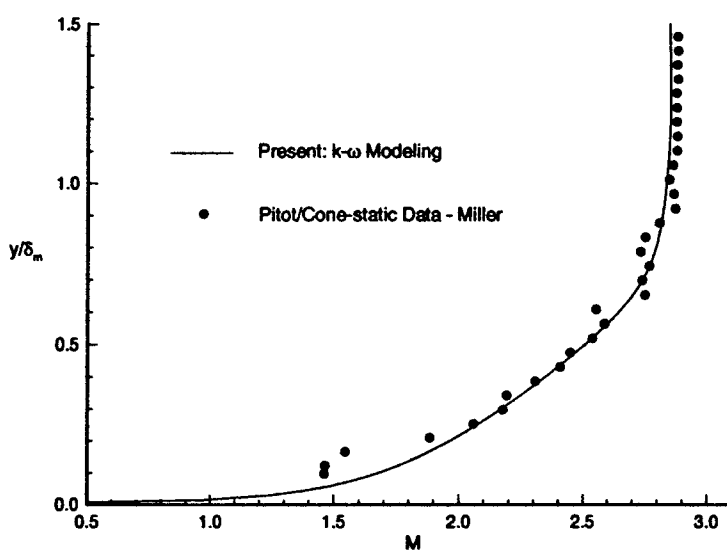


Figure 5.1 Mach Number vs y/δ_M , ZPG, FS 60.0/44.0

Figure 5.2 is a plot of the nondimensional turbulent shear stress (see Equation 4.2) versus y/δ_M . Shown in this plot are the present computed results and the "incompressible" component of the Reynolds stress tensor (see Appendix E) as reported by Miller (16) for the flow stations indicated. Agreement here is quite good, with the character of the experimental data being accurately reproduced computationally. Vertical shifting of the data

may be attributed to the methodology used to determine the boundary layer thickness, δ_M . The boundary layer thickness utilized in this figure and all those generated by Miller (16) and Dotter (5) is $\delta_{0.995M}$, or the value of y at which $M = 0.995M_e$. This process hinges on the accurate determination of the edge Mach number, an evaluation made extremely difficult by scatter in the experimental data. In retrospect, defining the boundary layer edge as $\delta_{0.99}$ would have significantly simplified this task by reducing the effect of the data scatter. With this in mind, computational agreement with the hot film data of Miller (16) at this flow station is considered excellent.

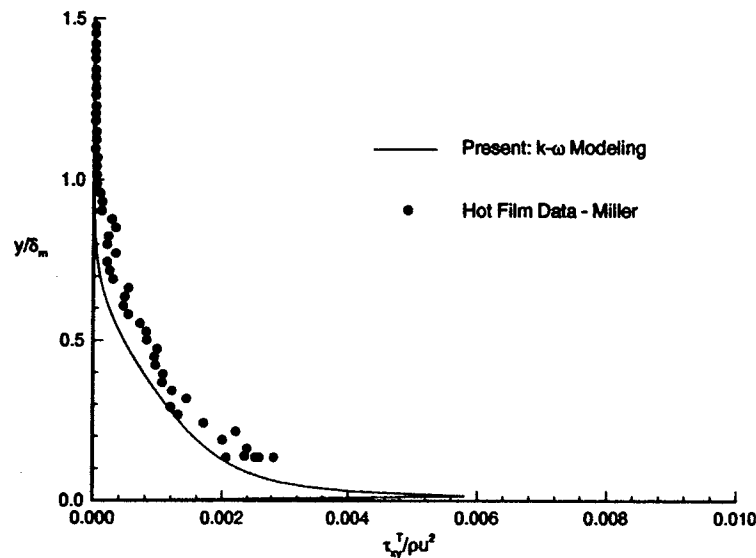


Figure 5.2 Nondimensional Turbulent Shear Stress vs y/δ_M , ZPG, FS 60.0/44.0

Figure 5.3 plots the nondimensionalized u component of velocity versus y/δ_u , where δ_u is the value of y at which $u = 0.995u_e$. This figure and all figures containing the Laser Doppler Velocimetry (LDV) data of Luker (15) and Hale (9) use this definition of the boundary layer thickness. Agreement between the present calculations and the LDV data is excellent. Both the magnitude and slope of the experimental data are replicated computationally. Similarly impressive results are presented in Figure 5.4, where the nondimensional turbulent shear stress is plotted versus y/δ_u . Once again, both the shape and magnitude of the experimental curve are captured in the computational results. Inspection

of Figure 5.5 reveals that the computed turbulent kinetic energy (k) profile closely matches the experimental data throughout the boundary layer.

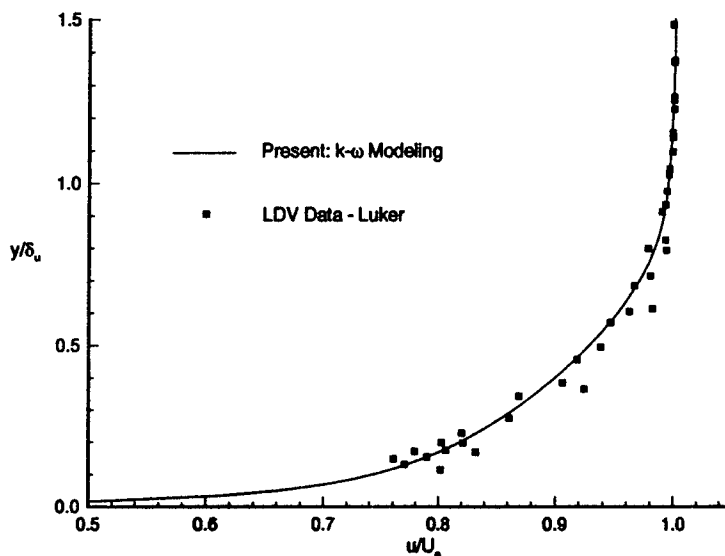


Figure 5.3 u/u_e vs y/δ_u , ZPG, FS 60.0/71.5

5.1.2 FPG Test Section. Profiles presented in this section are taken at FS 71.5 in the FPG test section. Figure 5.6 presents a comparison between the computed Mach number profile and Miller's (16) hot film data obtained at the same location. Agreement between the two curves is excellent within the boundary layer but once again a Mach number mismatch is evident in the freestream. In this case, the computed solution over-predicts the freestream Mach number at this flow station by less than 1.2%.

Comparisons between the computed and measured turbulent shear stress at this flow station (Figure 5.7) reveal a large mismatch between the numerically and experimentally generated curves. The character of the experimental data is captured in the computational curve, but the average difference in magnitude is greater than 50%, with the numerical results severely under-predicting the experimental data.

Comparison with the LDV data of Luker (15) at this flow station reveals similar, though not identical, results. The computed non-dimensional velocity profile shown in

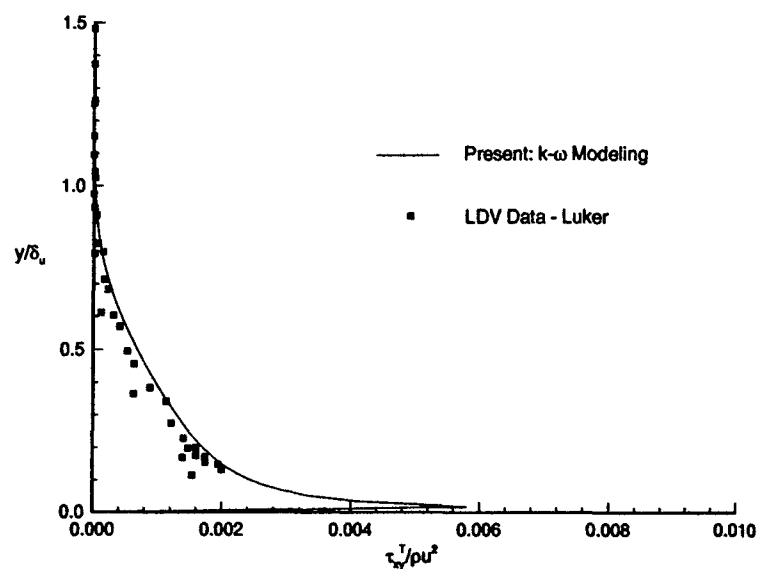


Figure 5.4 Nondimensional Turbulent Shear Stress vs y/δ_u , ZPG, FS 60.0/71.5

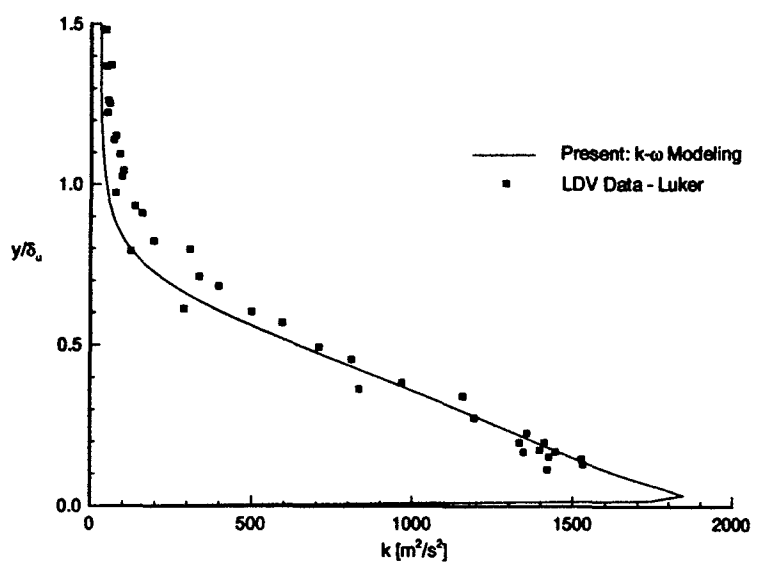


Figure 5.5 k vs y/δ_u , ZPG, FS 60.0/71.5

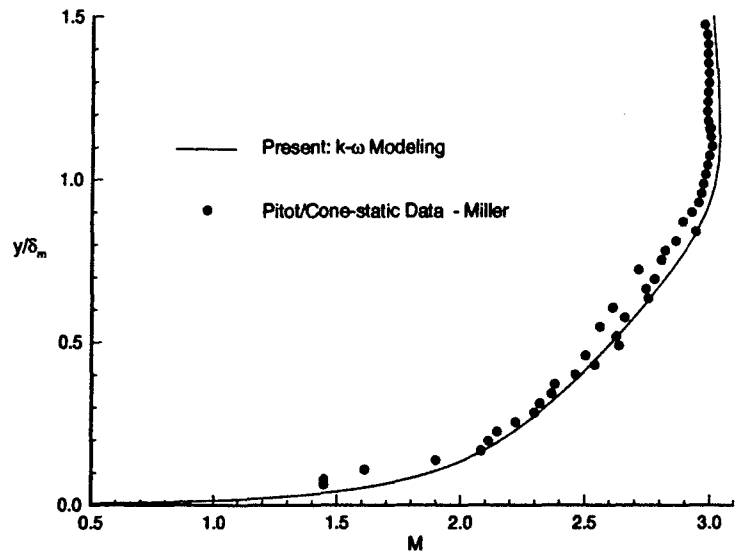


Figure 5.6 Mach Number vs y/δ_M , FPG, FS 71.5

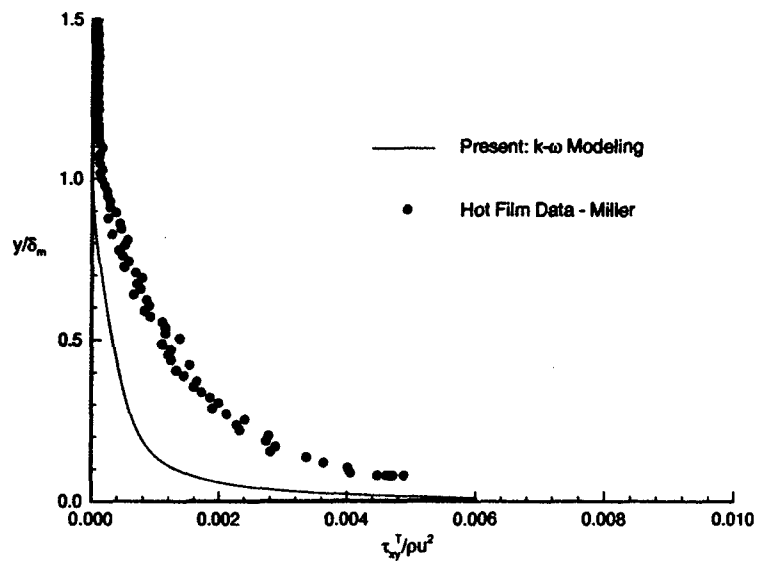


Figure 5.7 Nondimensional Turbulent Shear Stress vs y/δ_M , FPG, FS 71.5

Figure 5.8 tracks with the experimental data from the wall to the freestream, accurately predicting every aspect of the profile. Agreement with the experimentally generated nondimensional turbulent shear stress curve, however, is not as good. As shown in Figure 5.9, the computed curve over-predicts the experimental data by roughly 50% while maintaining the character of the experimentally generated profile. A comparison of Figures 5.9 and 5.7 reveals that large discrepancies exist between the data sets generated by Miller (16) and Luker (15). Luker (15) has suggested that this discrepancy may be due to the failure of the assumption that $p' = 0$, an assumption required in the hot-film data reduction technique. While this assumption is considered valid in zero pressure gradient regions, Luker (15) asserts that it may not be valid when a pressure gradient is present. The computational profile splits the difference between the hot-film and LDV measurements. Figure 5.10 compares the computed and experimental k profiles at this flow station. As was seen in the ZPG test section, agreement between the computational and experimental profiles is outstanding through the majority of the boundary layer. Differences near the wall may be attributed to the breakdown of an assumption made by Luker (15) and Hale (9) in the calculation of the experimental k data points in regions of FPG. An assumption regarding the magnitude of w' is required to calculate the turbulent kinetic energy because although the LDV setup did not allow for the measurement of velocity components in the transverse direction, fluctuations in this direction still contribute to k . The assumption made in the experimental analysis is that $w' = v'$.

5.1.3 APG Test Section. Profiles presented in this section were generated at FS 71.0 (Dotter (5)) and FS 68.0 (Hale (9)). As previously mentioned, FS 71.0 in the APG test section actually lies in a FPG region. This should not affect comparisons between the computational results and those presented by Dotter (5), although the profiles will not necessarily represent those characteristic of an APG flowfield.

Figure 5.11 is a plot of the local Mach number versus y/δ_M at FS 71.0. In this figure a sizeable mismatch is seen between the computed and calculated Mach number profiles. The profile itself is similar, but the magnitude of the computed curve is appreciably lower than that of the experimental data. The error appears almost as an “offset” type of error

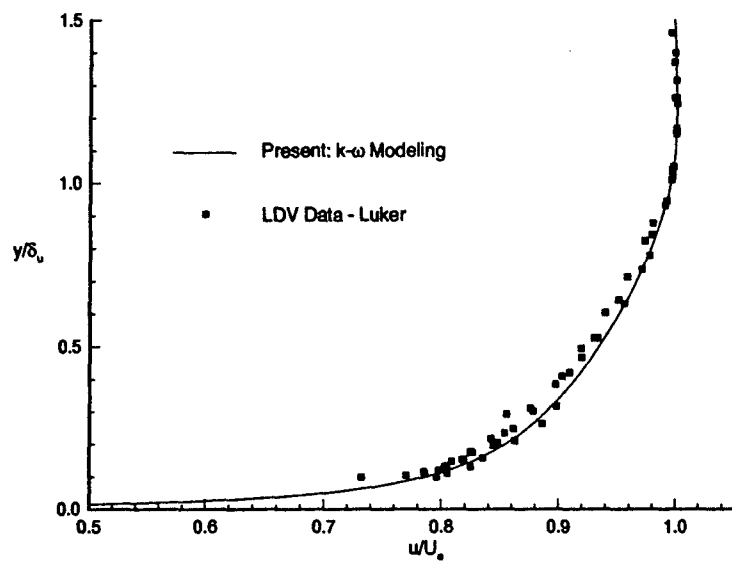


Figure 5.8 u/u_e vs y/δ_u , FPG, FS 71.5

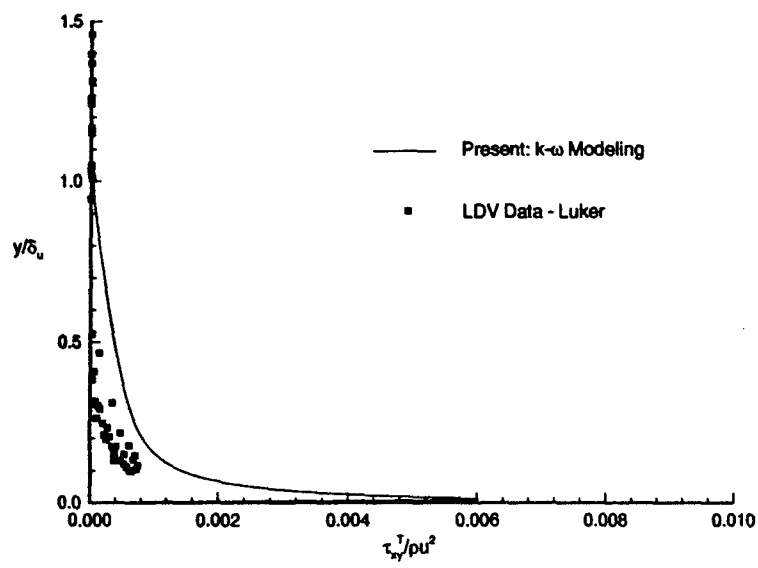


Figure 5.9 Nondimensional Turbulent Shear Stress vs y/δ_u , FPG, FS 71.5

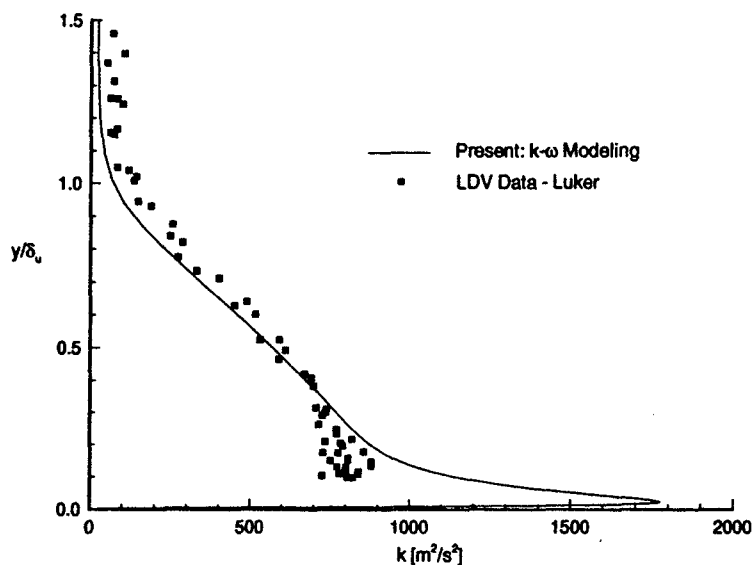


Figure 5.10 k vs y/δ_u , FPG, FS 71.5

and may be due to the upstream flowfield specification as mentioned previously. In the freestream, the magnitude of this error is 3.2%.

As may be seen in Figure 5.12, computed nondimensional turbulent shear stress profiles at this flow station are not in close agreement with the hot film data of Dotter (5), although some of the characteristics of the experimental data are present. The computational curve exhibits a linear region from $0.3 \leq y/\delta \leq 0.7$, the slope of which is only slightly greater than that of the linear portion of the hot film curve. Additionally, the experimental profile shows a sharp increase in turbulent shear as the wall is approached. This trend is also seen in the numerical results, the difference once again being that the magnitude of the computed curve is significantly less than that of its experimental counterpart.

Comparisons between the numerical curves and the LDV data of Hale (9) generated at FS 68.0 appear more promising. The nondimensional velocity profiles, shown in Figure 5.13, agree extremely well through the boundary layer. The computed turbulent shear stress curve (Figure 5.14) displays the same slope as the experimental data, but under-predicts the magnitude of the stress. The computational k profile is similarly under-

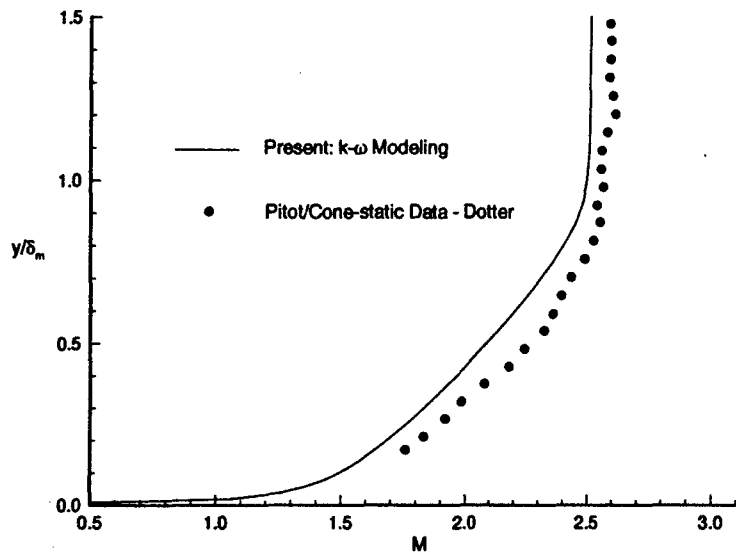


Figure 5.11 Mach Number vs y/δ_M , APG, FS 71.0

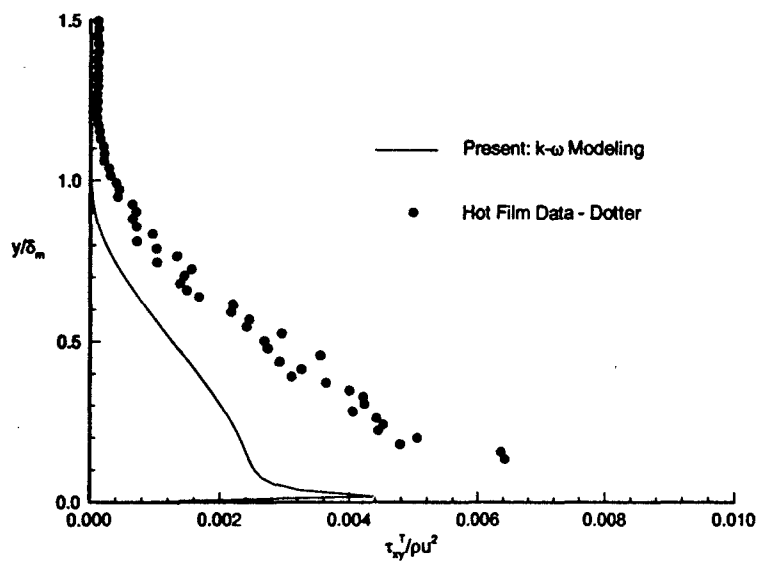


Figure 5.12 Nondimensional Turbulent Shear Stress vs y/δ_M , APG, FS 71.0

predicted, as may be seen in Figure 5.15, where the character of the experimental profile is replicated very well numerically; only the magnitude is mis-represented. As mentioned previously, the mismatch seen in these last two figures may be the result of difficulties in determining the boundary layer thickness, which is compounded at this flow station by the coalescence of pressure waves near $y = \delta$ (see Figure 5.47). This coalescence has the effect of smearing the edge of the boundary layer, making determination of the boundary layer thickness a difficult exercise. Altering the boundary layer thickness utilized in the generation of these curves will shift the profiles vertically, diminishing both the apparent accuracy displayed in Figure 5.13 and the discrepancies seen in Figures 5.14 and 5.15.

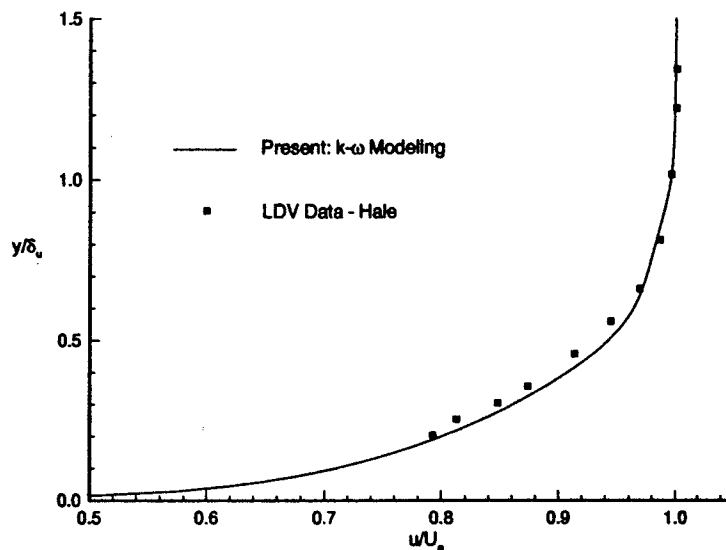


Figure 5.13 u/u_e vs y/δ_u , APG, FS 68.0

5.2 Comparison to Baldwin-Lomax Results

In order to further evaluate the effectiveness of the $k - \omega$ turbulence model and its present implementation, comparisons to numerical solutions obtained through the use of the Baldwin-Lomax turbulence model were conducted. This section presents a comparison between solutions obtained with these two models for the three test geometries, utilizing the LDV data of Luker (15) and Hale (9) as the basis for comparison.

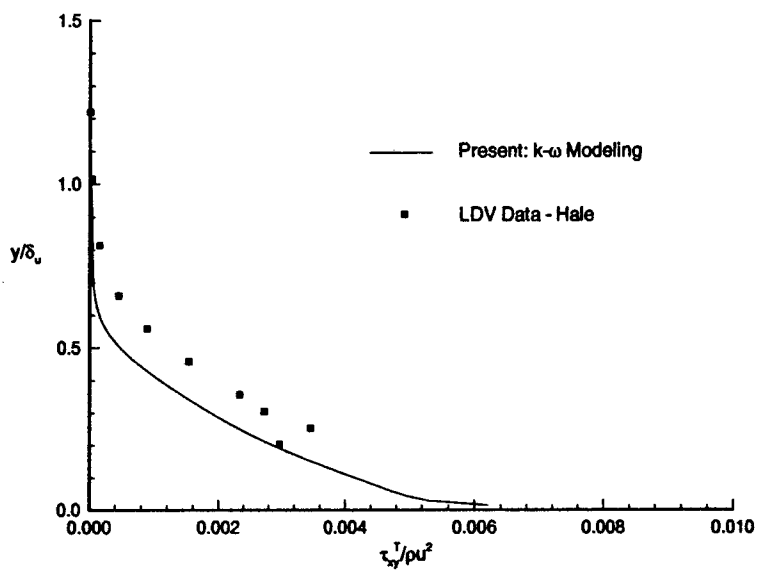


Figure 5.14 Nondimensional Turbulent Shear Stress vs y/δ_u , APG, FS 68.0

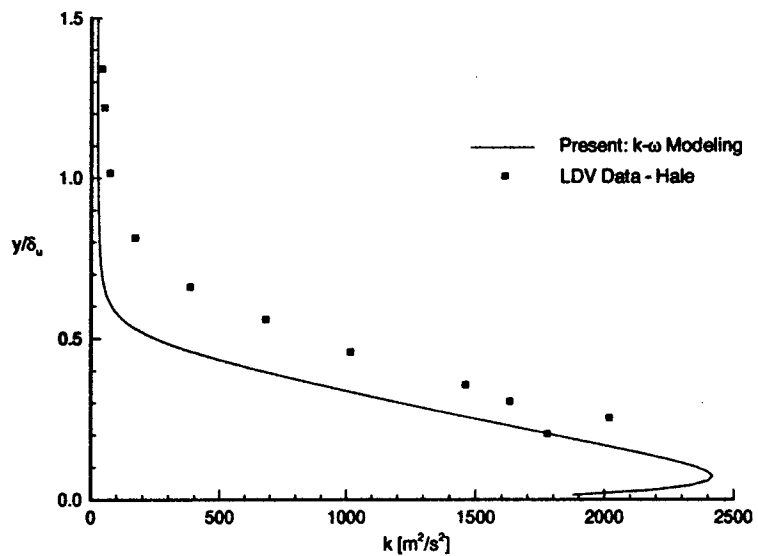


Figure 5.15 k vs y/δ_u , APG, FS 68.0

5.2.1 Zero Pressure Gradient (ZPG) Test Section. Figure 5.16 is a plot of the numerically and experimentally determined nondimensional velocity profiles at FS 60.0 (numerical data) and FS 71.5 (ZPG LDV data). As may be seen in this figure, agreement between the two numerical curves in the near-wall and wake regions is good. The profiles differ over a larger portion of the boundary layer, extending from $0.05 \leq y/\delta_u \leq 0.7$. Similar disagreement was observed in Section 4.5, where the Baldwin-Lomax model under-predicts the velocity in the logarithmic region of the wall law plot. Agreement between the Baldwin-Lomax and LDV velocity profiles at this flow station is therefore inferior to that observed with the $k - \omega$ solution.

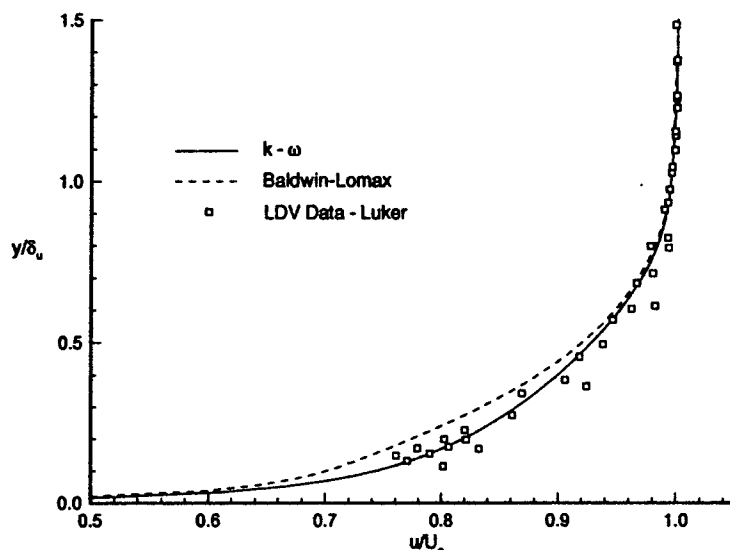


Figure 5.16 u/u_e vs y/δ_u , ZPG, FS 60.0/71.5

Turbulent shear stress profiles taken at this flow station (see Figure 5.17) reveal similar trends. The Baldwin-Lomax profiles agree well with the $k - \omega$ solution both near the wall and in the far field, but outside of these regions, the turbulent shear stress values predicted by the Baldwin-Lomax model are marginally higher than those of the $k - \omega$ model. Once again, the character of the experimental profile is better approximated by the profile generated through the use of the $k - \omega$ turbulence model.

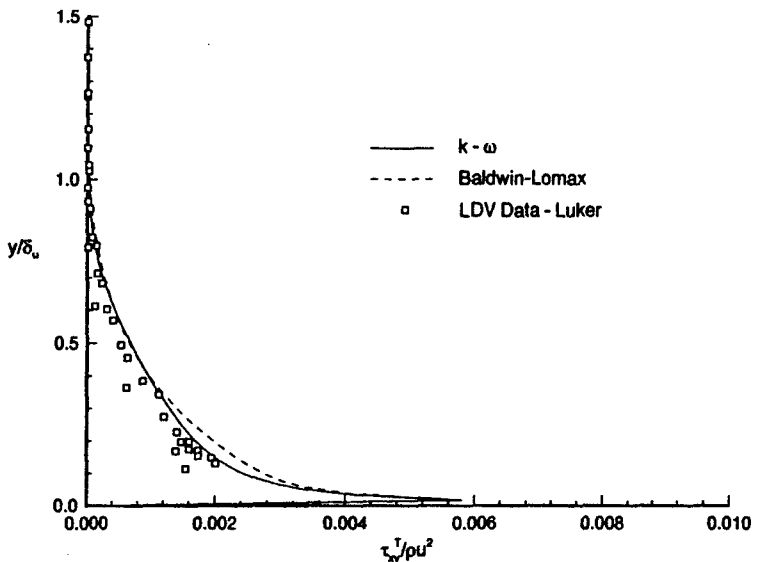


Figure 5.17 Nondimensional Turbulent Shear Stress vs y/δ_u , ZPG, FS 60.0/71.5

The disparity between the Baldwin-Lomax and $k-\omega$ profiles seen in the figures above must be linked to the computed eddy viscosity distribution, since this is the method by which the effects of turbulent fluctuations are incorporated into the mean flow equations. Figure 5.18 contains profiles of μ_T/μ vs y/δ_u for both the Baldwin-Lomax and $k-\omega$ computations, taken at FS 60.0. As may be seen in this figure, the profiles differ substantially in the region between $0.1 \leq y/\delta_u \leq 0.7$, where the Baldwin-Lomax model under-predicts the eddy viscosity by a large margin. This region is precisely that in which the nondimensional velocity profiles (see Figure 5.16) disagree. Disagreement between the turbulent shear stress profiles examined above is limited to the region given by $0.1 \leq y/\delta_u \leq 0.4$, but the largest offset (see Figure 5.17) occurs at approximately the same y/δ_u location as the largest offset in the eddy viscosity profiles.

Notice that the $k-\omega$ eddy viscosity profile presented in Figure 5.18 does not go to 0 in the freestream. This is the result of the "experimental profile" upstream boundary conditions, which specified a finite eddy viscosity in the freestream. Physically, this may be thought of as the result of finite freestream turbulence intensities. Because the $k-\omega$ turbulence model determines the eddy viscosity based on the state of the entire flowfield,

this upstream specification is reflected in the downstream profiles. As with all algebraic turbulence models, the Baldwin-Lomax model relies only on the local state of the flow to determine the eddy viscosity; the upstream boundary condition specification therefore has little or no effect on the downstream eddy viscosity distribution.

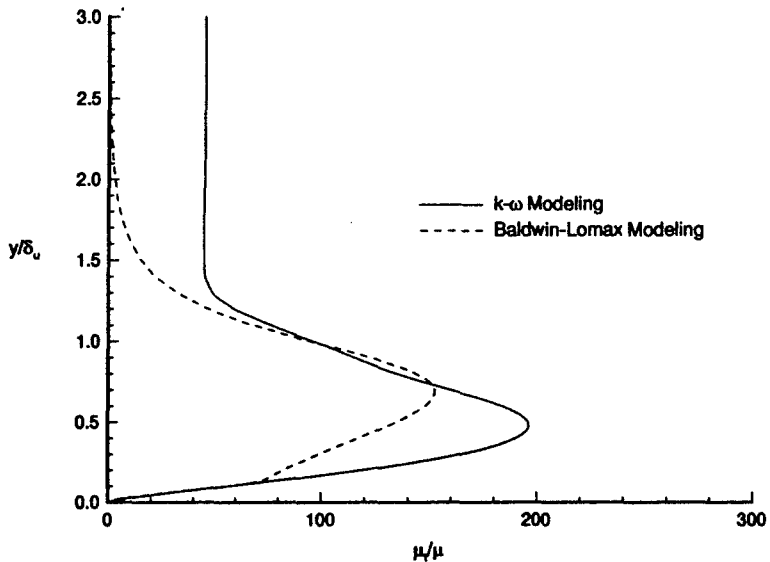


Figure 5.18 μ_T/μ vs y/δ_u , ZPG, FS 60.0/71.5

5.2.2 Favorable Pressure Gradient (FPG) Test Section. This section compares numerical profiles generated in the FPG test section at FS 71.5 with the LDV data of Luker (15) obtained at the same flow station. Figures 5.19 and 5.20 are plots of the nondimensional velocity and turbulent shear stress, respectively, at this location. These figures exhibit the same trends with regards to the Baldwin-Lomax solutions that were observed in the ZPG region, with under-predictions of the velocity and over-predictions in the turbulent shear stress appearing between $0.05 \leq y/\delta_u \leq 0.7$. As before, the $k - \omega$ turbulence model appears to more accurately represent the experimental data. Examination of the eddy viscosity profiles at this flow station (see Figure 5.21) reveals significant disparities throughout the boundary layer. While the peak eddy viscosity is similarly predicted by

both models, the Baldwin-Lomax model predicts that this peak occurs near the boundary layer edge, whereas the $k - \omega$ model predicts its location at $y/\delta_u \approx 0.6$.

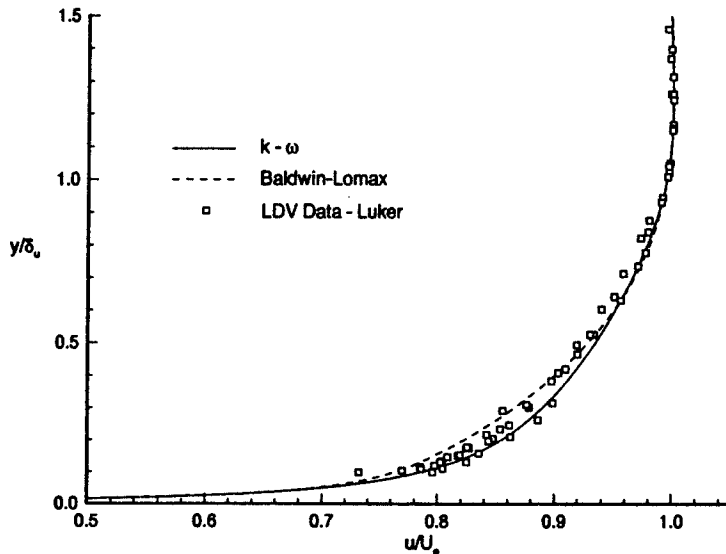


Figure 5.19 u/u_e vs y/δ_u , FPG, FS 71.5

5.2.3 Adverse Pressure Gradient (APG) Test Section. In this section, computed nondimensional velocity and turbulent shear stress profiles at FS 68.0 in the APG test section are compared; the LDV data of Hale (9) serves as the basis for comparison. In Figure 5.22, the Baldwin-Lomax solution is seen to deviate only slightly from the $k - \omega$ profile. Unfortunately, this profile deviation is such that the computed curve no longer matches the character of the experimental data. Similarly, in Figure 5.23 the overall magnitude of the turbulent shear stress is similar to that of the $k - \omega$ solution, but the character of the experimental curve is lost. Inspection of Figure 5.24 reveals good agreement between the computed eddy viscosity profiles in the inner and outer regions of the boundary layer, but a significant under-prediction of this quantity between $0.05 \leq y/\delta_u \leq 0.6$. This is seen as the root of the large disparities in the velocity and turbulent shear stress profiles mentioned previously.

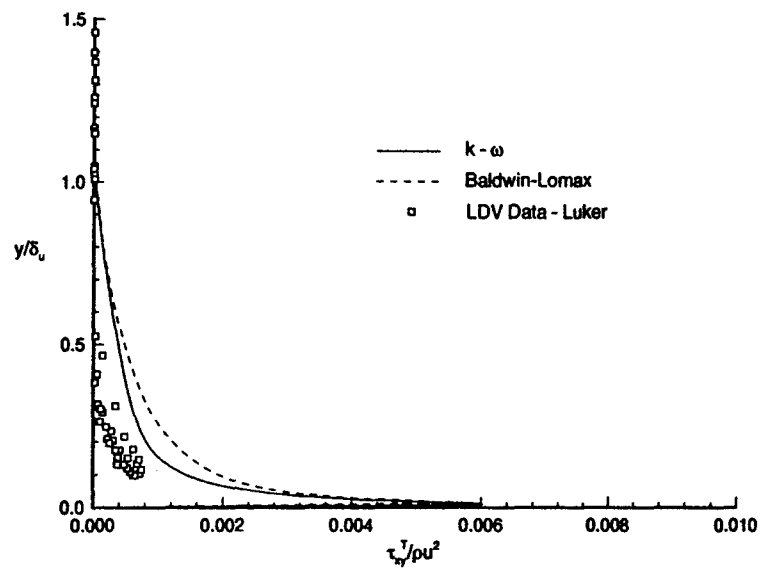


Figure 5.20 Nondimensional Turbulent Shear Stress vs y/δ_u , FPG, FS 71.5

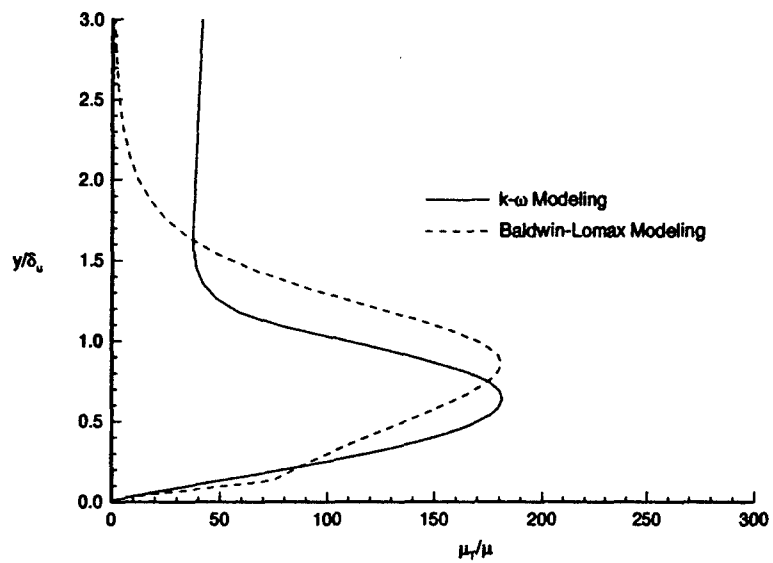


Figure 5.21 μ_T/μ vs y , FPG, FS 71.5

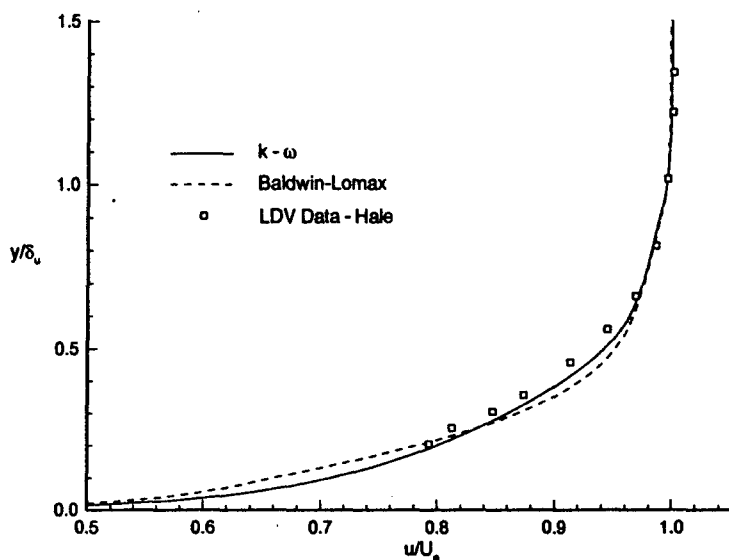


Figure 5.22 u/u_e vs y/δ_u , APG, FS 68.0

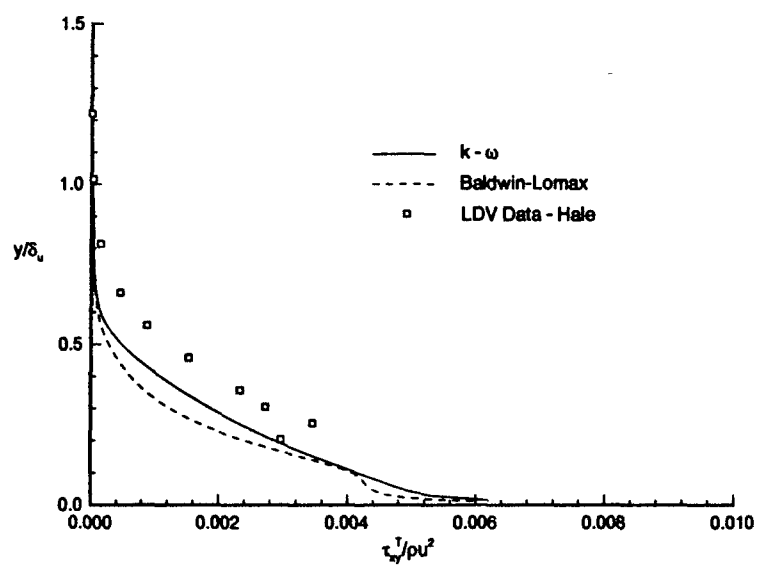


Figure 5.23 Nondimensional Turbulent Shear Stress vs y/δ_u , APG, FS 68.0

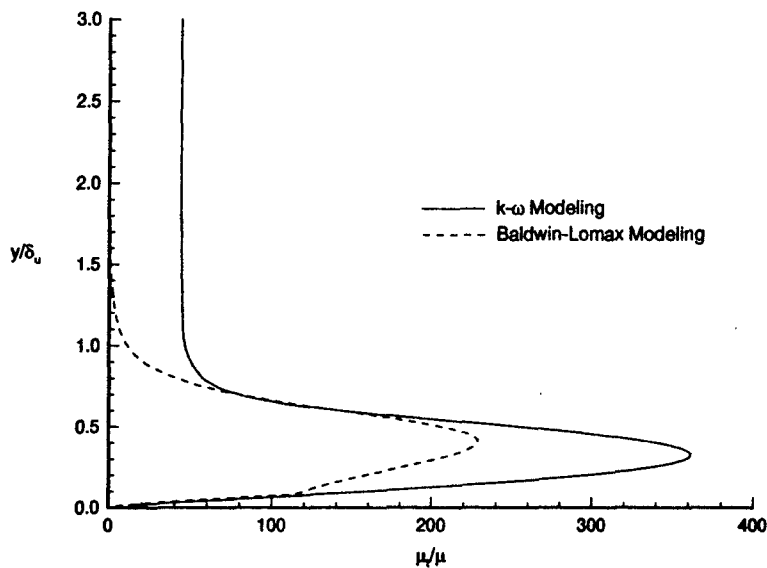


Figure 5.24 μ_T/μ vs y , APG, FS 68.0

5.2.4 Surface Effects. Figure 5.25 displays the distribution of the wall shear stress along the test sections for the Baldwin-Lomax and $k - \omega$ computations. Neglecting the entrance region, the Baldwin-Lomax turbulence model predicts wall shear values in the ZPG region that are 8% to 13% less than those predicted using the $k - \omega$ turbulence model. Using the correlation from van Driest II theory (24) (1), Luker (15) calculated the wall shear stress at FS 71.5 in the ZPG test section as 67.0 Pa. Extrapolating the slope of the τ_{wall} vs x curve from upstream of the test sections to 71.5 cm shows that the computed τ_{wall} at this station would be approximately 66.8 Pa, a difference of 0.3% from the experimental value. A similar extrapolation performed on the Baldwin-Lomax curve yields a wall shear stress of 64 Pa. Interestingly, the Baldwin-Lomax results indicate that $\frac{\partial \tau_{wall}}{\partial x} > 0$, a trend that predicted by neither the $k - \omega$ results nor theory. Predictions of wall shear in the FPG test section are similar in both slope and magnitude, whereas the Baldwin-Lomax computations in the APG test section under-predict the wall shear by a large margin when compared to the $k - \omega$ solution.

Figure 5.26 contains plots of the computed surface pressure as a function of location. The pressure distribution predicted through the use of the Baldwin-Lomax model is very

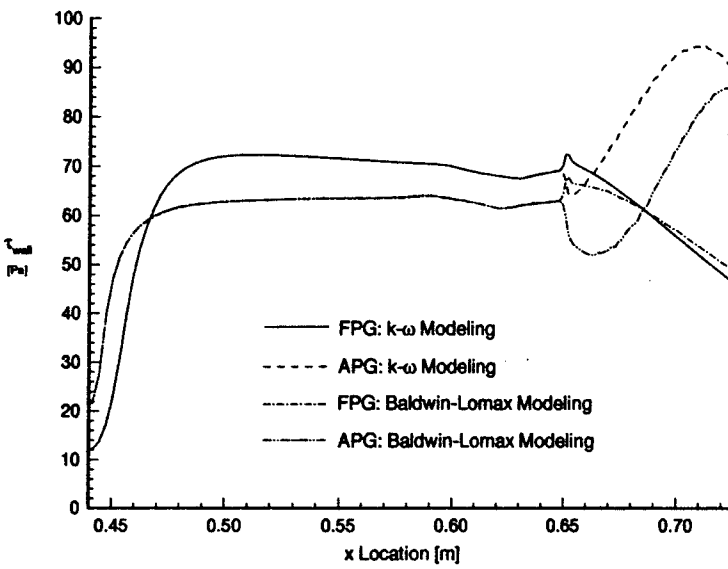


Figure 5.25 τ_{wall} vs x

similar to that obtained using the $k - \omega$ model over the majority of the tunnel surface for both experimental test sections. This agreement breaks down somewhat in the region between FS 58.0 and FS 65.0. In this region, a decrease in surface pressure is predicted by both models, the artifact of a series of pressure waves that are present in the computational domain as the result of the boundary conditions applied at the inflow station. The magnitude and duration of this pressure fluctuation is larger with the $k - \omega$ model than with the Baldwin-Lomax model. In the APG and FPG test sections, however, p_{wall} and $\frac{\partial p_{wall}}{\partial x}$ are seen to be effectively independent of the turbulence model utilized.

5.2.5 Computational Expense and Convergence Characteristics. Although the solutions obtained with the Baldwin-Lomax turbulence model are in general found to be less accurate than that obtained through use of the $k - \omega$ turbulence model, use of the former for flowfield analysis may be justified if a significant savings in computational time may be realized by doing so. A comparison of required Central Processing Unit (CPU) time for a fixed number of iterations using the two turbulence models has been performed. For this comparison, the code was run for 10,000 iterations on grid APG2, a 151x151 grid

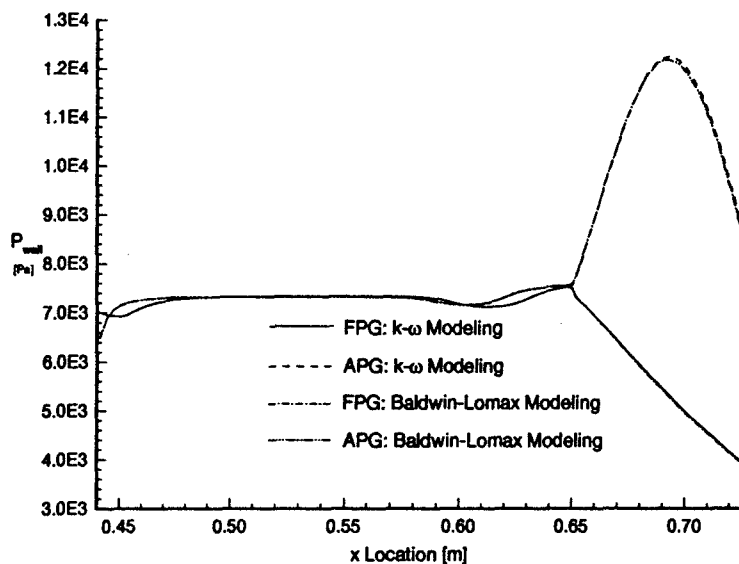


Figure 5.26 p_{wall} vs x

having 22801 cell centers on a Cray Research C916. In order to minimize the effect of read and write time requirements, no data output subroutines were called during these computations. The $k - \omega$ computations required 3012.529 seconds of CPU time for a total of 1.3212×10^{-5} seconds per iteration per cell center. The Baldwin-Lomax computations required 2811.601 seconds, or 1.2331×10^{-5} seconds per iteration per cell center, a 6.67% reduction in CPU usage over the $k - \omega$ model.

The convergence histories of computations utilizing the Baldwin-Lomax model are significantly different than those exhibited when $k - \omega$ modeling is used. Figure 5.27 shows characteristic convergence histories for Baldwin-Lomax and $k - \omega$ computations performed on Grid FPG2. The CFL number used for these calculations was 0.5. The convergence history typical of the $k - \omega$ turbulence model displays an initial increase in the residual, followed by a long steady decrease of roughly 12 orders of magnitude before bottoming out near 2.5×10^{-11} . Convergence to this level is seldom required, however, since the solutions effectively cease to evolve after the residual drops four or five orders of magnitude. The convergence history characteristic of the Baldwin-Lomax turbulence model shows a much smaller initial jump in the residual followed by a shallow decrease

of roughly 4 orders of magnitude. At this point oscillations in the solution preclude any further reduction in the residual unless the turbulence model is frozen, as shown in this figure. These oscillations are not eliminated by a reduction in the CFL number and are thought to be linked to the specification of y_{max} and F_{max} within the Baldwin-Lomax subroutine (see Section 3.3.1). As y_{max} bounces between two adjacent nodes, the flowfield is continually attempting to adjust to the new formulation for μ_T at that plane within the flow. This behavior may be at least partially eliminated by the introduction of finer computational meshes, but the intent of this section is to evaluate the performance of the models on the same mesh for the same flowfield conditions. For the purposes of this investigation, Baldwin-Lomax computations are deemed converged when this oscillation continues for roughly 10000 iterations unchanged. Fortunately, this oscillatory behavior appears after the flowfield properties of interest ($\tau_{wall}, p_{wall}, u, \tau_{xy}^T$) have ceased to change. It should be noted that this oscillation, though typical of Baldwin-Lomax computations, did not appear in every such computation. Variations in freestream/upstream conditions had a profound effect on the convergence history of Baldwin-Lomax computations; in fact, several Baldwin-Lomax computations (using different flow conditions) converged to the same degree as the companion $k - \omega$ computations.

In summary, the Baldwin-Lomax turbulence model produces results for these flowfields that are found to be less accurate and more sensitive to the inflow conditions than those obtained through use of the $k - \omega$ turbulence model. This may be the result of the Baldwin-Lomax model's inability to account for flow history effects, an ability possessed by the $k - \omega$ model, as mentioned in Chapter I. As such, use of this model based on potential CPU time savings is not a viable option for flowfields of the type examined in this study. As an alternative, implicit solution of the $k - \omega$ equations has the potential to significantly reduce computational expense while maintaining the high level of accuracy of the $k - \omega$ formulation.

5.3 Evaluation of Inflow Boundary Condition Effects

The uniqueness of the solution of a system of differential equations is guaranteed by the form of the boundary conditions imposed on that system of equations. This mathe-

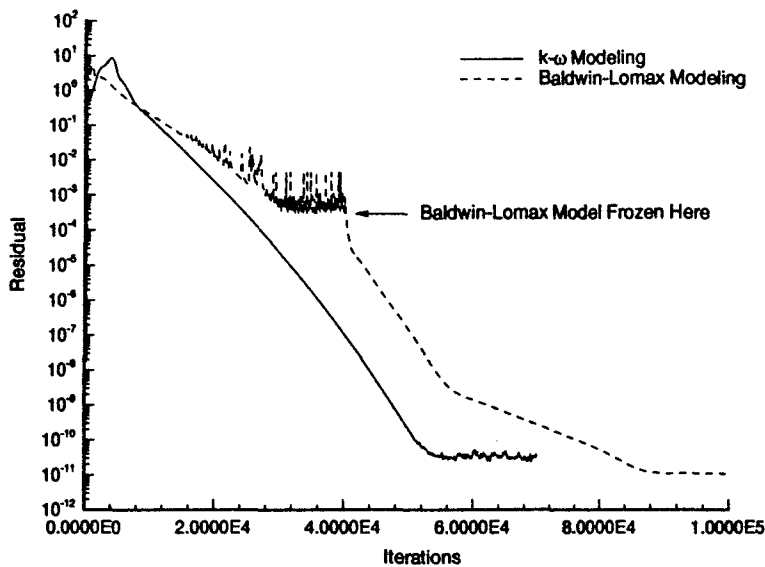


Figure 5.27 Convergence History, $k - \omega$ vs Baldwin-Lomax

mathematical reality drives the need to evaluate the effect of boundary condition variation on the solutions generated in this effort. Since the flowfield being studied is for the most part supersonic, the preferred direction of information propagation is largely in the streamwise direction. Thus, variations in the upstream boundary conditions may be expected to have a significant effect on the flowfield.

The two sets of boundary conditions used in this investigation are described in Section 4.6. The following sections compare and contrast the solutions obtained with each set of boundary conditions, once again using the LDV data of Luker (15) and Hale (9) as the basis for comparison.

5.3.1 Zero Pressure Gradient (ZPG) Test Section. This section compares the numerical solutions obtained at FS 60.0 with the LDV data extracted at FS 71.5 in the ZPG test section. Figure 5.28 is a plot of the nondimensional velocity as a function of y/δ through the boundary layer at this flow station. Although the numerically generated solutions agree closely in the wall region, this agreement disappears above $y/\delta \approx 0.2$. Examination of the freestream inflow curve reveals a velocity deficit in the upper two-

thirds of the boundary layer that is not seen in either the experimental profile inflow curve or the experimental data. This velocity deficit may be linked to an over-prediction of the turbulent shear stress in the same region, as is seen in Figure 5.29.

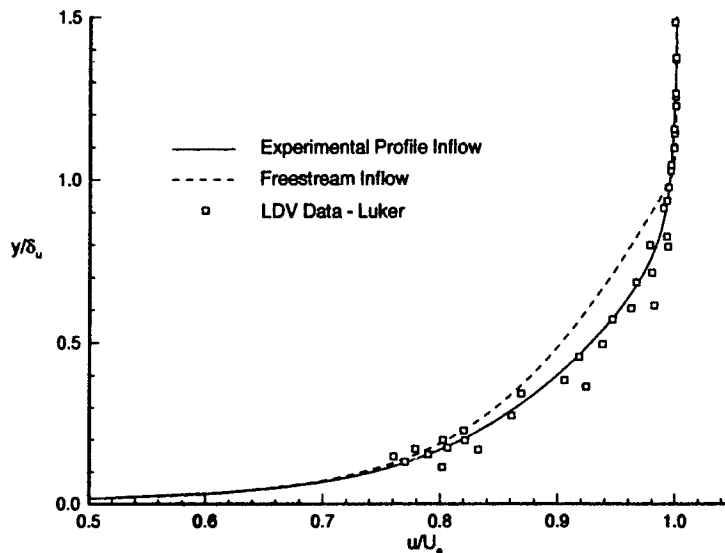


Figure 5.28 u/u_e vs y/δ_u , ZPG, FS 60.0/71.5

5.3.2 Favorable Pressure Gradient (FPG) Test Section. Profiles in this section were generated at FS 71.5 in the FPG test section. Figure 5.30 shows that the nondimensional computed velocity profiles differ only slightly at this flow station; both do an acceptable job approximating the experimental data. Similarly, Figure 5.31 shows close agreement between the computed solutions. Comparing the features of Figures 5.30 and 5.31 reveals that for a given y/δ location, high nondimensional velocity is typically coupled with reduced turbulent shear stress. Thus, an over-prediction of the local velocity appears to be linked to an under-prediction of the turbulent shear stress. This trend is also present in the ZPG test section, as may be seen in Figures 5.28 and 5.29.

5.3.3 Adverse Pressure Gradient (APG) Test Section. Profiles presented in this section were generated at FS 68.0 in the APG test section. Agreement between the numerical profiles is similar to that which was seen in the ZPG test section. The differences

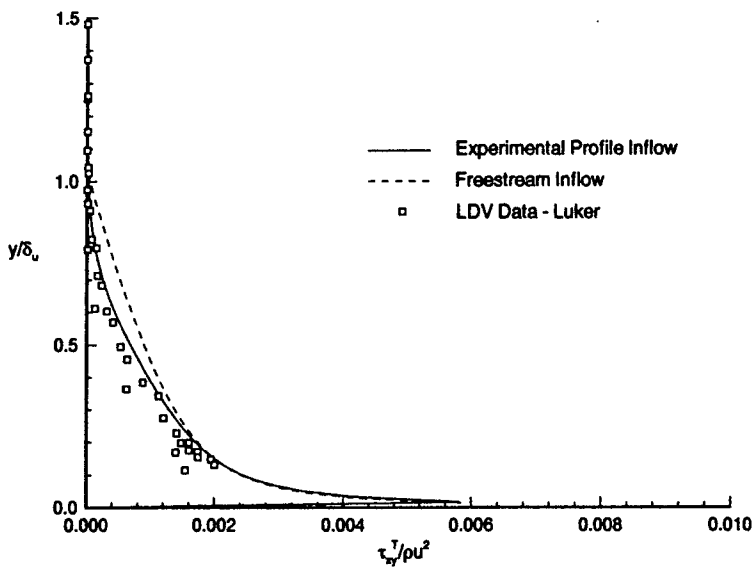


Figure 5.29 Nondimensional Turbulent Shear Stress vs y/δ_u , ZPG, FS 60.0/71.5

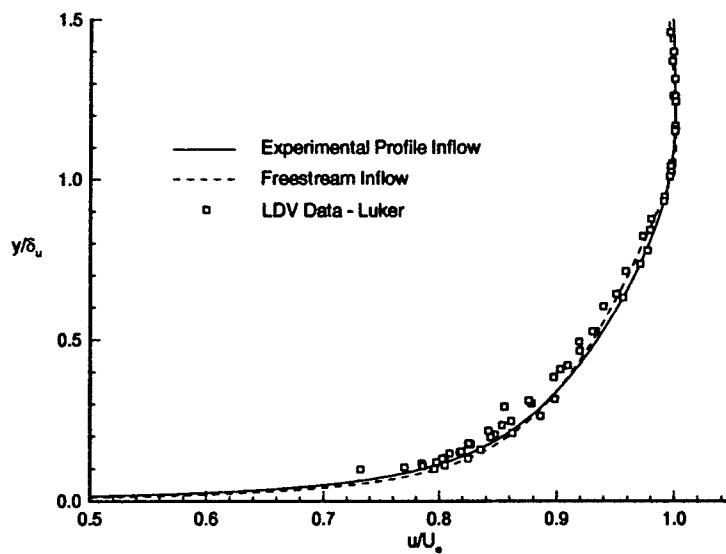


Figure 5.30 u/u_e vs y/δ_u , FPG, FS 71.5

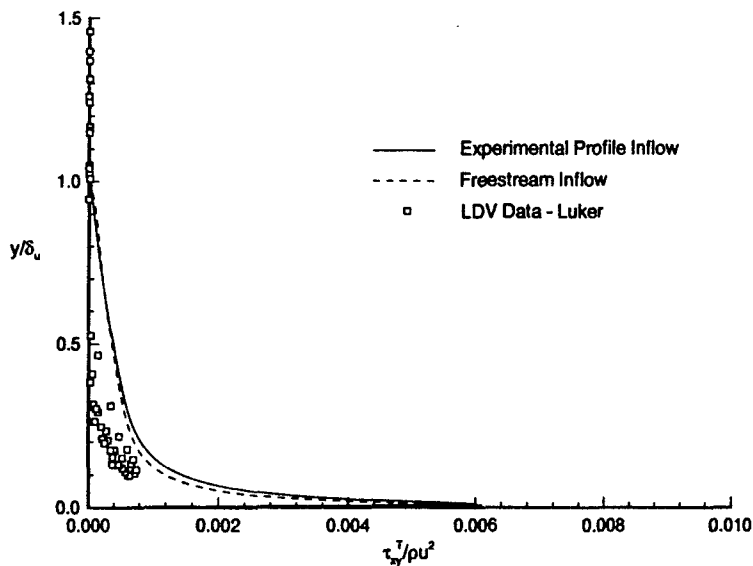


Figure 5.31 Nondimensional Turbulent Shear Stress vs y/δ_u , FPG, FS 71.5

may once again be characterized by a velocity deficit and accompanying turbulent shear stress surplus between $0.2 \leq y/\delta \leq 0.75$. The velocity profile is once again more accurately predicted numerically when the experimental profile boundary conditions are used. The turbulent shear stress profile generated through the use of the freestream inflow conditions, however, more accurately predicts the magnitude of this quantity over a fairly large region of the boundary layer. Unfortunately, this agreement is restricted to magnitude effects only; the general shape of the turbulent shear stress profile is still more accurately reproduced by the computations utilizing the experimental profile conditions. Finally, the converse of the trend observed in the above sections appears to hold as well; numerical under-prediction of the velocity is coupled with an over-prediction of the turbulent shear stress.

5.3.4 Surface Effects. The effect of the upstream boundary condition variation is not limited to the velocity and shear stress profiles. Differences exist in the surface pressure and wall shear stress distributions as well. Figure 5.34 shows that while the computed wall shear stress values are the same for both models in the upstream ZPG region, wall shear predictions in the pressure gradient regions differ. This figure indicates that the magnitude

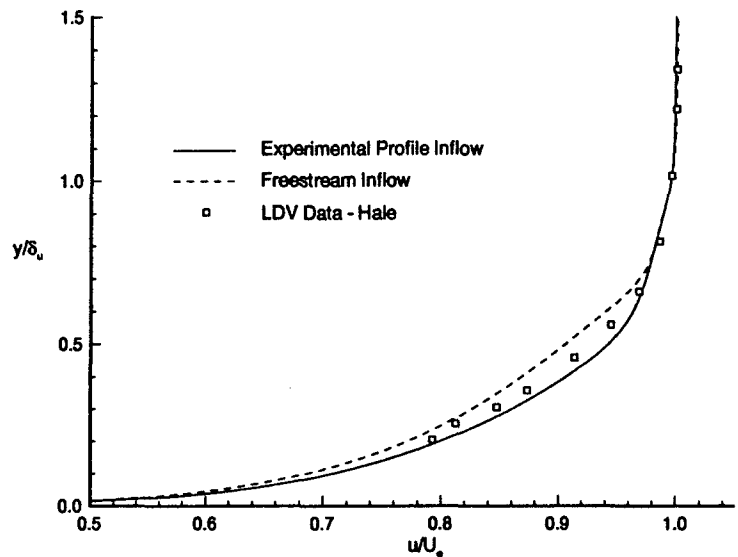


Figure 5.32 u/u_e vs y/δ_u , APG, FS 68.0

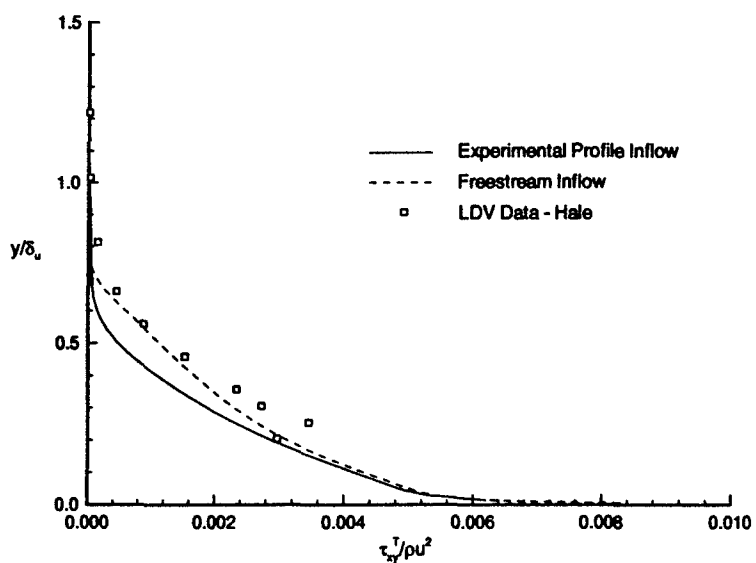


Figure 5.33 Nondimensional Turbulent Shear Stress vs y/δ_u , APG, FS 68.0

of the change in the wall shear stress in the pressure gradient regions is smaller with the freestream inflow conditions than that obtained through the use of the experimental profile inflow conditions.

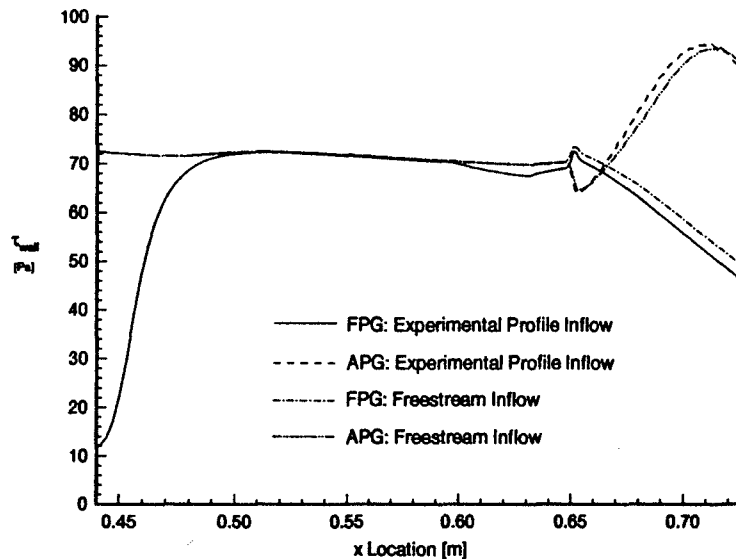


Figure 5.34 τ_{wall} vs x

Figure 5.35 shows that while the pressure gradient within the test sections is similarly predicted by both inflow boundary conditions, a fairly large discrepancy exists in the computed surface static pressure distributions. In this figure, computations using the freestream inflow conditions predict significantly higher static pressures than those utilizing the experimental inflow profile. Interestingly, it is the curve generated using the freestream inflow conditions that most closely approximates the experimental data (Luker (15), FPG data and Hale (9), APG data). Recall that both inflow conditions use essentially the same data, the difference being that the latter utilizes more flowfield information by specifying nonuniform velocity, temperature, density, k , and ω profiles. Thus, there is no reason to expect that the pressure distribution should vary when one set of boundary conditions is used in lieu of the other.

The differences observed may be partially explained through an examination of Figures 5.36 and 5.37. The lower frame of these figures contains a numerical contour plot of

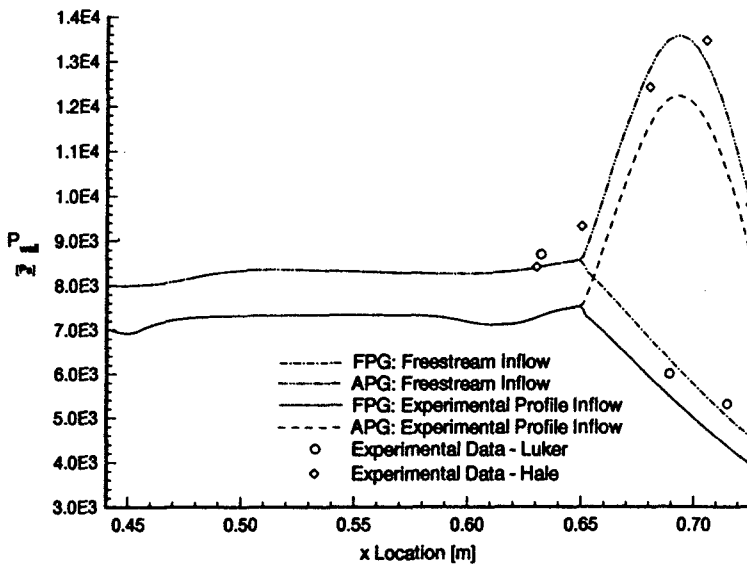


Figure 5.35 p_{wall} vs x

the static pressure in the test section; the upper frame is a line plot of the static pressure at the surface. Comparing these figures with Figure 5.35 reveals that while the pressure at the inflow plane is effectively the same for both sets of boundary conditions, a series of reflected pressure waves present in the numerical solution increases the surface (and mean flow) pressure substantially in the streamwise direction. These pressure waves appear to originate at the leading edge of the computational mesh when the previously undisturbed freestream is subjected to no-slip boundary conditions at the inlet. This is an interesting feature, but it does not explain the agreement between the freestream inflow case and the experimental data.

Looking to the experimental setup for potential answers, Schlieren images taken in the test sections reveal the presence of “seam shocks,” oblique shock waves which originate upstream of the measurement stations due to misalignment of the wind tunnel sections. The presence of these weak shock waves raises two issues: first, it challenges the assumption that the total pressure is constant from the settling chamber to FS 44.0, the location at which the upstream boundary conditions were measured. The effect of these seam shocks would be to reduce the total pressure at that station, leading to further reductions in the

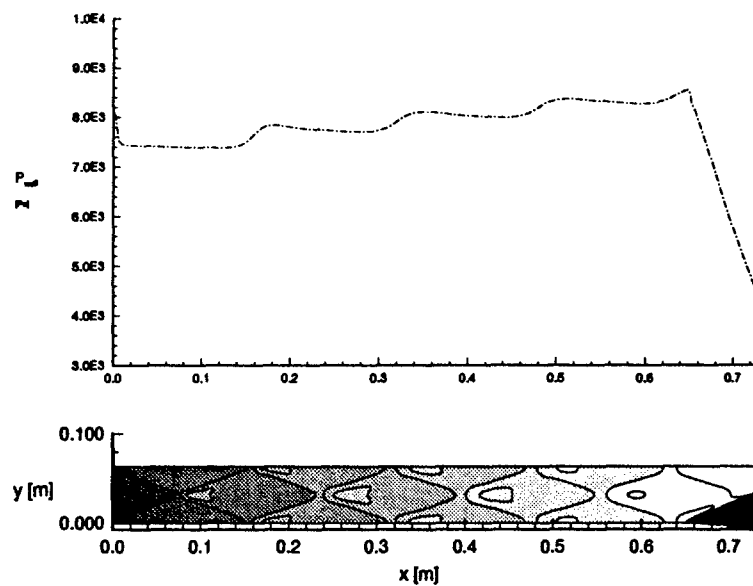


Figure 5.36 p_{wall} vs x and Pressure Contour Plot, FPG, Freestream Inflow

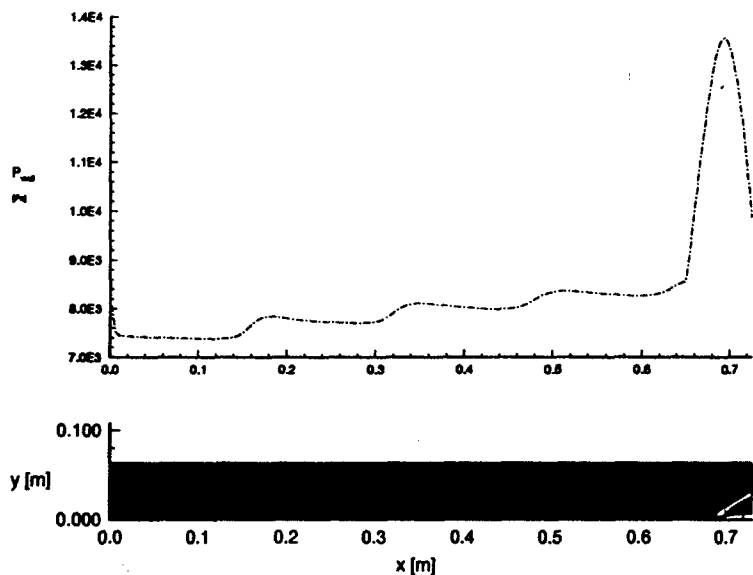


Figure 5.37 p_{wall} vs x and Pressure Contour Plot, APG, Freestream Inflow

static pressure. Thus, the static pressure assumed at FS 44.0 is the maximum possible static pressure at that flow station given the velocity profile and total pressure and temperature measured in the settling chamber. The second is that these shocks may be responsible for raising the static pressure from the "assumed" upstream value of roughly 7200 Pa to the 8400 Pa measurement obtained by Hale (9) at FS 63.0. In that case, the agreement between the freestream inflow calculation and the experimental data is fortuitous at best; the non-physical numerical pressure fluctuations simply combine in such a manner as to mimic the pressure rise in the actual flow due to these unintended, but physical, oblique shocks.

These reflected pressure waves are also present to some extent in Figures 5.38 and 5.39, which were generated through the use of the experimental profile inflow boundary conditions. The appearance of pressure fluctuations in these solutions tends to dispel the notion that the instantaneous application of no-slip at the leading edge is responsible for the computational pressure fluctuations. A potential link between these two calculations is that in both cases the v component of velocity is set to 0. For the freestream inflow case, this is a good approximation, consistent with the assumption of an undisturbed freestream. In the experimental profile case, however, this assumption is fairly inaccurate; boundary layer flows typically have non-zero v components of velocity. It is possible that this inconsistency is at least partially responsible for the appearance of the pressure waves in that calculation.

Finally, a portion of the observed pressure mismatch may be linked to the stagnation temperature and pressure utilized in the specification of both sets of boundary conditions (see Section 4.6. For example, a 1 degree difference in the total temperature specification leads to a 140 Pa offset in the static pressure. Similarly, uncertainty in the stagnation pressure measurements reported by Luker (15) lead to an 88 Pa window over which the static pressure may vary.

5.3.5 Summary. Specification of the upstream boundary condition appears to have a significant effect on the velocity and shear stress profiles in the ZPG and APG test sections. This effect is diminished appreciably in the FPG test section. Thus, the

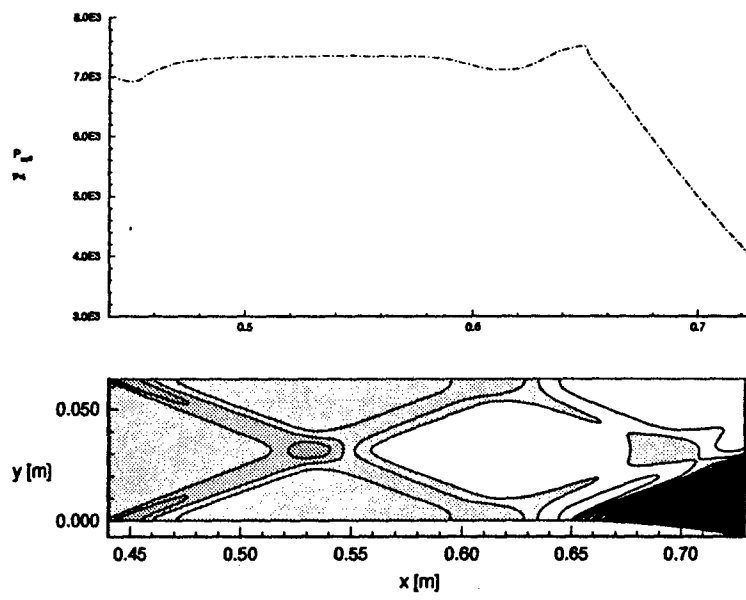


Figure 5.38 p_{wall} vs x and Pressure Contour Plot, FPG, Experimental Profile Inflow

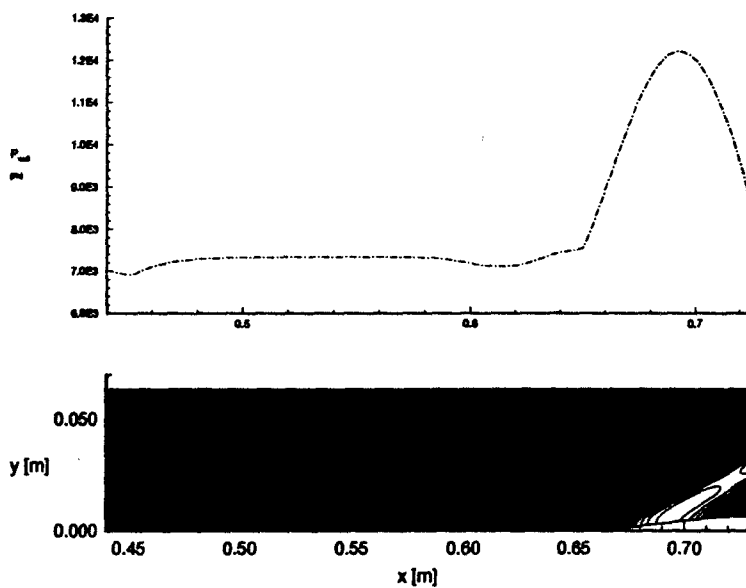


Figure 5.39 p_{wall} vs x and Pressure Contour Plot, APG, Experimental Profile Inflow

stabilizing effect of a FPG tends to reduce the effects of variations in upstream boundary condition specification, whereas the effect of an APG is to maintain, if not amplify, these differences. From a practical standpoint, this observation implies that extra care must be taken when specifying the upstream boundary conditions for a flowfield characterized by ZPG or an APG. The converse appears to hold as well for FPG flowfields. Finally, accurate specification of the upstream profile, to include thermophysical quantities and all components of the velocity vector, is required to obtain accurate absolute pressure distributions, although the magnitudes of pressure gradients are reproduced accurately regardless of the inflow condition used.

5.4 Flowfield Analysis

This section presents the results of a flowfield analysis performed using the experimental profile inflow conditions and the $k - \omega$ turbulence model, the combination of turbulence model and upstream boundary conditions found to provide the most accurate overall solutions. As in the previous sections, this section focuses on the effects of the favorable and adverse pressure gradients through an examination of the velocity, turbulent shear stress, and eddy viscosity profiles, the static pressure distribution along the surface, and the distribution of τ_{wall} through the test sections.

5.4.1 Favorable Pressure Gradient (FPG) Test Section. The flowfield in the FPG test section is characterized by a progressive and mild expansion beginning at FS 65.0 and continuing to the end of the computational domain. A numerical Schlieren image of this test section, showing density gradients in the y direction, $\frac{\partial \rho}{\partial y}$, is presented in Figure 5.40(a). In this figure, flow is from left to right and lightly shaded areas represent regions of positive density gradients; dark areas correspond to negative gradients. The expansion is visible as an incrementally brighter triangular region in the lower right hand corner of the figure. In this figure, the boundary layer at the lower surface is seen to respond immediately to the presence of this pressure gradient by increasing in thickness, while the boundary layer at the upper surface appears to be unaffected by the expansion. This observation is consistent with those of Spina, Smits & Robinson (21), who found that "...bulk dilatation

decreases the wall shear stress and increases the boundary-layer thickness." Referring back to Figure 5.38, the average pressure gradient at the lower surface in the expansion region is fairly constant and may be calculated as -4.5728×10^4 Pa/m.



(a)



(b) Luker (15)

Figure 5.40 Schlieren Imagery of FPG Test Section

Figure 5.40(b) is an actual Schlieren photograph of the FPG test section. Prominent in this figure are the "seam shocks" mentioned in Section 5.3.4. One appears as a light line passing through the frame from upper left to lower right, the other begins at the lower left, moving towards the upper right corner but dissipating away before it arrives there. This pattern is initially symmetric about the centerline of the tunnel. In this figure, a thickening of the boundary layer is evident as the flow passes into the expansion region, but the expansion is more difficult to visualize due to noise in the flow and the arrival of the first seam shock.

The remainder of this section will concentrate on profiles obtained at different flow stations within the FPG test section. The location of these stations and the orientation of the cutting planes (lines) with respect to the test section are shown in Figure 5.41, a composite figure based on a contour plot of the pressure gradient in the x direction, $\frac{\partial p}{\partial x}$. Superimposed over this contour plot are the planes along which data has been extracted; directly above the plot is a representation of the surface pressure distribution at the bottom wall in the test section. Immediately evident in this contour plot are the reflected pressure waves mentioned previously and a significantly more visible expansion region.

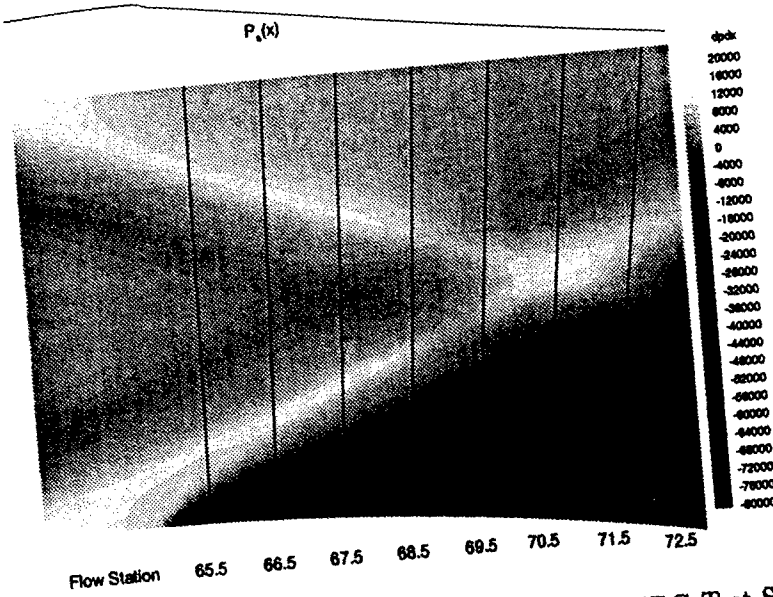


Figure 5.41 Location of Measurement Stations, FPG Test Section

Figure 5.42 presents velocity profiles obtained at the stations indicated in Figure 5.41. This figure clearly shows the evolution of the flow from one closely resembling a ZPG profile (FS 65.5), to the profile presented previously as one representative of a FPG flow. This evolution is characterized by a gradual increase in the edge velocity and boundary layer thickness as the traverse moves farther into the expansion region. Although it appears in this figure that the freestream velocity decreases at the downstream flow stations, this is a by-product of the body-normal coordinate system used in the generation of these profiles.

The nondimensional turbulent shear stress profile evolves in a similar manner, as may be seen in Figure 5.43. Once again, the profile at FS 65.5 closely resembles the ZPG profiles taken at FS 60.0 (see Figure 5.9). Progressing through the expansion region, the character of the profile changes, with the slope of the curve increasing, reducing the turbulent shear stress through a large portion of the boundary layer. While the peak value near the wall remains essentially unchanged, the area under the profile decreases significantly, potentially indicating a reduction in the total amount of energy present in the turbulent fluctuations.

Based on this supposition, Figure 5.44 presents the turbulent kinetic energy profiles at these same flow stations. The arrows in this figure indicate the direction of movement

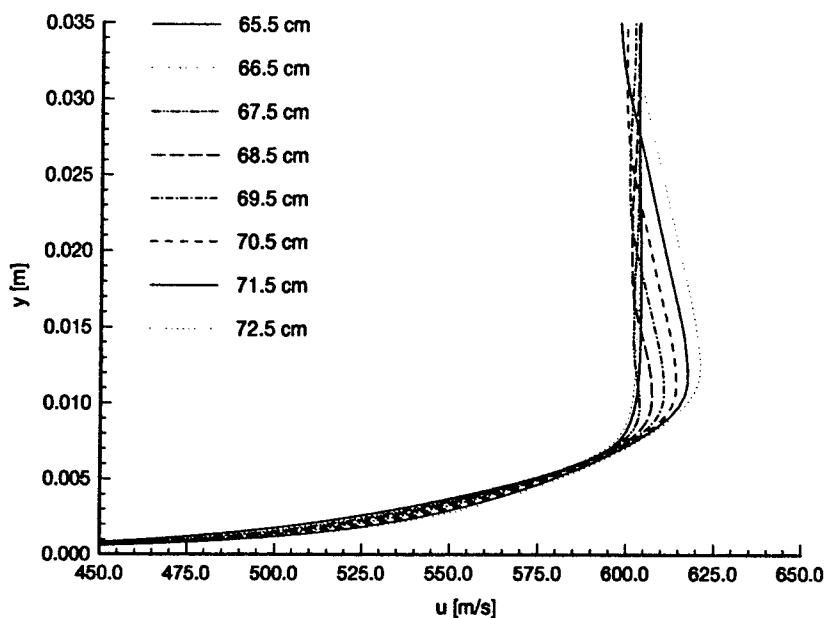


Figure 5.42 Velocity vs y , FPG Test Section

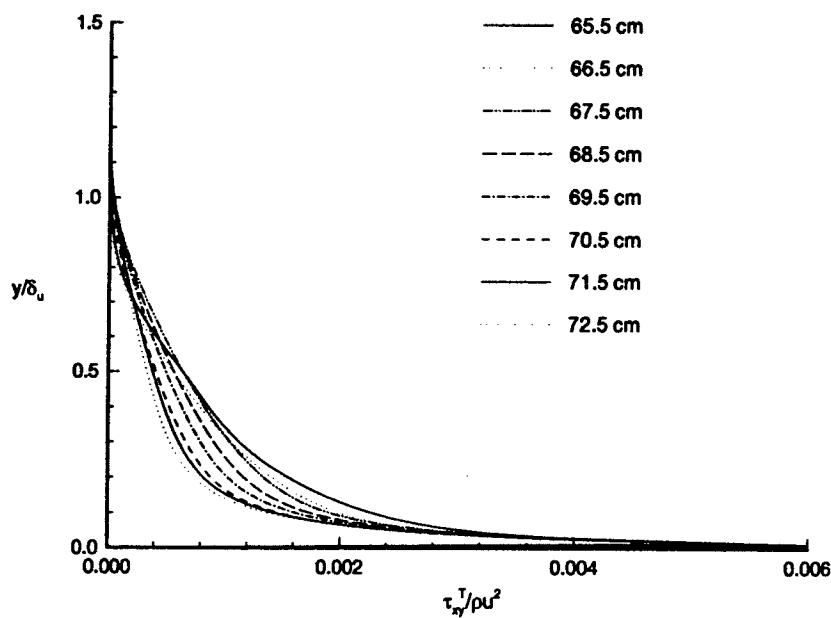


Figure 5.43 Nondimensional Turbulent Shear Stress vs y/δ_u , FPG Test Section

of the profiles as the cutting planes are moved downstream. This figure shows that while neither the peak turbulent kinetic energy (TKE) near the wall nor the area under the $k - y$ curve are significantly reduced, the distribution of TKE through the boundary layer is altered by the presence of the FPG. This alteration consists of a shift which increases the TKE near the edge of the boundary layer while reducing its magnitude close to the wall. A physical argument is proposed: High inertia freestream flow resists the influence of the curvature of the wall, increasing the boundary layer thickness. As a result of this increased boundary layer thickness, the velocity gradient near the wall decreases, resulting in decreased shear stress at the wall and decreased energy transfer to the wall through viscous effects. This reduction in the wall shear stress may be clearly seen in Figure 5.34, where the shear stress at the wall is reduced from 72 Pa to 46 Pa over the course of 8 cm. Since the total energy in the flow is conserved, the reduction in energy transfer to the wall must be balanced by an increase in the energy transfer elsewhere. This shifts the TKE curve toward the edge of the boundary layer, where increased transfer of TKE into the mean flow accounts for the reduction in energy transferred to the wall.

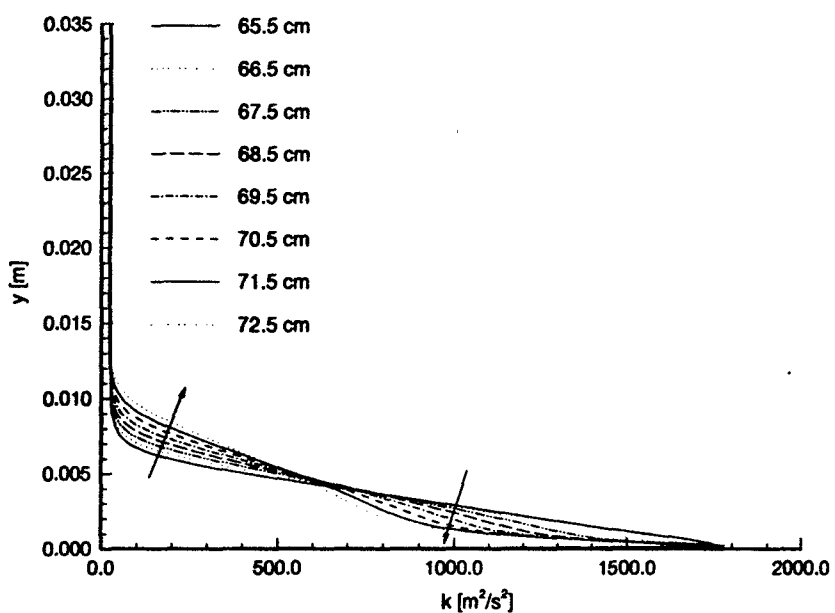


Figure 5.44 Turbulent Kinetic Energy vs y , FPG Test Section

Figure 5.45 shows the evolution of the eddy viscosity profiles through the FPG test section. The peak eddy viscosity is seen to decrease and move away from the wall as the cutting plane is moved downstream. This magnitude reduction and peak shift are thought to be responsible for the reduction in the turbulent shear stress seen in Figure 5.43 and the re-distribution of turbulent kinetic energy seen in Figure 5.44. Examination of the eddy viscosity levels in the freestream reveals that these values are also reduced under the influence of the FPG. As noted in Spina, Smits & Robinson (21), a FPG tends to decrease the magnitude of turbulent fluctuations in compressible boundary layer flow, even re-laminarizing these flowfields if the FPG is strong enough. Computationally, this result arises from a reduction in the eddy viscosity, a feature that is clearly predicted by the $k - \omega$ turbulence model.

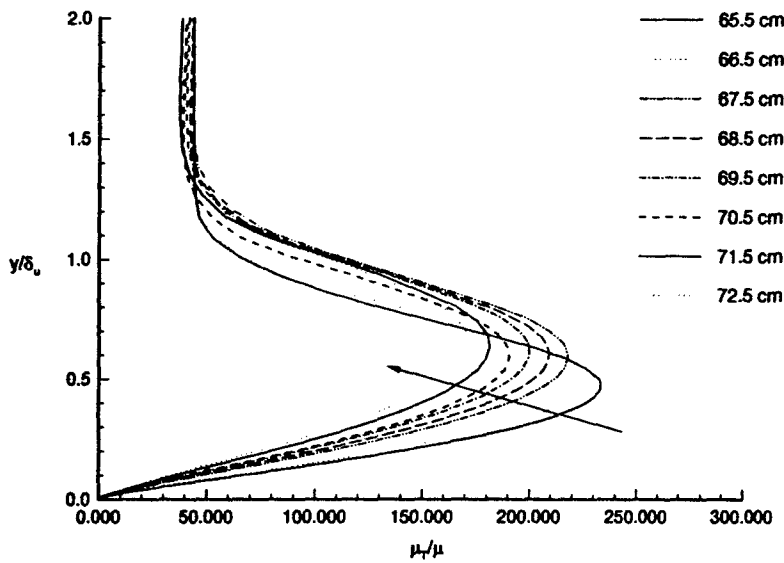
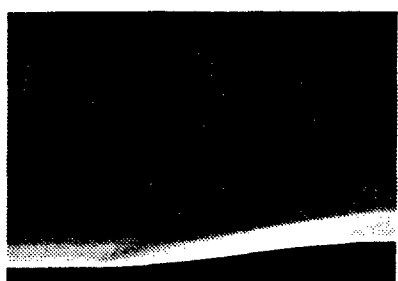


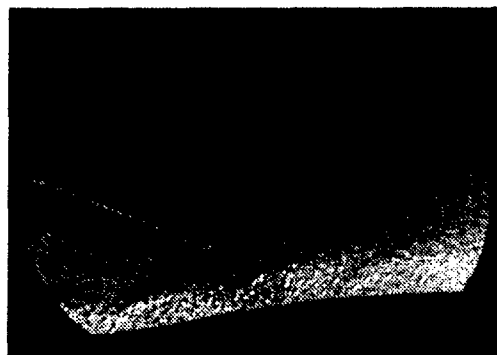
Figure 5.45 μ_r/μ vs y/δ_u , $k - \omega$ Modeling, FPG Test Section

5.4.2 Adverse Pressure Gradient (APG) Test Section. The flowfield in the APG Test Section displays a mixed set of features. As mentioned in Chapter II, regions of both favorable and adverse pressure gradient are present in this test section. In the region upstream of FS 68.0, (see Figure 5.39) the lower wall is concave up, creating a region

of adverse pressure gradient. The magnitude of the pressure gradient in this region is relatively constant and calculated to be 1.3425×10^5 Pa/m. Beyond FS 68.0, the radius of curvature increases until an inflection occurs, transitioning the pressure gradient from adverse to favorable. Hence, aft of FS 69.0 the pressure gradient is favorable; beyond FS 71.0 the magnitude of this gradient is fairly constant and equal to -1.6201×10^5 Pa/m



(a)



(b) Hale (9)

Figure 5.46 Schlieren Imagery of APG Test Section

Figure 5.46(a) is a numerical Schlieren image of this test section. Strong density gradients are evident in the shock wave, which strengthens near the end of the test section. The boundary layer is seen to decrease in thickness initially behind the coalescence of pressure waves near the wall, and then to increase in the region of FPG which follows. Figure 5.46(b) is an actual Schlieren image of this test section, displaying the same characteristics as the numerical prediction. Note that the “seam shocks” seen in Figure 5.40(b) are present in this image as well. The effect of these weak oblique waves is diminished in this test section, however, due to the strength of the main shock structure.

Figure 5.47 is a contour plot of the pressure gradient in the x direction, over which are superimposed the locations of the data planes considered in this section. From this figure, the development of the shock wave is readily visible, transitioning from a simple coalescence of pressure waves into a proper shock near the end of the test section. As was done previously, a representation of the surface static pressure in the test section is shown above this contour plot.

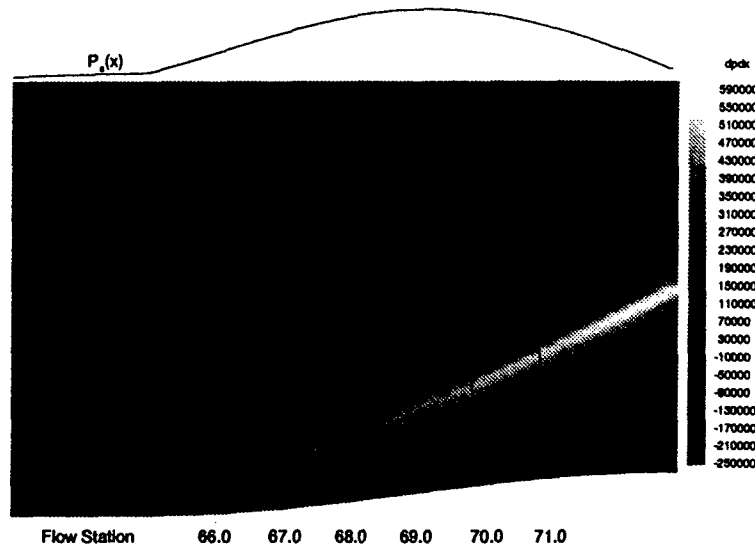


Figure 5.47 Location of Measurement Stations, APG Test Section

As may be expected and seen in Figure 5.48, the combination of the pressure gradients and the shock wave has a dramatic effect on the velocity profiles in the test section. Initially, the effect of the APG on the velocity profiles is to decrease the edge velocity and thin the boundary layer, as may be seen by comparing the profiles at FS 66.0 and 67.0. By FS 68.0, the shock is strong enough to have a smearing effect on the boundary layer edge, making that edge ill-defined. Aft of FS 68.0, the effect of the shock is restricted primarily to the flow outside the boundary layer. It is in this region (aft of FS 68.0) that the FPG begins to dominate the flowfield, manifesting its presence through an increase in the boundary layer thickness.

The nondimensional turbulent shear stress profiles in this section also reflect the varying character of the flowfield. The peak turbulent shear stress near the wall is seen to increase with streamwise position initially, maintaining a profile that resembles that seen in the ZPG regions. After the peak value is reached in the vicinity of FS 68.0, the profiles begin to change in character, moving towards the form presented in Figure 5.43. As was seen in this figure, progression along the FPG region is accompanied by a reduction in the turbulent shear stress in the flowfield. It is interesting to note that the profiles aft of FS 68.0 in this test section do not immediately take the form of those generated in the FPG

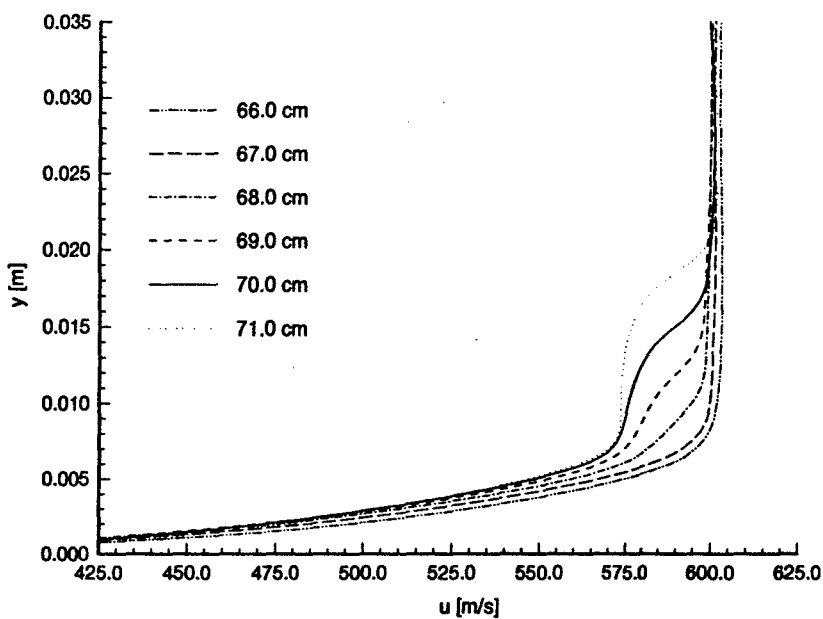


Figure 5.48 Velocity vs y , APG Test Section

test section. Their shape instead reflects both APG and FPG qualities. This observation serves to emphasize the importance of “historical” flowfield effects in turbulence modeling. This trend is also reflected in Figure 5.34, which indicates an initial increase in the wall shear stress, followed by a decrease in this quantity. Note that the peak wall shear occurs after the inflection takes place, once again indicating the importance of upstream effects.

The turbulent kinetic energy (TKE) profiles shown in Figure 5.50 exhibit similar features. Within the APG region, the peak value of the TKE is seen to increase and shift slightly away from the wall. Transitioning into the FPG region of this test section, the peak value decreases more dramatically, and the curve appears to begin to turn in on itself in an attempt to return to the type of profile seen earlier in the FPG test section (see Figure 5.44). Again, the condition of the upstream flow appears to play a major role in specifying the TKE profiles at each flow station. In other words, the profile in the FPG portion of this test section still retains many of the features of the APG profiles, while obviously moving towards the overall shape of the profiles seen in the FPG test section.

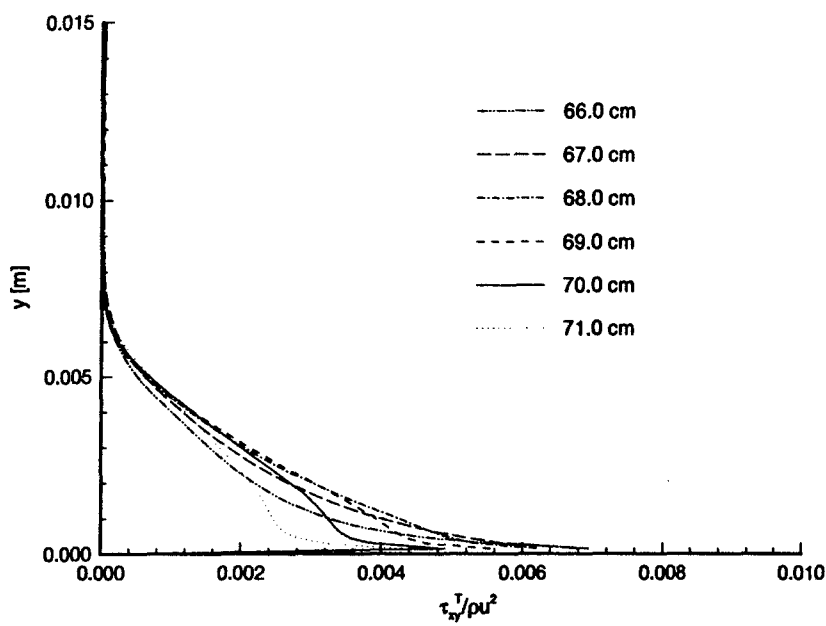


Figure 5.49 Nondimensional Turbulent Shear Stress vs y , APG Test Section

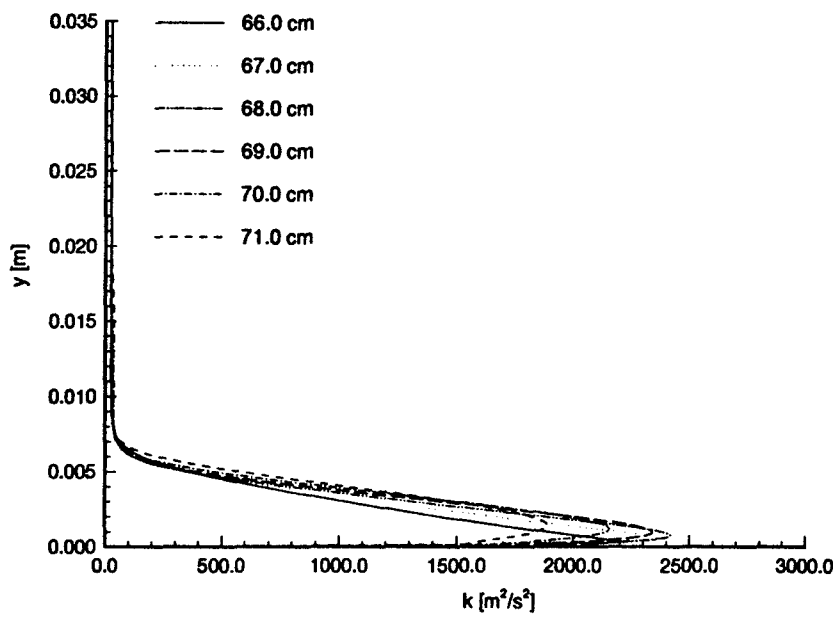


Figure 5.50 Turbulent Kinetic Energy vs y , APG Test Section

The eddy viscosity profiles (see Figure 5.51) in the APG test section behave in a similar manner. From FS 66.0 to FS 69.0, the peak eddy viscosity increases at a fairly constant rate and does not shift vertically within the boundary layer. The peak eddy viscosity at FS 70.0 is greater than that at FS 69.0 but has begun to move away from the wall, as was seen in the FPG test section. This seems to indicate that the maximum eddy viscosity lies somewhere between FS 69.0 and 70.0, on the same y plane as is seen between FS 66.0 and FS 69.0. Then, as the adverse pressure gradient diminishes in strength and the gradient becomes favorable, the peak eddy viscosity decreases and moves towards the boundary layer edge, as seen at FS 70.0 and 71.0. As before, this appears to be the mechanism responsible for shifting the TKE profile towards the boundary layer edge. Note that the eddy viscosity in the region between the shock wave and the lower test section wall is higher than that above the shock, indicating perhaps that the shock wave itself limits the extent of the APG to the region close to the wall. In the region below the shock wave but outside the boundary layer, eddy viscosity is seen to increase under the influence of the APG.

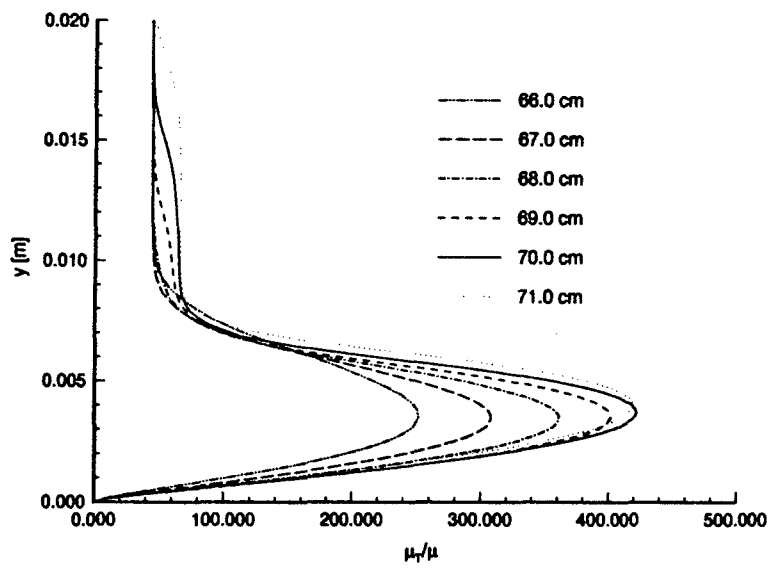


Figure 5.51 μ_T/μ vs y , $k - \omega$ Modeling

VI. Conclusions and Recommendations for Further Investigation

6.1 Conclusions

- 1. The $k - \omega$ turbulence model provides acceptable computational results for this family of flowfields.* Agreement between computed and experimental velocity and turbulent shear stress profiles is excellent, as is the agreement between computed and experimental wall shear stress in the zero pressure gradient test section. Wall shear predictions in the pressure gradient sections appear to follow published observations, but the lack of experimental data in these regions precludes direct comparison. All pertinent flowfield features have been accurately predicted numerically using this model. Finally, $k - \omega$ computations produced significantly better results than the corresponding Baldwin-Lomax computations.
- 2. Flowfield history plays a significant role in the determination of flowfield properties at every station in the flowfield.* Velocity and shear stress profiles evolve under the influence of both local and non-local flow features. Failing to account for the non-local flow features will introduce errors into the solution. Although FPG flowfield computations appear to be fairly insensitive to variations in upstream boundary conditions, ZPG and APG flowfield calculations are extremely sensitive to such variations.
- 3. Favorable pressure gradients tend to damp out turbulent fluctuations in compressible boundary layer flow.* The effect of the imposition of a favorable pressure gradient on the flowfields studied was to reduce the turbulent shear stress and alter the distribution of the turbulent kinetic energy through the boundary layer. Wall shear stress is also reduced in regions of favorable pressure gradient.
- 4. Adverse pressure gradients tend to increase the magnitude of the turbulent fluctuations in compressible boundary layer flowfields.* The effect of an adverse pressure gradient on the flowfields studied was to increase the turbulent shear stress through the boundary layer. Additionally, the peak turbulent kinetic energy and the wall shear stress are increased under the influence of the adverse pressure gradient.

6.2 Recommendations for Further Investigation

- 1. Decrease the solution time by enabling the implicit solution of the $k - \omega$ equations.*
If running in implicit mode, the flow solver in its present form utilizes Symmetric Gauss-Seidel Simultaneous Over-Relaxation (SOR) by Lines to rapidly advance the solution utilizing CFL numbers as high as 1.0×10^6 . In this mode, converged laminar solutions are possible in as few as 200 iterations. Enabling the solution of the k and ω equations to proceed at this rate would significantly reduce computation time, dramatically increasing this code's utility.
- 2. Move on to more challenging flowfields.* Now that the performance of this algorithm/turbulence model combination has been documented for compressible turbulent flows involving mild pressure gradients, evaluate its applicability to separated flows or flows over more complex geometries. Specifically, the supersonic slot injection flowfields studied by Tucker (23) stand out as excellent test cases for an investigation of this nature.
- 3. Integrate additional sophisticated turbulence models.* For the mild pressure gradient cases presented in this study, the Baldwin-Lomax turbulence model is relatively well behaved and helps to provide a baseline against which the performance of the $k - \omega$ model may be judged. For the massively separated flows mentioned above, algebraic models such as Baldwin-Lomax tend not to fare very well. The addition of a Reynolds-Stress turbulence model, directly solving the Reynolds-stress equation, will provide additional capabilities for computations involving more challenging flowfields. Failing that, the addition of one or several other two-equation models will enhance this code's utility as an analysis tool and serve as a basis for comparison for investigations involving these more complicated flowfields.

Appendix A. Strong Conservation Law form of Governing Differential Equations

This section presents the transformation of the governing equations from Cartesian form to the Strong Conservation Law form. The governing partial differential equations in vector form in Cartesian coordinates

$$\frac{\partial U}{\partial t} + \frac{\partial F}{\partial x} + \frac{\partial G}{\partial y} = 0 \quad (\text{A.1})$$

may be recast using the chain rule of partial differentiation

$$\frac{\partial F}{\partial x} = \xi_x \frac{\partial F}{\partial \xi} + \eta_x \frac{\partial F}{\partial \eta} \quad (\text{A.2})$$

$$\frac{\partial G}{\partial y} = \xi_y \frac{\partial G}{\partial \xi} + \eta_y \frac{\partial G}{\partial \eta} \quad (\text{A.3})$$

into the Weak (or Chain Rule) Conservation form of the governing equations

$$\frac{\partial U}{\partial t} + \xi_x \frac{\partial F}{\partial \xi} + \eta_x \frac{\partial F}{\partial \eta} + \xi_y \frac{\partial G}{\partial \xi} + \eta_y \frac{\partial G}{\partial \eta} = 0 \quad (\text{A.4})$$

The next step in the transformation is to divide the above equation by the Jacobian of the forward transformation and regroup

$$\frac{1}{J} \frac{\partial U}{\partial t} + \left(\frac{\xi_x}{J} \frac{\partial F}{\partial \xi} + \frac{\xi_y}{J} \frac{\partial G}{\partial \xi} \right) + \left(\frac{\eta_x}{J} \frac{\partial F}{\partial \eta} + \frac{\eta_y}{J} \frac{\partial G}{\partial \eta} \right) = 0 \quad (\text{A.5})$$

The first term in parentheses on the LHS may be re-expressed as

$$\frac{\xi_x}{J} F_\xi + \frac{\xi_y}{J} G_\xi = \left(\frac{\xi_x}{J} F + \frac{\xi_y}{J} G \right)_\xi - \left(\frac{\xi_x}{J} \right)_\xi F - \left(\frac{\xi_y}{J} \right)_\xi G \quad (\text{A.6})$$

Similarly, the second term in parentheses may be expressed as

$$\frac{\eta_x}{J} F_\eta + \frac{\eta_y}{J} G_\eta = \left(\frac{\eta_x}{J} F + \frac{\eta_y}{J} G \right)_\eta - \left(\frac{\eta_x}{J} \right)_\eta F - \left(\frac{\eta_y}{J} \right)_\eta G \quad (\text{A.7})$$

Inserting these two terms into Equation A.5 and re-grouping yields

$$\frac{1}{J} \frac{\partial U}{\partial t} + \left(\frac{\xi_x F + \xi_y G}{J} \right)_\xi + \left(\frac{\eta_x F + \eta_y G}{J} \right)_\eta - \left[\left(\frac{\xi_x}{J} \right)_\xi + \left(\frac{\eta_x}{J} \right)_\eta \right] F - \left[\left(\frac{\xi_y}{J} \right)_\xi + \left(\frac{\eta_y}{J} \right)_\eta \right] G = 0 \quad (\text{A.8})$$

Re-expressing the terms in square brackets in terms of the metrics of the inverse transformation (see Appendix D) reveals that

$$\left(\frac{\xi_x}{J} \right)_\xi + \left(\frac{\eta_x}{J} \right)_\eta = \left(\frac{y_\eta}{\tilde{J} J} \right)_\xi + \left(\frac{-y_\xi}{\tilde{J} J} \right)_\eta \equiv 0 \quad (\text{A.9})$$

$$\left(\frac{\xi_y}{J} \right)_\xi + \left(\frac{\eta_y}{J} \right)_\eta = \left(\frac{-x_\eta}{\tilde{J} J} \right)_\xi + \left(\frac{x_\xi}{\tilde{J} J} \right)_\eta \equiv 0 \quad (\text{A.10})$$

Finally, the strong conservation law form of the governing equations is obtained

$$\frac{1}{J} \frac{\partial U}{\partial t} + \left(\frac{\xi_x F + \xi_y G}{J} \right)_\xi + \left(\frac{\eta_x F + \eta_y G}{J} \right)_\eta = 0 \quad (\text{A.11})$$

Now, defining

$$\bar{F} = \left(\frac{\xi_x F + \xi_y G}{J} \right) \quad (\text{A.12})$$

and

$$\bar{G} = \left(\frac{\eta_x F + \eta_y G}{J} \right) \quad (\text{A.13})$$

the strong conservation law form of the governing equations may be rewritten as

$$\frac{U_t}{J} + \bar{F}_\xi + \bar{G}_\eta = 0 \quad (\text{A.14})$$

Appendix B. Finite Volume Method Overview

This section presents an overview of the Finite Volume method, based on the presentation given in Buter (3). Consider the governing differential equations of fluid mechanics in strong conservation form

$$\frac{1}{J} \frac{\partial U}{\partial t} + \frac{\partial \bar{F}}{\partial \xi} + \frac{\partial \bar{G}}{\partial \eta} = 0 \quad (\text{B.1})$$

If this equation is integrated over a stationary control volume with vertices $abcd$, as shown in Figure B, this equation becomes

$$\frac{1}{J} \int_{abcd} \left(\frac{\partial U}{\partial t} \right) d\xi d\eta = - \int_{abcd} \left(\frac{\partial \bar{F}}{\partial \xi} + \frac{\partial \bar{G}}{\partial \eta} \right) d\xi d\eta \quad (\text{B.2})$$

Applying Green's Theorem (13) to the right hand side of the above equation yields

$$\frac{1}{J} \int_{abcd} \left(\frac{\partial U}{\partial t} \right) d\xi d\eta = - \oint_{abcd} (Fd\eta - Gd\xi) \quad (\text{B.3})$$

where the line integral is evaluated by integrating counterclockwise around the cell. Referring to Figure B, Equation B.3 may be represented by the following finite approximation

$$\begin{aligned} \frac{1}{J} \left(\frac{U^{n+1} - U^n}{\delta t} \right) \Delta\xi \Delta\eta &= \\ &- [F_S \Delta\eta_{ab} + F_E \Delta\eta_{bc} + F_N \Delta\eta_{cd} + F_W \Delta\eta_{da}] \\ &+ [G_S \Delta\xi_{ab} + G_E \Delta\xi_{bc} + G_N \Delta\xi_{cd} + G_W \Delta\xi_{da}] \end{aligned} \quad (\text{B.4})$$

where F_E refers to the evaluation of F at point E and so on. Referring once again the uniform, unitary computational mesh in Figure B, it is clear that

$$\Delta\eta_{ab} = \Delta\eta_{cd} = \Delta\xi_{bc} = \Delta\xi_{da} = 0$$

$$\Delta\eta_{bc} = \Delta\xi_{ab} = 1$$

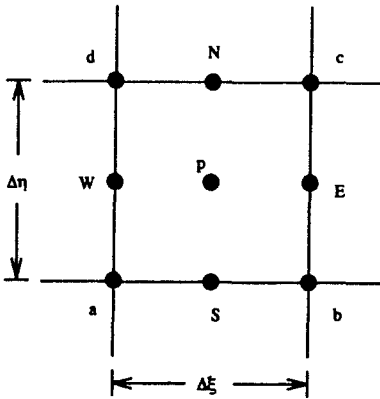


Figure B.1 Finite Volume Cell in Computational Domain

$$\Delta\eta_{da} = \Delta\xi_{cd} = -1$$

which, when inserted into Equation B.4 yields

$$\frac{1}{J} \left(\frac{U^{n+1} - U^n}{\delta t} \right) = G_C + G_N - F_E - F_W \quad (\text{B.5})$$

Finally, defining $\delta U \equiv U^{n+1} - U^n$ and multiplying through by $J\delta t$ yields

$$\delta U = J\delta t [G_S - G_N + F_W - F_E] \quad (\text{B.6})$$

Appendix C. Extrapolation and Limiting

In cell centered, finite volume codes, no flowfield information is stored at the cell interfaces. Finite differences involving the fluxes \bar{F} and \bar{G} , however, require the evaluation of these fluxes at those interfaces. Therefore, approximations of the flowfield properties at the interfaces are required. A first order approximation assumes that the flux at the interface is the same as the flux at the cell center. A second order approximation extrapolates interface values using the value of the flux vector at the cell center and that of the cell immediately upstream. These two methods of extrapolation are shown for the left state in Figure C.1. From this figure it is obvious that second order extrapolation utilizes more flowfield information and therefore should provide better results. Unfortunately, second order extrapolation breaks down at local maxima and minima, where extrapolation based on upstream property variance can induce overshoots at cell interfaces. Thus, any extrapolation greater than first order must be controlled, or limited, to prevent oscillations in the vicinity of local maxima or minima. Yee (28) developed the MINMOD limiting scheme to address this difficulty. MINMOD is neither first nor second order, but something in between, providing most of the benefits of second order extrapolation everywhere but at local minima and maxima, where it reverts to first order. This section describes MINMOD limiting as implemented by Gaitonde (8) within FPFV.

C.1 Left State

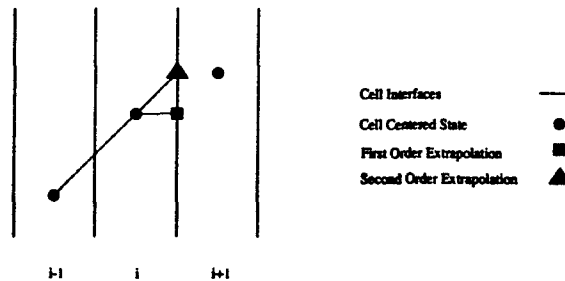


Figure C.1 First and Second Order Extrapolation, Left State

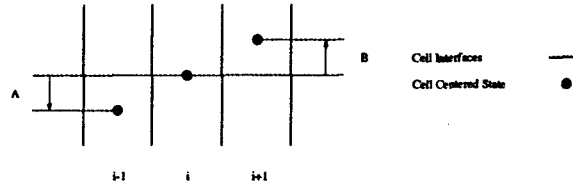


Figure C.2 Sign Convention for Extrapolation and Limiting, Left State

If ϕ is a flowfield variable to be extrapolated, the left state is computed using $\phi_{i-1,j}$, $\phi_{i,j}$, and $\phi_{i+1,j}$. The sign convention for extrapolation of the left state is shown in Figure C.2, with A and B positive for the configuration shown, or

$$\begin{aligned} B &= \phi_{i+1,j} - \phi_{i,j} \\ A &= \phi_{i,j} - \phi_{i-1,j} \end{aligned} \quad (C.1)$$

In general, not including the case where $A = B = 0$, six cases must be considered and handled differently, depending on the signs and magnitudes of A and B. All six cases are handled within FPFV rather elegantly by the following functional evaluation

$$\phi_{i+\frac{1}{2},j}^L = \phi_{i,j} + \frac{FL1(A,B)}{2} \quad (C.2)$$

where $FL1(A,B)$ is a function defined by

$$FL1(A,B) = \text{sign}(1,A)\max(0,\min(|A|,B\text{sign}(1,A))) \quad (C.3)$$

where

$$\text{sign}(A,B) = \begin{cases} |A| : B \geq 0 \\ -|A| : B < 0 \end{cases} \quad (C.4)$$

These functional evaluations are perhaps better understood if presented in a graphical manner, as is done below for the six cases under consideration

Case 1 : $A > B > 0$: See Figure C.3, $\phi_{i+\frac{1}{2},j}^L = \phi_{i,j} + \frac{B}{2}$

Case 2 : $B > A > 0$: See Figure C.4, $\phi_{i+\frac{1}{2},j}^L = \phi_{i,j} + \frac{A}{2}$

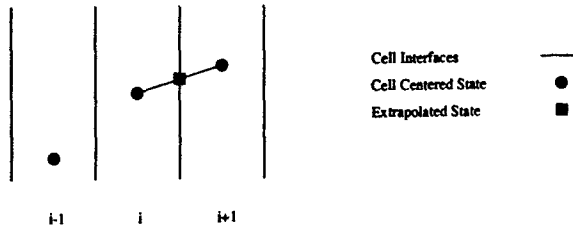


Figure C.3 $A > B > 0$, Left State

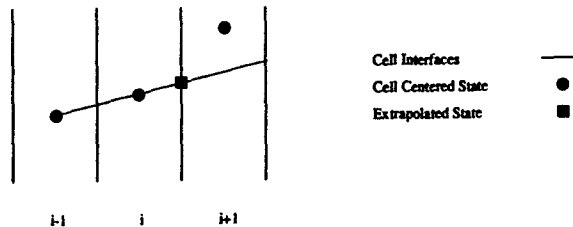


Figure C.4 $B > A > 0$, Left State

Case 3 : $A, B < 0, |A| > |B|$: See Figure C.5, $\phi_{i+\frac{1}{2},j}^L = \phi_{i,j} - \frac{|B|}{2}$

Case 4 : $A, B < 0, |B| > |A|$: See Figure C.6, $\phi_{i+\frac{1}{2},j}^L = \phi_{i,j} - \frac{|A|}{2}$

Case 5 : $A > 0, B < 0$: Local Maximum. See Figure C.7, $\phi_{i+\frac{1}{2},j}^L = \phi_{i,j}$

Case 6 : $A < 0, B > 0$: Local Minimum. See Figure C.8, $\phi_{i+\frac{1}{2},j}^L = \phi_{i,j}$

C.2 Right State

Still using ϕ as the flowfield variable to be extrapolated, the right state is computed using $\phi_{i,j}$, $\phi_{i+1,j}$, and $\phi_{i+2,j}$. The sign convention for extrapolation of the right state is shown in Figure C.9, with A and B positive for the configuration shown, or

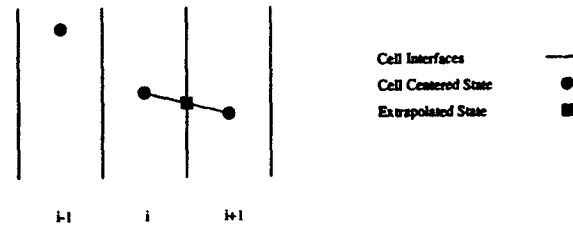


Figure C.5 $A, B < 0, |A| > |B|$, Left State

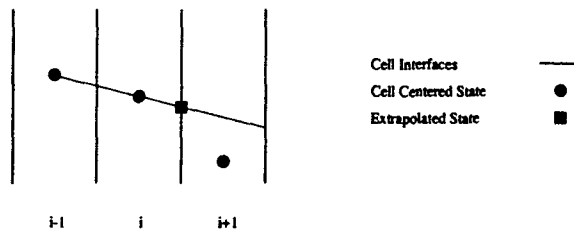


Figure C.6 A, B < 0, |B| > |A|, Left State

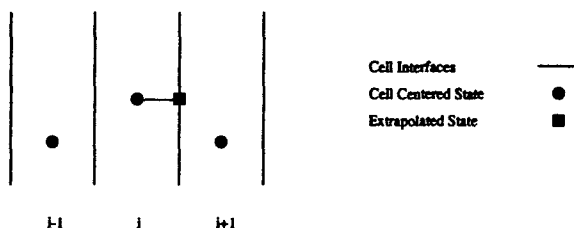


Figure C.7 Local Maximum, Left State

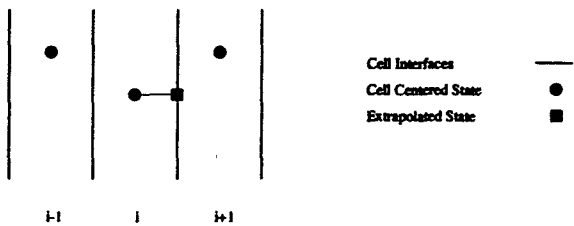


Figure C.8 Local Minimum, Left State

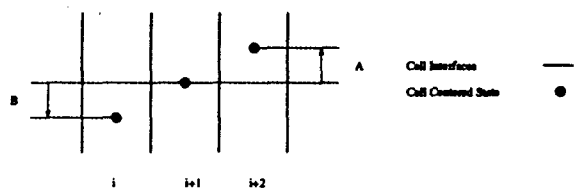


Figure C.9 Sign Convention for Extrapolation and Limiting, Right State

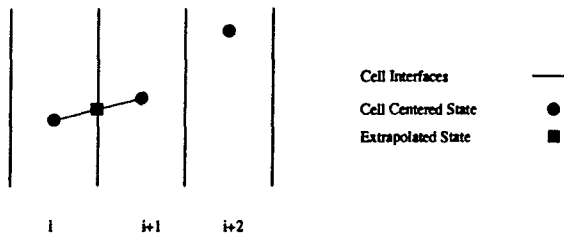


Figure C.10 $A > B > 0$, Right State

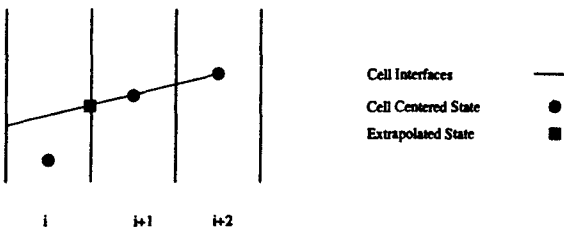


Figure C.11 $B > A > 0$, Right State

$$\begin{aligned} A &= \phi_{i+2,j} - \phi_{i+1,j} \\ B &= \phi_{i+1,j} - \phi_{i,j} \end{aligned} \quad (C.5)$$

Once again, six cases must be considered and handled differently, depending on the signs and magnitudes of A and B. The functional evaluation presented in the previous section is used with the following modification

$$\phi_{i+\frac{1}{2},j}^R = \phi_{i+1,j} - \frac{FL1(A,B)}{2} \quad (C.6)$$

where $FL1(A,B)$ is as defined in Equation C.3. Graphically, the six cases under consideration are as shown below

Case 1 : $A > B > 0$: See Figure C.10, $\phi_{i+\frac{1}{2},j}^R = \phi_{i+1,j} - \frac{B}{2}$

Case 2 : $B > A > 0$: See Figure C.11, $\phi_{i+\frac{1}{2},j}^R = \phi_{i+1,j} - \frac{A}{2}$

Case 3 : $A, B < 0, |A| > |B|$: See Figure C.12, $\phi_{i+\frac{1}{2},j}^R = \phi_{i,j} + \frac{|B|}{2}$

Case 4 : $A, B < 0, |B| > |A|$: See Figure C.13, $\phi_{i+\frac{1}{2},j}^R = \phi_{i,j} + \frac{|A|}{2}$

Case 5 : $A > 0, B < 0$: Local Maximum. See Figure C.14, $\phi_{i+\frac{1}{2},j}^R = \phi_{i+1,j}$

Case 6 : $A < 0, B > 0$: Local Minimum. See Figure C.15, $\phi_{i+\frac{1}{2},j}^R = \phi_{i+1,j}$

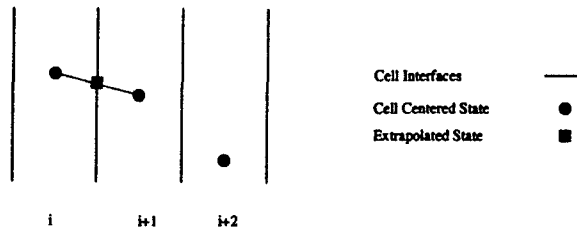


Figure C.12 $A, B < 0, |A| > |B|$, Right State

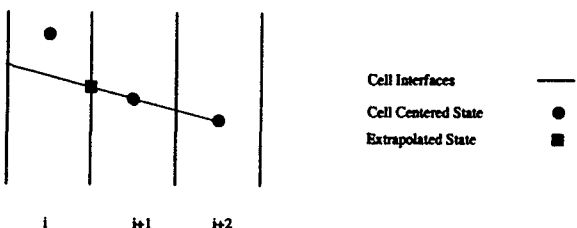


Figure C.13 $A, B < 0, |B| > |A|$, Right State

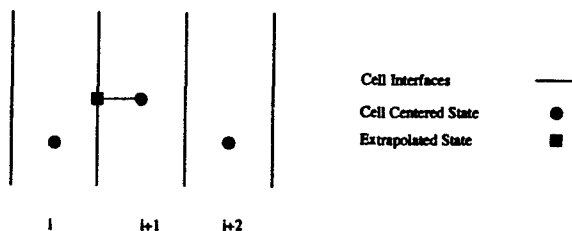


Figure C.14 Local Maximum, Right State

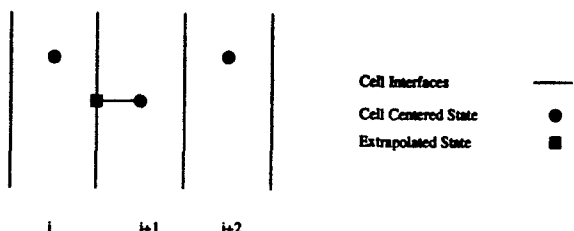


Figure C.15 Local Minimum, Right State

Appendix D. Coordinate Transformation

Numerically solving the above system of differential equations is most often facilitated by transforming the frequently irregular physical domain into a rectilinear computational domain using evenly spaced grid points. This section presents the details of a general coordinate transformation as described by Buter (2).

Thus, the physical (x, y) space is mapped into the computational (ξ, η) space using the following coordinate transformation

$$\xi = \xi(x, y) \quad (\text{D.1})$$

$$\eta = \eta(x, y) \quad (\text{D.2})$$

Applying the chain rule of partial differentiation to the above transformation yields

$$\frac{\partial}{\partial x} = \xi_x \frac{\partial}{\partial \xi} + \eta_x \frac{\partial}{\partial \eta} \quad (\text{D.3})$$

$$\frac{\partial}{\partial y} = \xi_y \frac{\partial}{\partial \xi} + \eta_y \frac{\partial}{\partial \eta} \quad (\text{D.4})$$

For the forward transformation, the total derivatives may be expressed as

$$d\xi = \xi_x dx + \xi_y dy \quad (\text{D.5})$$

$$d\eta = \eta_x dx + \eta_y dy \quad (\text{D.6})$$

or

$$\begin{bmatrix} d\xi \\ d\eta \end{bmatrix} = \begin{bmatrix} \xi_x & \xi_y \\ \eta_x & \eta_y \end{bmatrix} \begin{bmatrix} dx \\ dy \end{bmatrix} \quad (\text{D.7})$$

where the Jacobian of the forward transformation may be defined as

$$J = \xi_x \eta_y - \eta_x \xi_y \quad (\text{D.8})$$

Similarly, for the inverse transformation, the total derivatives may be expressed as

$$dx = x_\xi d\xi + x_\eta d\eta \quad (\text{D.9})$$

$$dy = y_\xi d\xi + y_\eta d\eta \quad (\text{D.10})$$

or

$$\begin{bmatrix} dx \\ dy \end{bmatrix} = \begin{bmatrix} x_\xi & x_\eta \\ y_\xi & y_\eta \end{bmatrix} \begin{bmatrix} d\xi \\ d\eta \end{bmatrix} \quad (\text{D.11})$$

Combining Equations D.7 and D.11 yields

$$\begin{bmatrix} x_\xi & x_\eta \\ y_\xi & y_\eta \end{bmatrix} = \begin{bmatrix} \xi_x & \xi_y \\ \eta_x & \eta_y \end{bmatrix}^{-1} \quad (\text{D.12})$$

If the Jacobian of the forward transformation is defined as

$$J = \xi_x \eta_y - \eta_x \xi_y \quad (\text{D.13})$$

the relationships between the metrics of the forward and inverse transformations as

$$\xi_x = J y_\eta \quad (\text{D.14})$$

$$\xi_y = -J x_\eta \quad (\text{D.15})$$

$$\eta_x = -J y_\xi \quad (\text{D.16})$$

$$\eta_y = J x_\xi \quad (\text{D.17})$$

Similar manipulations reveal that the Jacobian of the inverse transformation may be defined as

$$\tilde{J} = x_\xi y_\eta - y_\xi x_\eta \quad (\text{D.18})$$

and that the Jacobians of the forward and inverse transformations are related by

$$\tilde{J} = \frac{1}{J} \quad (\text{D.19})$$

Appendix E. Time-Averaged Navier-Stokes Equations

This appendix presents an overview of Reynolds and Favré averaging as presented by Bowersox (1) and the forms of the Navier-Stokes equations obtained through the use of each technique.

E.1 Reynolds Averaging

In Reynolds averaging, flow variables are replaced by the sum of a mean value and a fluctuating component, as shown below for the “random” flow variable ϕ .

$$\phi = \bar{\phi} + \phi' \quad (\text{E.1})$$

After these substitutions have been made, the governing equations are expanded and then time averaged. The time average of fluctuating components is, by definition, zero, so terms involving the product of a mean and a fluctuating component disappear. products of two or more fluctuation terms do not necessarily go to zero physically, so they are preserved through the averaging process. Consider the Continuity equation in Cartesian coordinates

$$\frac{\partial \rho}{\partial t} + \frac{\partial \rho u}{\partial x} + \frac{\partial \rho v}{\partial y} = 0 \quad (\text{E.2})$$

after substituting in the mean and fluctuating components for all flow variables and expanding, the above equation becomes

$$\frac{\partial(\bar{\rho} + \rho')}{\partial t} + \frac{\partial(\bar{\rho}\bar{u} + \bar{\rho}u' + \rho'\bar{u} + \rho'u')}{\partial x} + \frac{\partial(\bar{\rho}\bar{v} + \bar{\rho}v' + \rho'\bar{v} + \rho'v')}{\partial y} = 0 \quad (\text{E.3})$$

Time averaging the resulting equation yields the Reynolds-averaged form

$$\frac{\partial \bar{\rho}}{\partial t} + \frac{\partial(\bar{\rho}\bar{u} + \overline{\rho' u'})}{\partial x} + \frac{\partial(\bar{\rho}\bar{v} + \overline{\rho' v'})}{\partial y} = 0 \quad (\text{E.4})$$

which may be written in indicial notation as

$$\frac{\partial \bar{p}}{\partial t} + \frac{\partial (\bar{\rho} \bar{u}_j + \overline{\rho' u'_j})}{\partial x_j} = 0 \quad (E.5)$$

Similar manipulations, when performed on the momentum equations (22), yield

$$\frac{\partial (\bar{\rho} \bar{u}_i + \overline{\rho' u'_i})}{\partial t} + \frac{\partial \bar{\rho} \bar{u}_i \bar{u}_j}{\partial x_j} = - \frac{\partial \bar{p}}{\partial x_i} + \frac{\partial \tau_{ij} + \tau_{ij}^T}{\partial x_j} \quad (E.6)$$

where the Reynolds stress tensor τ_{ij}^T contains the additional fluctuation terms added to the momentum equations. In indicial notation, the Reynolds stress tensor takes the following form:

$$\tau_{ij}^T \equiv - \left(\bar{\rho} \overline{u'_i u'_j} + \bar{u}_i \overline{\rho' u'_j} + \bar{u}_j \overline{\rho' u'_i} + \overline{\rho' u'_i u'_j} \right) \quad (E.7)$$

The Reynolds averaged form of the Energy equation (22) in terms of the total enthalpy is

$$\frac{\partial (\bar{\rho} \bar{h}_o + \overline{\rho' h'_o})}{\partial t} + \frac{\partial \bar{\rho} \bar{h}_o \bar{u}_j}{\partial x_j} = - \frac{\partial (\bar{u}_i \overline{\tau_{ij}} + \overline{u' \tau'_{ij}} - q_j - q_j^T)}{\partial x_j} \quad (E.8)$$

where the turbulent heat flux is defined as

$$q_j^T \equiv \bar{\rho} \overline{h'_o u'_i} + \bar{h}_o \overline{\rho' u'_i} + \bar{u}_i \overline{\rho' h'_o} + \overline{\rho' h'_o u'_i} \quad (E.9)$$

E.2 Favre Averaging

The form of Reynolds stress tensor generated by Reynolds averaging contains four terms that must be modeled if the system of equations is to be closed. In an attempt to reduce the number of terms that must be modeled, a closer look at the Navier-Stokes Equations suggests that mass averaging the flow variables is another way to account for the turbulent fluctuations within the flow. The premise of replacing flow quantities with a mean plus a fluctuating component does not change, but the rules by which the averaging

process eliminates combinations of terms changes commensurate with the philosophy of mass, or Favrè , averaging. Consider once again a random flow variable, ϕ :

$$\phi = \bar{\phi} + \phi'' \quad (\text{E.10})$$

where

$$\bar{\phi} \equiv \frac{\overline{\rho\phi}}{\bar{\rho}} \quad (\text{E.11})$$

In Favrè averaging, the averaging process eliminates only those terms that involve the product of the mean density and a fluctuating term. This feature arises from the following set of manipulations

$$\rho\phi = \rho\bar{\phi} + \rho\phi'' \quad (\text{E.12})$$

Averaging yields

$$\begin{aligned} \overline{\rho\phi} &= \overline{\rho\bar{\phi}} + \overline{\rho\phi''} \\ &= \bar{\rho}\bar{\phi} + \overline{\rho\phi''} \end{aligned} \quad (\text{E.13})$$

which, when combined with Equation E.11, yields

$$\overline{\rho\phi} = \bar{\rho}\frac{\overline{\rho\bar{\phi}}}{\bar{\rho}} + \overline{\rho\phi''} \quad (\text{E.14})$$

or

$$\overline{\rho\phi''} = 0 \quad (\text{E.15})$$

Applying these rules to the governing differential equations (22) yields the Favrè averaged form of the Continuity Equation

$$\frac{\partial \bar{\rho}}{\partial t} + \frac{\partial \bar{\rho} \bar{u}_i}{\partial x_i} = 0 \quad (\text{E.16})$$

the Momentum Equations,

$$\frac{\partial (\bar{\rho} \bar{u}_i)}{\partial t} + \frac{\partial \bar{\rho} \bar{u}_i \bar{u}_j}{\partial x_j} = - \frac{\partial \bar{p}}{\partial x_i} + \frac{\partial \tau_{ij} + \tau_{ij}^T}{\partial x_j} \quad (\text{E.17})$$

where the Reynolds stress tensor τ_{ij}^T is defined in indicial notation as

$$\tau_{ij}^T \equiv -\bar{\rho} \overline{u_i'' u_j''} \quad (\text{E.18})$$

and the Energy equation

$$\frac{\partial (\bar{\rho} \bar{h})}{\partial t} + \frac{\partial \bar{\rho} \bar{h} \bar{u}_j}{\partial x_j} = \frac{\partial \bar{p}}{\partial t} + \bar{u}_j \frac{\partial \bar{p}}{\partial x_j} + \overline{u_j'' \frac{\partial p}{\partial x_j}} + \frac{\partial (-\bar{q}_j - \bar{q}_j^T)}{\partial x_j} + \overline{\tau_{ij} \frac{\partial u_i''}{\partial x_j}} \quad (\text{E.19})$$

where the turbulent heat flux is given by

$$\bar{q}_j^T = \overline{\rho h'' u_j''} \quad (\text{E.20})$$

Notice that the Reynolds stress tensor obtained through Favre Averaging contains three fewer terms than that obtained from Reynolds averaging. In fact, the Favré averaged term looks much like the “incompressible” portion of the Reynolds averaged term, as would be obtained by setting $\rho' = 0$. The following exercise more formally shows the relationship between the Favré -averaged and Reynolds-averaged terms. The instantaneous velocity may be represented in terms of both Reynolds-averaged and Favré -averaged variables

$$u = \bar{u} + u' = \bar{u} + u'' \quad (\text{E.21})$$

$$v = \bar{v} + v' = \tilde{v} + v''$$

Solving for the ' quantities,

$$\begin{aligned} u' &= \tilde{u} - \bar{u} + u'' \\ v' &= \tilde{v} - \bar{v} + v'' \end{aligned} \quad (\text{E.22})$$

Next, take the time-average the Favrè portions of Equation E.21

$$\begin{aligned} \bar{u} &= \bar{\tilde{u}} + \bar{u}'' = \bar{\tilde{u}} + \bar{u}'' \\ \bar{v} &= \bar{\tilde{v}} + \bar{v}'' = \bar{\tilde{v}} + \bar{v}'' \end{aligned} \quad (\text{E.23})$$

and use them to replace the \bar{u} and \bar{v} terms in Equation E.22

$$\begin{aligned} u' &= \tilde{u} + u'' - \bar{\tilde{u}} - \bar{u}'' = u'' - \bar{u}'' \\ v' &= \tilde{v} + v'' - \bar{\tilde{v}} - \bar{v}'' = v'' - \bar{v}'' \end{aligned} \quad (\text{E.24})$$

Next, take the product of these two terms and multiply the result by the mean density

$$\bar{\rho} \bar{u}' \bar{v}' = \bar{\rho} \bar{u}'' \bar{v}'' - \bar{\rho} \bar{u}'' \bar{v}'' - \bar{\rho} \bar{v}'' \bar{u}'' + \bar{\rho} \bar{u}'' \bar{v}'' = \bar{\rho} \bar{u}'' \bar{v}'' - \bar{\rho} \bar{u}'' \bar{v}'' \quad (\text{E.25})$$

Then, remembering the principles of Favrè averaging in terms of a general flow variable ϕ

$$\begin{aligned}
\phi &= \tilde{\phi} + \phi'' \\
\bar{\phi} &= \tilde{\phi} + \bar{\phi}'' \\
\bar{\phi}'' &= \bar{\phi} - \tilde{\phi} \\
&= \bar{\phi} - \frac{\rho \phi}{\bar{\rho}} \\
&= \bar{\phi} - \frac{(\bar{\rho} + \rho')(\bar{\phi} + \phi')}{\bar{\rho}}
\end{aligned} \tag{E.26}$$

the Favrè fluctuating component may be re-written as

$$\bar{\phi}'' = -\frac{\rho' \phi'}{\bar{\rho}} \tag{E.27}$$

This result may be inserted into the right hand side (RHS) of Equation E.25 to yield

$$\bar{\rho} \bar{u}' \bar{v}' = \bar{\rho} \bar{u}'' \bar{v}'' + \frac{\rho' u'}{\bar{\rho}} \frac{\rho' v'}{\bar{\rho}} \tag{E.28}$$

If the second term on the RHS of this equation is negligible, as may be expected of a fourth-order fluctuation term, then the above relation reduces to

$$\bar{\rho} \bar{u}' \bar{v}' \approx \bar{\rho} \bar{u}'' \bar{v}'' \tag{E.29}$$

which supports the observation made previously. Thus, solving the Favrè averaged form of the governing equations neglects the effects of ρ' , manifested by the elimination of the fourth-order fluctuation term in the above expression. Justification for doing so lies in Morkovin's Hypothesis (17), which states that the effect of density fluctuations on turbulent flow may be neglected as long as the magnitude of the density fluctuations is small compared to the mean density. Miller (16) found that density fluctuations in the mean flow were on the order of 1%, but within the boundary layer the magnitude of these fluctuations increased to roughly 10%. This observation indicates that the effects of density fluctuations are not negligible and should therefore technically be considered for this flowfield. Modeling constraints, however, dictate that the Favrè averaged form of the governing equations, which by definition neglect density fluctuations, be used.

Appendix F. AFIT Supersonic Pressure-Vacuum Wind Tunnel

The coordinates for the contour of the AFIT Supersonic Pressure-Vacuum Wind Tunnel, beginning in the upstream settling chamber, are:

Ceiling			
x (in)	y (in)	x (in)	y (in)
0.0000E+00	3.2910E+00	2.2240E+00	2.2240E+00
1.5000E+00	3.2910E+00	2.2590E+00	2.1420E+00
1.5340E+00	3.2870E+00	2.2930E+00	2.0600E+00
1.5690E+00	3.2770E+00	2.3280E+00	1.9770E+00
1.6030E+00	3.2610E+00	2.3620E+00	1.8940E+00
1.6380E+00	3.2390E+00	2.3970E+00	1.8110E+00
1.6720E+00	3.2120E+00	2.4310E+00	1.7290E+00
1.7070E+00	3.1790E+00	2.4660E+00	1.6470E+00
1.7410E+00	3.1400E+00	2.5000E+00	1.5670E+00
1.7760E+00	3.0970E+00	2.5350E+00	1.4870E+00
1.8100E+00	3.0500E+00	2.5690E+00	1.4090E+00
1.8450E+00	2.9980E+00	2.6040E+00	1.3330E+00
1.8790E+00	2.9420E+00	2.6380E+00	1.2590E+00
1.9140E+00	2.8830E+00	2.6730E+00	1.1870E+00
1.9480E+00	2.8200E+00	2.7070E+00	1.1180E+00
1.9830E+00	2.7530E+00	2.7420E+00	1.0520E+00
2.0170E+00	2.6840E+00	2.7760E+00	9.8890E-01
2.0520E+00	2.6120E+00	2.8110E+00	9.2930E-01
2.0860E+00	2.5380E+00	2.8450E+00	8.7350E-01
2.1210E+00	2.4620E+00	2.8800E+00	8.2160E-01
2.1550E+00	2.3840E+00	2.9140E+00	7.7410E-01
2.1900E+00	2.3050E+00	2.9490E+00	7.3110E-01

Ceiling (continued)

x (in)	y (in)	x (in)	y (in)
2.9830E+00	6.9290E-01	5.1000E+00	1.2600E+00
3.0180E+00	6.5990E-01	5.3030E+00	1.3310E+00
3.0520E+00	6.3220E-01	5.5120E+00	1.4010E+00
3.0870E+00	6.1020E-01	5.7290E+00	1.4700E+00
3.1210E+00	5.9420E-01	5.9560E+00	1.5390E+00
3.1560E+00	5.8430E-01	6.1940E+00	1.6070E+00
3.1900E+00	5.8100E-01	6.4440E+00	1.6740E+00
3.2620E+00	5.8360E-01	6.7070E+00	1.7410E+00
3.3050E+00	5.8680E-01	6.9840E+00	1.8070E+00
3.3490E+00	5.9120E-01	7.2770E+00	1.8720E+00
3.3920E+00	5.9700E-01	7.5880E+00	1.9360E+00
3.4360E+00	6.0410E-01	7.9170E+00	2.0000E+00
3.4810E+00	6.1260E-01	8.2660E+00	2.0620E+00
3.5260E+00	6.2260E-01	8.6370E+00	2.1210E+00
3.5710E+00	6.3420E-01	9.0310E+00	2.1780E+00
3.6180E+00	6.4740E-01	9.4510E+00	2.2340E+00
3.6650E+00	6.6240E-01	9.8980E+00	2.2850E+00
3.7130E+00	6.7920E-01	1.0370E+01	2.3330E+00
3.7620E+00	6.9800E-01	1.0880E+01	2.3770E+00
3.8120E+00	7.1900E-01	1.1430E+01	2.4160E+00
3.8380E+00	7.3040E-01	1.2010E+01	2.4480E+00
4.0860E+00	8.4690E-01	1.2630E+01	2.4740E+00
4.5070E+00	1.0320E+00	1.3290E+01	2.4920E+00
4.7050E+00	1.1120E+00	1.4000E+01	2.5000E+00
4.9020E+00	1.1870E+00		

Floor

x (in)	y (in)	x (in)	y (in)
.0000E+00	-.2710E+01	.2397E+01	-.1230E+01
.1500E+01	-.2710E+01	.2431E+01	-.1148E+01
.1534E+01	-.2706E+01	.2466E+01	-.1066E+01
.1569E+01	-.2696E+01	.2500E+01	-.9857E+00
.1603E+01	-.2680E+01	.2535E+01	-.9062E+00
.1638E+01	-.2658E+01	.2569E+01	-.8283E+00
.1672E+01	-.2631E+01	.2604E+01	-.7521E+00
.1707E+01	-.2598E+01	.2638E+01	-.6780E+00
.1741E+01	-.2559E+01	.2673E+01	-.6063E+00
.1776E+01	-.2516E+01	.2707E+01	-.5372E+00
.1810E+01	-.2469E+01	.2742E+01	-.4709E+00
.1845E+01	-.2417E+01	.2776E+01	-.4079E+00
.1879E+01	-.2361E+01	.2811E+01	-.3483E+00
.1914E+01	-.2302E+01	.2845E+01	-.2925E+00
.1948E+01	-.2239E+01	.2880E+01	-.2406E+00
.1983E+01	-.2172E+01	.2914E+01	-.1931E+00
.2017E+01	-.2103E+01	.2949E+01	-.1501E+00
.2052E+01	-.2031E+01	.2983E+01	-.1119E+00
.2086E+01	-.1957E+01	.3018E+01	-.7888E-01
.2121E+01	-.1881E+01	.3052E+01	-.5122E-01
.2155E+01	-.1803E+01	.3087E+01	-.2923E-01
.2190E+01	-.1724E+01	.3121E+01	-.1317E-01
.2224E+01	-.1643E+01	.3156E+01	-.3339E-02
.2259E+01	-.1561E+01	.3190E+01	.0000E+00
.2293E+01	-.1479E+01	.3290E+01	.0000E+00
.2328E+01	-.1396E+01	.1400E+02	.0000E+00
.2362E+01	-.1313E+01		

Appendix G. Additional Figures

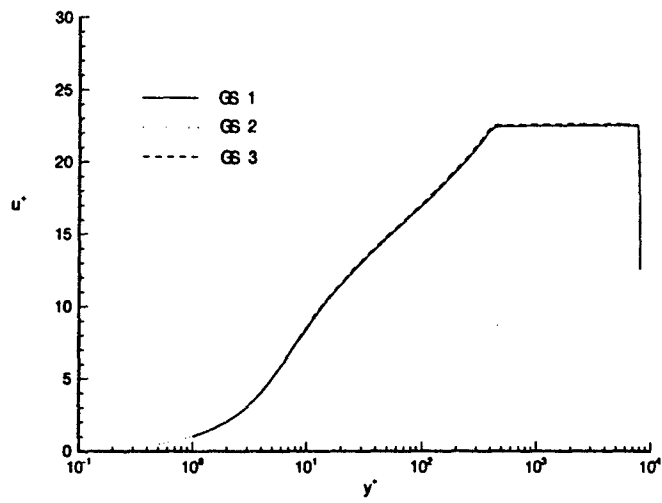


Figure G.1 u^+ (van Driest) vs y^+ , Upstream Flat Plate Test Section, FS 44.0, Normal Node Count Variation

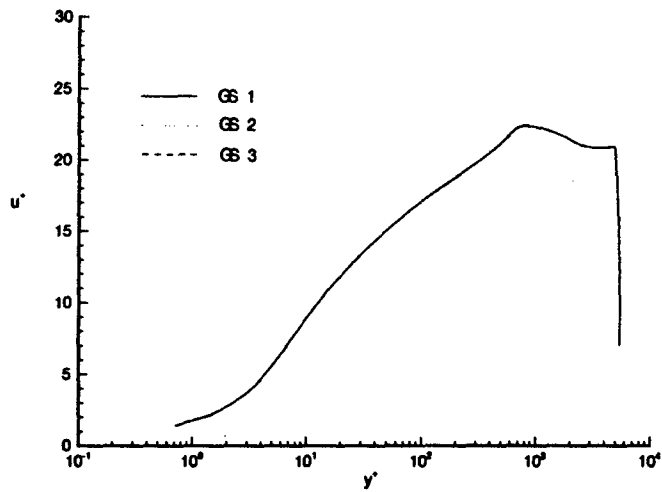


Figure G.2 u^+ (van Driest) vs y^+ , Favorable Pressure Gradient Section, FS 71.5, Normal Node Count Variation

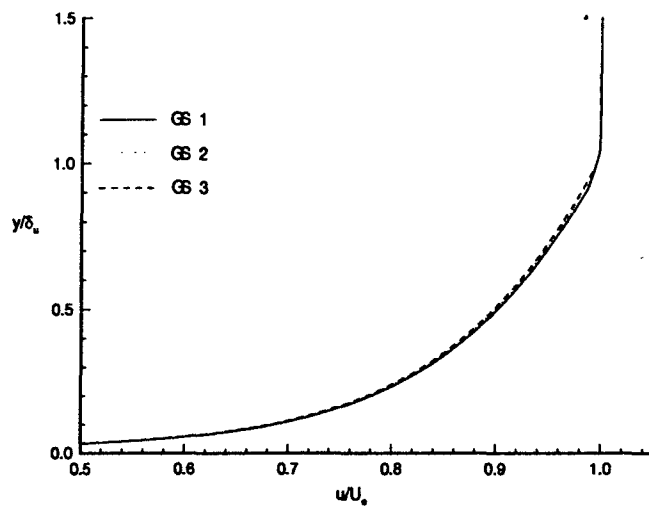


Figure G.3 Nondimensional Velocity Profile, Upstream Flat Plate Test Section, FS 44.0, Normal Node Count Variation

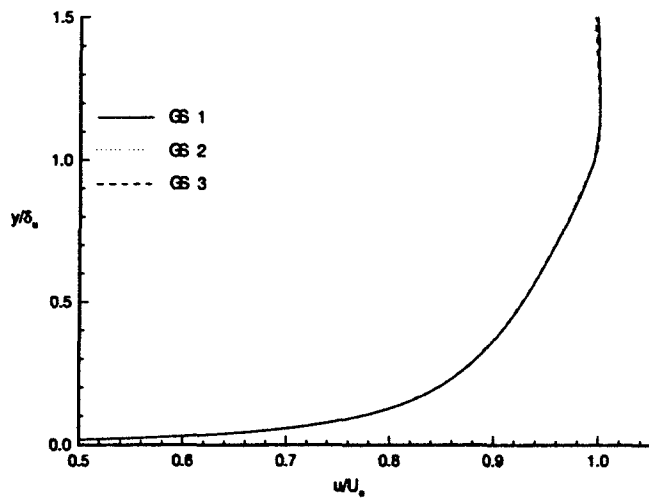


Figure G.4 Nondimensional Velocity Profile, Favorable Pressure Gradient Section, FS 71.5, Normal Node Count Variation

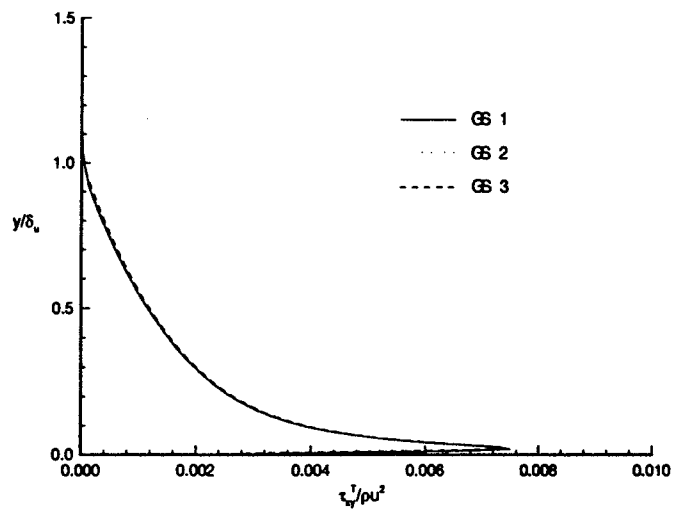


Figure G.5 Nondimensional Turbulent Shear Stress Profile, Upstream Flat Plate Test Section, FS 44.0, Normal Node Count Variation

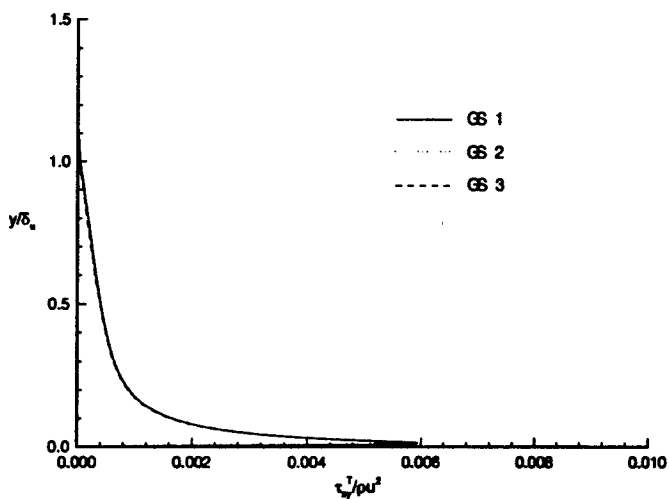


Figure G.6 Nondimensional Turbulent Shear Stress Profile, Favorable Pressure Gradient Section, FS 71.5, Normal Node Count Variation

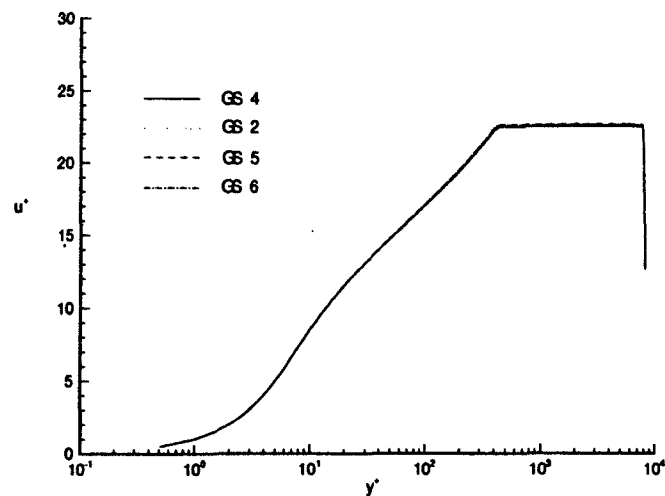


Figure G.7 u_+ (van Driest) vs y_+ , Upstream Flat Plate Test Section, FS 44.0, Streamwise Node Count Variation

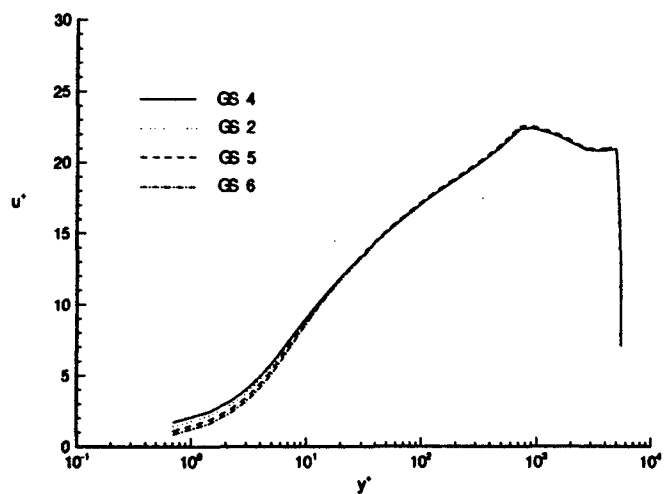


Figure G.8 u_+ (van Driest) vs y_+ , Favorable Pressure Gradient Section, FS 71.5, Streamwise Node Count Variation

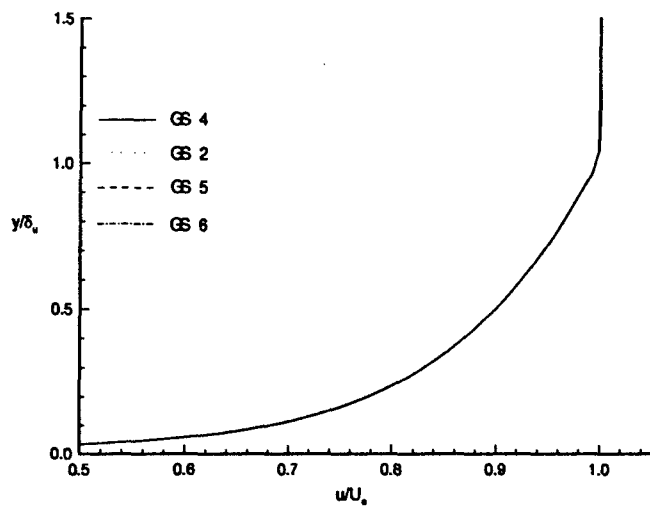


Figure G.9 Nondimensional Velocity Profile, Upstream Flat Plate Test Section, FS 44.0, Streamwise Node Count Variation

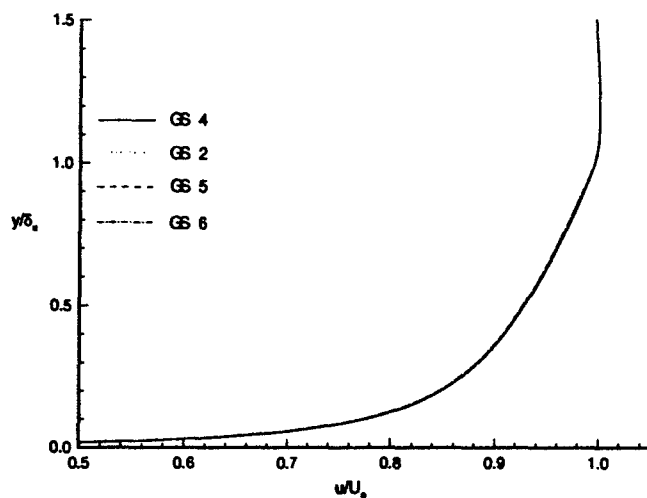


Figure G.10 Nondimensional Velocity Profile, Favorable Pressure Gradient Section, FS 71.5, Streamwise Node Count Variation

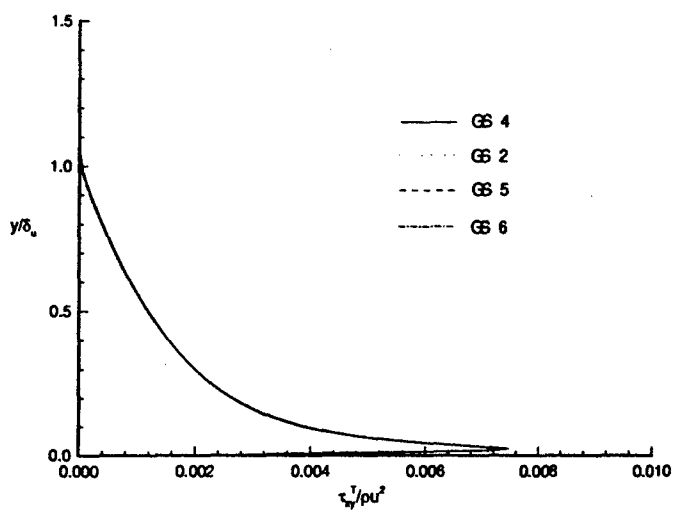


Figure G.11 Nondimensional Turbulent Shear Stress Profile, Upstream Flat Plate Test Section, FS 44.0, Streamwise Node Count Variation

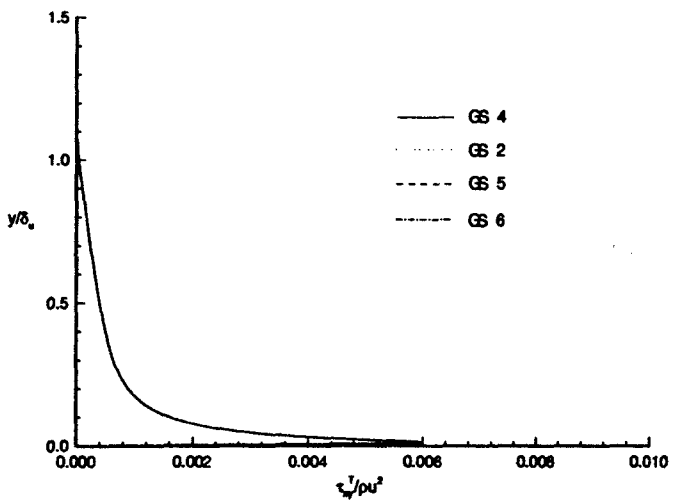


Figure G.12 Nondimensional Turbulent Shear Stress Profile, Favorable Pressure Gradient Section, FS 71.5, Streamwise Node Count Variation

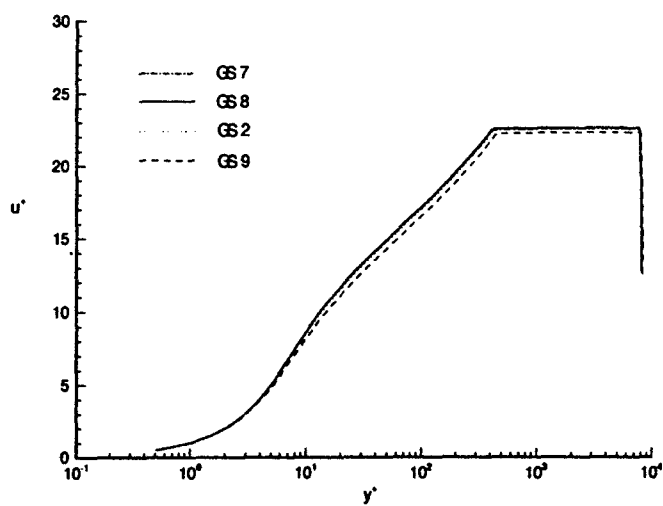


Figure G.13 u_+ (van Driest) vs y_+ , Upstream Flat Plate Test Section, FS 44.0, Wall Spacing Variation

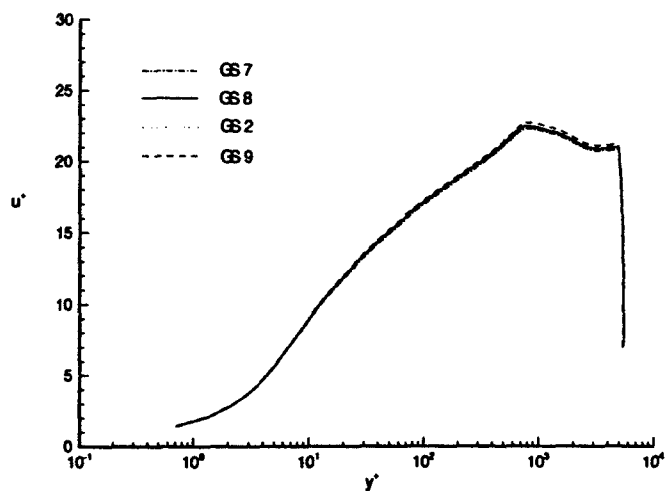


Figure G.14 u_+ (van Driest) vs y_+ , Favorable Pressure Gradient Section, FS 71.5, Wall Spacing Variation

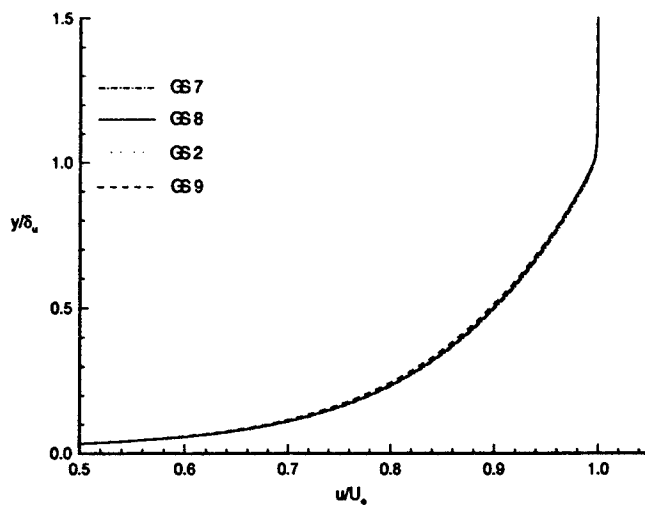


Figure G.15 Nondimensional Velocity Profile, Upstream Flat Plate Test Section, FS 44.0, Wall Spacing Variation

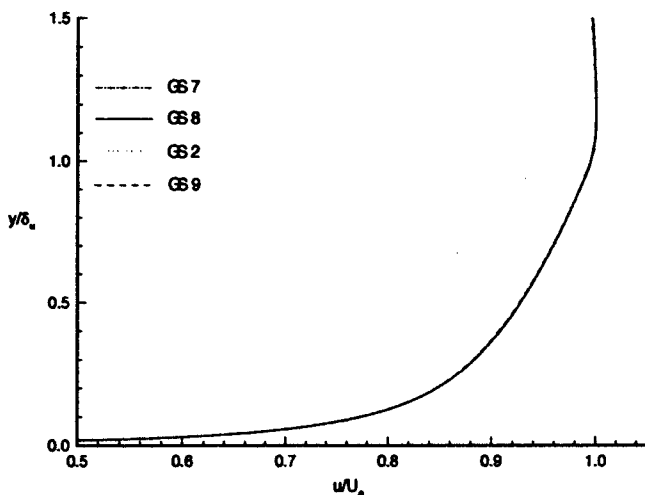


Figure G.16 Nondimensional Velocity Profile, Favorable Pressure Gradient Section, FS 71.5, Wall Spacing Variation

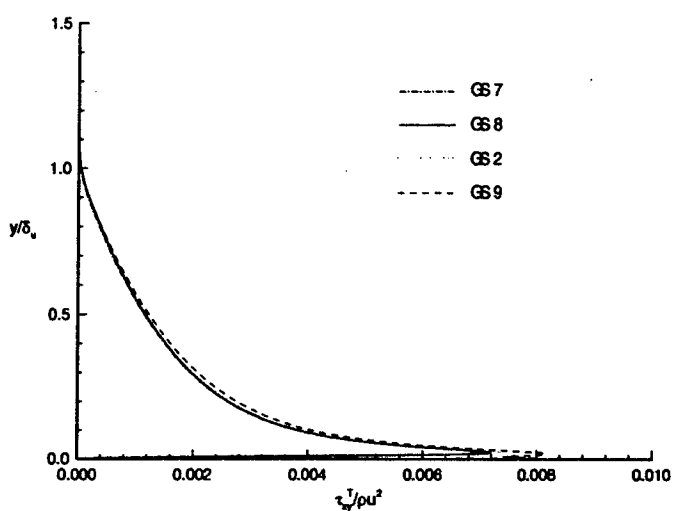


Figure G.17 Nondimensional Turbulent Shear Stress Profile, Upstream Flat Plate Test Section, FS 44.0, Wall Spacing Variation

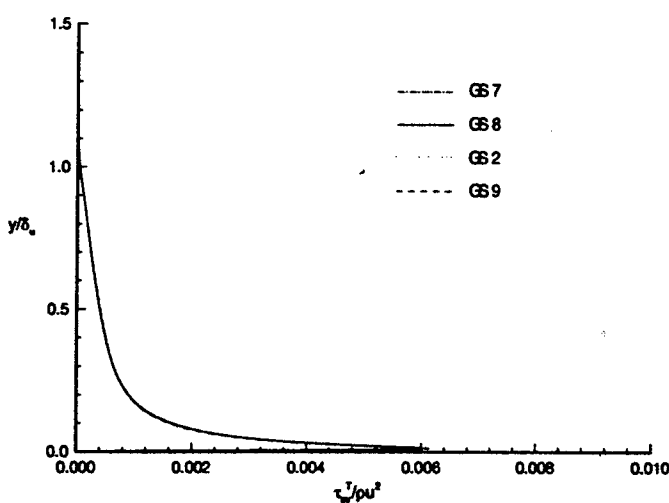


Figure G.18 Nondimensional Turbulent Shear Stress Profile, Favorable Pressure Gradient Section, FS 71.5, Wall Spacing Variation

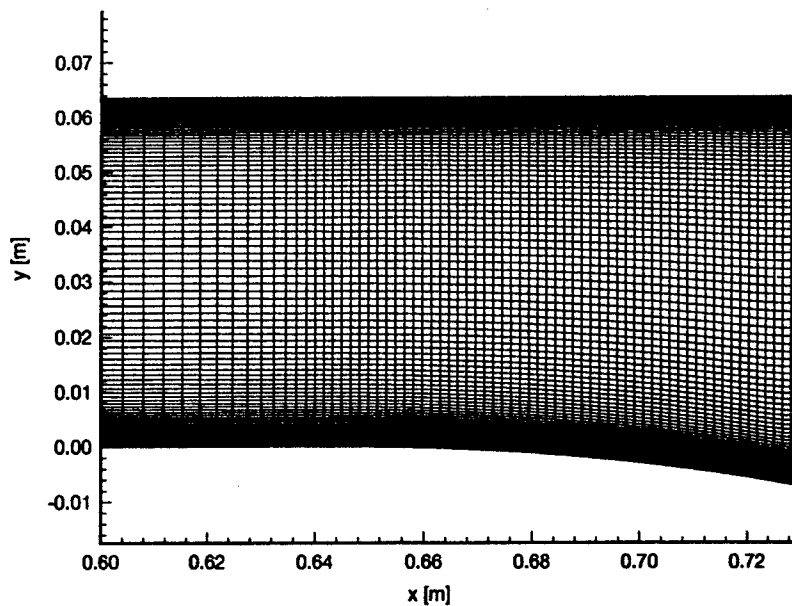


Figure G.19 Test Section Grid - FPG1

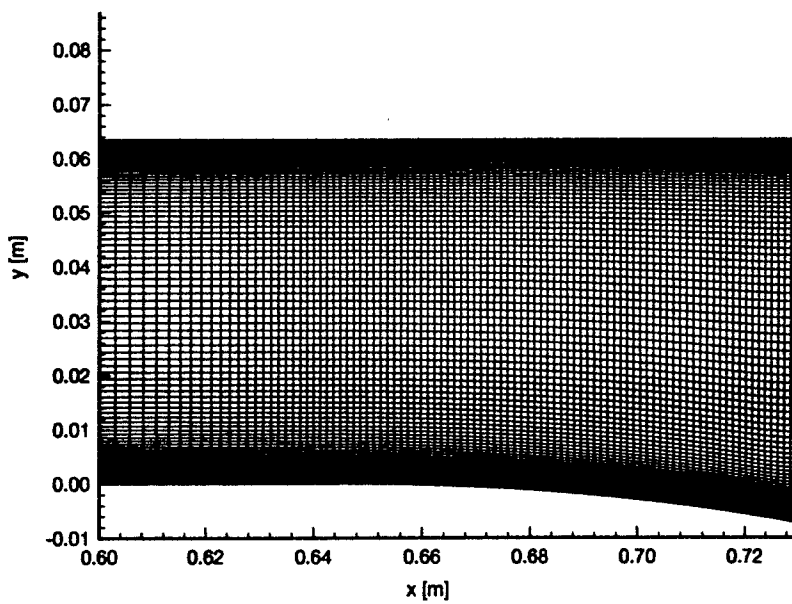


Figure G.20 Test Section Grid - FPG2

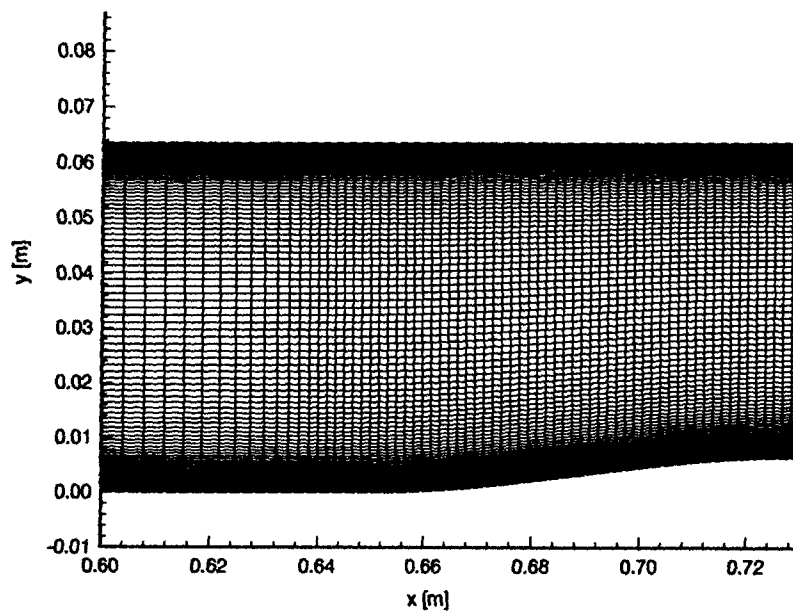


Figure G.21 Test Section Grid - APG1

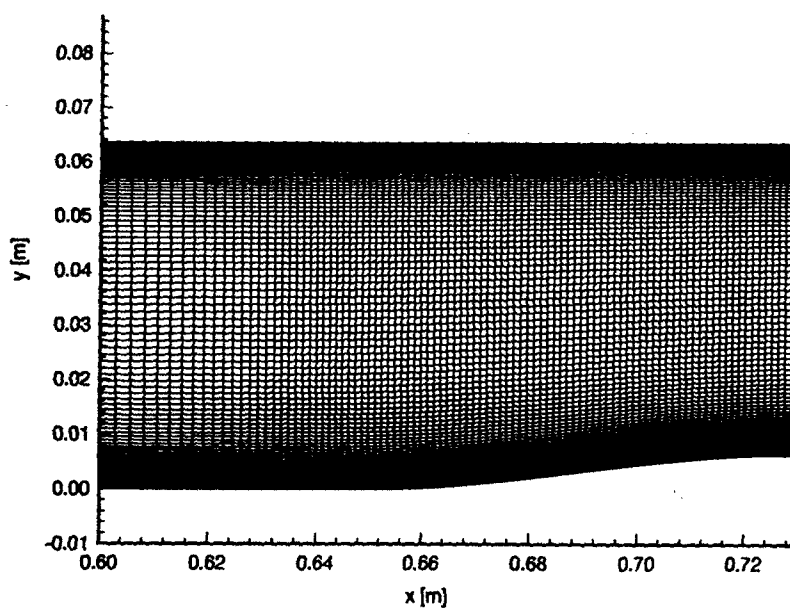


Figure G.22 Test Section Grid - APG2

Bibliography

1. Bowersox, R. D. W. "AERO 827: Turbulence." Class Notes, Winter Quarter 1995.
2. Buter, T. "AERO 751: Introduction to Computational Aerodynamics." Class Notes, Fall Quarter 1994.
3. Buter, T. "AERO 753: Advanced Computational Aerodynamics." Class Notes, Spring Quarter 1995.
4. Coakley, T. J. and P. G. Huang. "Turbulence Modeling For High-Speed Flows." *AIAA - 92 - 0436*. January 1992.
5. Dotter, Jon W. *Compressible Turbulence Measurements in a Supersonic Flow with Adverse Pressure Gradient*. MS thesis, Air Force Institute of Technology, 1994.
6. Gaitonde, D. and J. Shang. "A Numerical Study of Viscous Shock-on-Shock Hypersonic Flows with a Modified Steger-Warming Flux Split Scheme." *AIAA Paper 90-1491*. 1990.
7. Gaitonde, Datta, "Private Communications," March - October 1995.
8. Gaitonde, D.V. and J. S. Shang. "The Performance of Flux-Split Algorithms in High-Speed Viscous Flows." *AIAA-92-0186*. 1992.
9. Hale, Chad S. *Experimental Investigation of a Compressible Turbulent Boundary Layer With Adverse Pressure Gradient*. MS thesis, Air Force Institute of Technology, 1995.
10. Hoffman, Klaus A. and Steve T. Chiang. *Computational Fluid Dynamics for Engineers, One*. Engineering Education System, 1993.
11. Hopkins, E. J. and M. Inouye. "An Evaluation of Theories for Predicting Turbulent Skin Friction and Heat Transfer on Flat Plates at Supersonic and Hypersonic Mach Numbers," *AIAA Journal*, 9(6):993-1003 (1971).
12. Huffman, Richard E., Jr. *Mach 2.9 Investigation into the Flow Structure in the Vicinity of a Wrap-Around Fin*. MS thesis, Air Force Institute of Technology, 1995.
13. Kreyszig, Erwin. *Advanced Engineering Mathematics* (Seventh Edition). John Wiley and Sons, Inc., 1993.
14. Liu, F. and X. Zheng. "A Strongly-Coupled Time-Marching Method for Solving the Navier- Stokes and $k - \omega$ Turbulence Model Equations with Multigrid." *AIAA-94-2389*. 1994.
15. Luker, Joel J. *Experimental Investigation of a Compressible Turbulent Boundary Layer Including Favorable Pressure Gradient Effects*. MS thesis, Air Force Institute of Technology, 1995.
16. Miller, Raymond F. *Compressible Turbulence Measurements in a Supersonic Boundary Layer Including Favorable Pressure Gradient Effects*. MS thesis, Air Force Institute of Technology, 1994.
17. Morkovin, M. "Effects of Compressibility on Turbulent Flow." *The Mechanics of Turbulence* edited by A. Favré, New York: Gordon and Beach, 1964.

18. Morrison, J. "Flux Difference Split Scheme for Turbulent Transport Equations." *AIAA-90-5251*. October 1990.
19. Rizzetta, Donald P. and Miguel R. Visbal. "Comparative Numerical Study of Two Turbulence Models for Airfoil Static and Dynamic Stall," *AIAA Journal*, 31(4):784-786 (1993).
20. Settles, Gary S. and Lori J. Dodson. "Supersonic and Hypersonic Shock/Boundary-Layer Interaction Database," *AIAA Journal*, 32(7):1377-1383 (1994).
21. Spina, E. F., et al. "The Physics of Supersonic Turbulent Boundary Layers," *Annual Review of Fluid Mechanics*, 26:287-319 (1994).
22. Tilmann, C. "Numerical and Experimental Investigation of the Turbulent Shock/Boundary-Layer Interaction on a Wrap Around Fin Configuration." PhD prospectus, Air Force Institute of Technology, Wright-Patterson Air Force Base, Ohio, December 1994.
23. Tucker, Kelly C. *Experimental Investigation of non-Adiabatic Supersonic Slot Injection into a Supersonic Cross-Flow*. MS thesis, Air Force Institute of Technology, 1995.
24. van Driest, E. R. "Turbulent Boundary in Compressible Fluids," *Journal of the Aeronautical Sciences*, 18(3):145-160 (1951).
25. White, Frank M. *Viscous Fluid Flow* (Second Edition). McGraw-Hill, Inc., 1991.
26. Wilcox, D. C. "Progress in Hypersonic Turbulence Modeling." *AIAA-91-1785*. 1991.
27. Wilcox, David C. *Turbulence Modeling for CFD*. DCW Industries, Inc., 1993.
28. Yee, H. C. "Upwind and Symmetric Shock-Capturing Schemes." *NASA Technical Memorandum 89464*. May 1987.

Vita

Captain Eric Thomas Fick

The son of an Air Force officer, Capt Fick spent much of his childhood on the move, living in six different US states and Taiwan before settling in southern Illinois, where he attended Mater Dei High School. His scholastic achievements there enabled him to win a four year AFROTC scholarship, which he used to earn his Bachelor's degree in Aerospace Engineering at the University of Notre Dame. A distinguished graduate of the Notre Dame AFROTC program, Capt Fick was selected to receive a regular commission upon entering active duty, which he did at Hill AFB, UT in the fall of 1990. After spending eighteen months there as a Logistics Plans and Programs Officer, Capt Fick transferred to the F-16 System Support Division, where he served as the F-16 Fuel System and Environmental Control System (ECS) engineer. Eighteen months later he was selected to attend the Air Force Institute of Technology to pursue his master's degree in Aeronautical Engineering. After graduation, Capt Fick will be assigned to Wright Laboratories, where he will work in the Applied Computational Fluid Dynamics Branch.

VITA-1

Public reporting burden for this collection of information is estimated to average 1 hour per response, including the time for reviewing instructions, searching existing data sources, gathering and maintaining the data needed, and completing and reviewing the collection of information. Send comments regarding this burden estimate or any other aspect of this collection of information, including suggestions for reducing this burden, to Washington Headquarters Services, Directorate for Information Operations and Reports, 1215 Jefferson Davis Highway, Suite 1204, Arlington, VA 22202-4302, and to the Office of Management and Budget, Paperwork Reduction Project (0704-0188), Washington, DC 20503.

1. AGENCY USE ONLY (Leave blank)		2. REPORT DATE December 1995	3. REPORT TYPE AND DATES COVERED Master's Thesis
4. TITLE AND SUBTITLE NUMERICAL SIMULATION OF SUPERSONIC TURBULENT BOUNDARY LAYER FLOW UNDER THE INFLUENCE OF MILD PRESSURE GRADIENTS		5. FUNDING NUMBERS	
6. AUTHOR(S) Eric T. Fick			
7. PERFORMING ORGANIZATION NAME(S) AND ADDRESS(ES) Air Force Institute of Technology, WPAFB OH 45433-6583		8. PERFORMING ORGANIZATION REPORT NUMBER AFIT/GAE/ENY/95D-10	
9. SPONSORING / MONITORING AGENCY NAME(S) AND ADDRESS(ES) Dr. James McMichael AFOSR/NA, Bolling AFB, Washington DC		10. SPONSORING / MONITORING AGENCY REPORT NUMBER	
11. SUPPLEMENTARY NOTES			
12a. DISTRIBUTION / AVAILABILITY STATEMENT Distribution Unlimited		12b. DISTRIBUTION CODE	
13. ABSTRACT (Maximum 200 words) Mach 2.9 boundary layer flow ($R_e/m \approx 1.75 \times 10^7$) under the influence of mild pressure gradients is studied numerically. Baldwin-Lomax and $k - \omega$ turbulence models are incorporated into a cell-centered finite volume flow solver and the results are compared with hot wire anemometry and Laser Doppler Velocimetry (LDV) measurements obtained for the same geometries in the AFIT Mach 2.9 wind tunnel. Agreement between the present simulations obtained with the $k - \omega$ turbulence model and experimental velocity profiles is excellent in all test sections. Nondimensional turbulent shear stress predictions closely match experimental data in the flat plate and adverse pressure gradient sections while slightly over-predicting this quantity in the favorable pressure gradient region. Favorable pressure gradients are found to stabilize the flowfield, resulting in increased boundary layer thickness and reduced turbulent and wall shear stress distributions. Additionally, the presence of a favorable pressure gradient is found to diminish the effects of variations in upstream boundary condition specification. Adverse pressure gradients are found to de-stabilize the flowfield, resulting in increases in the turbulent shear stress, turbulent kinetic energy, and wall shear stress. Upstream effects are found to play a major role in adverse pressure gradient flowfield development. Flowfield features are predicted more accurately with the $k - \omega$ model than with the Baldwin-Lomax model.			
14. SUBJECT TERMS Boundary Layer, Supersonic, Compressible, Turbulence, Numerical Simulation, Pressure Gradient, Modeling		15. NUMBER OF PAGES 138	
		16. PRICE CODE	
17. SECURITY CLASSIFICATION OF REPORT UNCLASSIFIED	18. SECURITY CLASSIFICATION OF THIS PAGE UNCLASSIFIED	19. SECURITY CLASSIFICATION OF ABSTRACT UNCLASSIFIED	20. LIMITATION OF ABSTRACT UL